

A Search for an Additional Planet in the Hot-Jupiter
System WASP-5 by Transit Timing Variations

Akihiko Fukui

Division of Particle and Astrophysical Science,
Graduate School of Science,
Nagoya University

July 19, 2011

Abstract

Searching for transit timing variations (TTVs) of a transiting extrasolar planet can be a tool to find additional, even less massive planets existing in the same system. In addition, such additional-planet searches around hot Jupiters can be a test for migration mechanisms of hot Jupiters.

We observed 7 new transits of the hot Jupiter WASP-5b by using a 61 cm telescope located in New Zealand, aiming for detecting TTVs induced by an additional planet. When combined with other available photometric and radial velocity (RV) data, we find that its transit timings do not match a linear ephemeris; the best fit χ^2 values is 32.2 with 9 degrees of freedom, which corresponds to a confidence level of 99.982 % or 3.7 σ . Considering possible imperfect corrections of light-curve baselines, the χ^2 value reduces to 24.7, which corresponds to a confidence level of 99.668 % or 2.9 σ .

From the absence of significant TTV signals, we calculate upper limits of the mass of an hypothetical additional planet by means of numerical simulations, as a function of orbital-period ratio of the two planets. We place the limits of 2 M_{\oplus} (3 σ conf.) near 1:2 and 2:1 mean motion resonances (MMRs) with WASP-5b, assuming that the two planets are co-planer. These limits narrow the limits placed from the RV data only, where the limits of 22-70 M_{\oplus} over the orbital-period ratio from 0.2 to 5.0 are placed. We also put an upper limit of 43 M_{\oplus} (3 σ conf.) on excess of Trojan mass using both RV and photometric data.

Using the published transit timing data of 15 hot Jupiters, we estimate the frequency of second planet occurrence near 2:1 MMR with a hot Jupiter of $0.14_{-0.1}^{+0.2}$ for the second-planet mass of 10 M_{\oplus} , and <0.15 for that of $>30 M_{\oplus}$ (90% conf.). This result indicates that

secondary planets rarely exist near 2:1 MMR with hot Jupiters, which excludes a certain type of hot-Jupiter migration scenarios.

Acknowledgments

First of all, I would like to express my great gratitude to my supervisor Prof. Yoshitaka Itow for giving me the opportunity of studying this work, and providing strong support for this ph.D. thesis. I believe this thesis would never exist without his support.

I would express my sincere thanks to Prof. S. Inutsuka, Prof. F. Abe, Prof. S. Watanabe, and Prof. T. Sumi for reviewing my thesis carefully and providing many valuable advices. I would also like to extend my gratitude to Prof. Y. Muraki, Prof. K. Masuda, Prof. Y. Matsubara, and Prof. T. Sako for supporting me in many ways.

I would like to thank all the members of the MOA collaboration for supporting this work. I wish to give special thanks to P. J. Tristram for obtaining transit data and keeping me from feeling lonely during my stay at Mt. John. I would like to express my great appreciation to A. C. Gilmore and P. M. Kilmartin for everything they have done for me during my stay at Mt. John. I would also like to thank Prof. D. Sullivan for taking time to correct my English. I am really thankful to all the master and doctoral students (past and present) of MOA, especially K. Kamiya, K. Furusawa, and N. Miyake, for sharing fulfilling days through observations and discussions as well as pleasures.

I would like to express my great gratitude to Dr. N. Narita, who did not only originally provide me the idea of this thesis's theme but also teach me a lot of things about transiting planets and support my work in many aspects. I would also like to thank Prof. M. Tamura for giving me valuable advices. I wish to thank the members of the Division of Optical and Infrared Astronomy of NAOJ who made my stay there very pleasant and comfortable.

I would like to thank Prof. D. Latham and Prof. M. J. Holman for providing me a valuable opportunity to stay Harvard-Smithsonian CfA and discussing with me about my work. I would also thank Prof. J. N. Winn for giving me important advices. I am also grateful to all the members of CfA who welcomed me while I was there.

I am grateful to all the members of the CR lab. for giving me comfortable environments

and a lot of fun. Especially I wish to thank to my friends of T. Tanaka and T. Mase, who have shared a lot of time with me inside/outside the lab. I wish to express my gratitude to Ms. T. Kainai, who has taken care of an enormous amount of office works.

Finally, I would like to extend my great thanks to my family for supporting me behind the scenes. Last but not least, I thank the love and support of my future wife, Maki.

Contents

1	Introduction	6
1.1	Extrasolar Planets	6
1.2	Overview of the Classical Detection Methods	9
1.2.1	Pulsar Timing	9
1.2.2	Radial Velocity and Astrometry	10
1.2.3	Transit	12
1.2.4	Microlensing	14
1.2.5	Direct Imaging	15
1.2.6	Planetary Distribution	16
1.3	Planetary Formation Mechanisms	18
1.4	Hot Jupiters and their Migration Mechanisms	20
1.4.1	Disk-planet Interaction Model	20
1.4.2	Planet-planet Interaction Model	22
1.4.3	The Rossiter-McLaughline (RM) Effect	23
1.4.4	Multiplicity of Planets in Hot-Jupiter Systems	25
1.4.5	Planetary Pairs in Mean Motion Resonances	28
2	Transit Timing Variations	33
2.1	Brief History	33
2.2	Planetary TTV signals	38

2.2.1	Interior Perturbing Planets with Much Smaller Periods	38
2.2.2	Exterior Perturbing Planets on Eccentric, Larger Orbits	39
2.2.3	Both Planets on Initially Circular, non-MMR Orbits	40
2.2.4	Planets on Initially Circular Orbits Locked in MMRs	40
2.2.5	Close Planets with Non-zero Eccentricities	42
2.2.6	Planetary Detection Sensitivity	43
2.3	Other Effects Causing TTVs	45
2.4	Test for Hot-Jupiter Formation Mechanisms	45
3	The MOA Project and Instruments	48
3.1	The MOA Project	48
3.2	Telescope and Camera	49
3.3	Study of Noise Property	52
3.3.1	Readout Noise	52
3.3.2	Dark Noise	55
3.3.3	Flat-field Noise	57
3.3.4	The Semi-Realtime Auto Guiding Software	60
4	Observations and Data Reduction	63
4.1	Target Selection	63
4.2	The WASP-5 System	64
4.3	Observations	66
4.4	Data Reduction	67
5	Light Curve Analysis	73
5.1	Baseline Systematic Correction	73
5.2	Estimation of Time-Correlated Systematic Noise	78
5.3	Light Curve Fitting	80

6	Combined Analysis with Published Data	83
6.1	Data Sets	83
6.2	Model Fitting	84
6.3	Measurement of TTVs	89
7	Upper Limits on the Mass of the Secondary Companion	93
7.1	Numerical Simulation	94
7.2	Constraining on Excess of Trojan Mass	97
8	Discussion	100
8.1	Example Models of Secondary Planet	100
8.2	Correlation with the Correction of Light-Curve Baseline	106
8.3	Statistical Analysis of TTVs in Hot Jupiters	109
8.4	Future Prospects	118
9	Conclusion	120
A	Baseline Correction Funcion	122
B	Analytic Transit Light Curve	124
B.1	The Mandel's Model	124
B.2	The Ohta's Model	126
C	Analytic Formula for Rossiter-McLaughlin Effect	131
C.1	General Description	131
C.2	The Hirano's Model	132

Chapter 1

Introduction

1.1 Extrasolar Planets

Are we alone in the universe? This question has been a fundamental one for human beings for long times. Under the ideology of the geocentric universe proposed by Aristotle in the third century B.C., humans had thought that the Earth and human itself were special so that there was no need to wonder another planetary system. The heliocentric view, introduced by Copernicus in 1543, pointed that the Earth is just one of many planets orbiting the Sun, and this concept had observationally been verified by Galileo in the 17th century. In the 20th century, it had been revealed that the Sun is also just one of a huge number of stars within the milky way galaxy, and furthermore, the galaxy is also one of a vast amount of galaxies existing in the universe. Through these paradigm-shifts, the quest for another planetary system beyond our solar system had naturally been opened.

In 1855, Jacob claimed that the orbit on the sky of a binary system 70 Ophiuchi showed an anomaly due to a planetary body (Jacob 1855). Although his claim was rejected by later observations, it was probably the first claim for an exoplanet discovery. In the mid-20th century, thanks to rapidly-developed telescopes and photographic technology, serious exoplanet-huntings had been started. In 1943, Reuly and Holmberg claimed again an

existence of a planet around 70 Ophiuchi (Reuyl & Holmberg 1943), and Strand also claimed an another one around 61 Cygni (Strand 1943), both by using the astrometric technique. However, these discoveries have not been confirmed by any followup observations. In 1963, van de Kamp reported a detection of a planet around Barnard's star via the same technique (van de Kamp 1963), although, this claim had been suspected for many years and was completely ruled out in 1973 (Gatewood & Eichhorn 1973).

In the 1980s, astronomers had achieved significant development in measuring radial velocity (RV) of stars, which improved the RV precision from $\sim 0.5 \text{ km s}^{-1}$ to $\simeq 15 \text{ m s}^{-1}$. This improvement enabled researchers to start RV surveys to search for planetary companions around stars. However, unfortunately, most of these surveys had failed to find any planet. Walker et al. concluded that there was no Jovian planet nor brown dwarf companion in a sample of 21 stars after 12-years survey using the Canada-France-Hawaii Telescope with a high precision echelle spectrograph (Walker et al. 1995).

In 1992, surprisingly, the first discovery of extrasolar planets was reported around a neutron star via the pulsar timing method (Wolszczan & Frail 1992). This news was followed by a discovery of the first extrasolar planet orbiting a solar-like star via the RV technique in 1995 (51 Peg b, Mayor & Queloz 1995). Unexpectedly, this sub-Jupiter mass planet has the orbital period of only 4.2 days. Such a close-in giant planet, so-called 'hot Jupiter', had never been imagined from the planets in our solar system, which had been the only planetary system involving a main sequence star known before the discovery. Since then, more than 500 extrasolar planets have been detected via several detection techniques including transit, microlensing, and direct imaging in addition to the foregoing two.

From these discoveries, high diversity of planetary systems in the galaxy has been revealed; such as high-eccentricity planets so called 'eccentric planets' and the hot Jupiters as well, both of which are not seen in our solar system. The diversity suggests that the mechanisms of planetary formation and evolution are more complex than previously thought.

Especially, hot Jupiters, which are defined roughly as Jupiter-mass planets within ~ 0.1 AU, are considered never to form *in situ* due to the lack of their materials, and have significantly migrated from the outer parts of these systems to the current positions. The migration mechanisms of hot Jupiters are, although several scenarios have been proposed, still under discussion, and that is one of the motivations of this paper.

In recent years, thanks to the developments of observational instruments and techniques, much lower-mass planets have gradually been found. The High Accuracy Radial velocity Planet Searcher (HARPS) spectrograph on the 3.6 m telescope at La Silla and the High Resolution Echelle Spectrometer (HIRES) spectrograph on the 10 m Keck telescope both have achieved the RV precisions of $\sim 1 \text{ m s}^{-1}$, with which many several Earth-mass planets have been discovered (e.g. Lovis et al. 2011; Vogt et al. 2010). Space telescopes for transit survey such as *CoRoT* and *Kepler* have successfully been finding a large number of small planets or planetary candidates including Earth-like planets (e.g. Léger et al. 2009; Borucki et al. 2011). The microlensing technique also has the capability to find even sub-Earth mass planets (Yee et al. 2009). Nevertheless, the first discovery of an Earth-mass planet is still being awaited.

Measuring transit timing variations, the method employed in this paper, is a novel technique to find an additional planet existing in known transiting planetary systems. This technique also has a sensitivity to even Earth-mass planets lying on orbits of mean motion resonances with transiting planets. This method can also be a powerful tool to reveal the multiplicity of hot Jupiter systems, which could be a test for the hot-Jupiter formation mechanisms. The findings from such observations combined with other vast observational and theoretical efforts will help us to understand overall planetary-formation scenarios, and how common we are in the universe.

1.2 Overview of the Classical Detection Methods

Since an extrasolar planet itself is very faint as well as an extremely brighter host star lies just beside the planet, it is difficult to distinguish the two objects spacially. Therefore, most of the extrasolar planets discovered to date have been detected by several indirect methods, such as pulsar timing, radial velocity, transit, and microlensing. An another indirect method, astrometry, is close to reaching its first discovery. The direct imaging method has now been succeeding to find planets lying at the outermost part of planetary systems. The brief summary of each method is described bellow.

1.2.1 Pulsar Timing

The first extrasolar system outside the solar system was detected via the pulsar timing method around a millisecond pulsar, PSR 1257+12 (Figure.1.1, Wolszczan & Frail 1992). This technique relies on investigating periodic variations in arrival time of radio pulses from a pulsar due to the presence of planetary mass objects around the central object. Currently, four planets around two mllisecond pulsars have been discovered: three around PSR 1257+12 (Wolszczan 1994) and one around PSR B1620-26 (Backer et al. 1993). The remarkably-stable rotational frequencies of millisecond pulsars make them sensitive to very low mass planets, and indeed one of the four planets has only 0.02 Earth masses, which is the lowest mass among all the known planets. However, such planets are orbiting neutron stars, which are residual objects of supernovae, and are thought to have formed in different ways from those for planets around main sequence stars. Therefore, these two types of planet should be different in their circumstances, and the pulsar-timing planets are generally considered as a different category from those around main sequence stars.

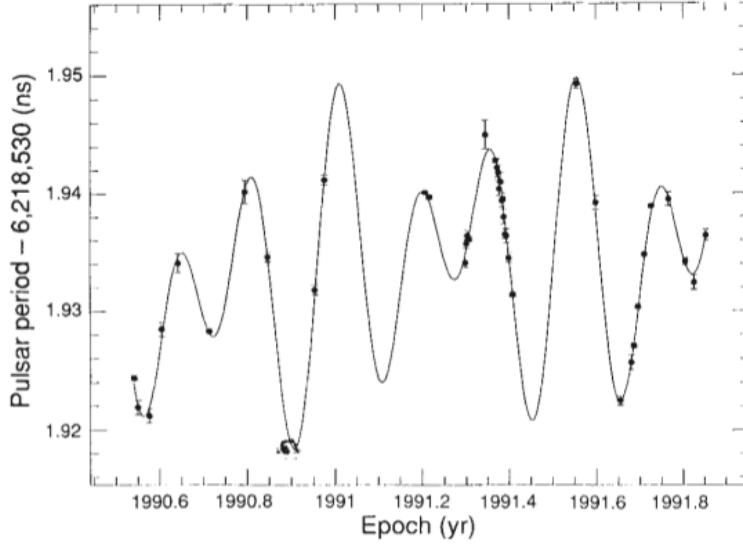


Figure 1.1: Period variations of PSR1257+12 (from Wolszczan & Frail 1992). The solid line denotes changes in period predicted by a two-planet model, in which planets with masses of $2.8 M_{\oplus}$ and $3.4 M_{\oplus}$ orbit almost circularly around the central object with periods of 98.2 and 66.6 days, respectively.

1.2.2 Radial Velocity and Astrometry

Motion of a planet orbiting a star causes the star to undergo a reflex motion about the planet-star barycenter. Observing this motion by measuring either radial velocity or angular (or astrometric) position of the star, one can know the existence of the planet indirectly.

The radial velocity (RV) method relies on the former observables obtained by measuring doppler shifts of stellar spectral lines. The velocity amplitude of a star wobbled by a planet, K , is expressed as

$$K = \left(\frac{2\pi G}{P} \right)^{1/3} \frac{M_p \sin i}{(M_p + M_*)^{2/3}} \frac{1}{(1 - e^2)^{1/2}}, \quad (1.1)$$

where G is the gravitational constant, P is the orbital period, M_p is the planetary mass, M_* is the stellar mass, i is the orbital inclination, and e is the orbital eccentricity. K , P and e can be solved from the observations of radial velocity variations. Therefore when the stellar mass is estimated from the spectral type of the star and $M_p \ll M_*$, $M_p \sin i$

can be obtained. Since the inclination i is unknown unless determined by other means (e.g., measuring transit impact parameter, or constraining it from dynamical motions of multiple planets in the system), this technique generally provides only a lower limit about the planetary mass. The equation (1.1) also indicates that this detection method favors massive, eccentric and short-period planets orbiting less massive stars.

If one measured the radial velocity of the Sun from outside the solar system as edge-on, the velocity amplitude would be only 13 m s^{-1} . Nevertheless, thanks to the developments of high-precision radial velocity techniques, 1 m s^{-1} precision has now been achieved by several groups (e.g. Lovis et al. 2011; Vogt et al. 2010). Since the first discovery of an RV planet in 1995 (51 Peg b, Figure. 1.2), about 370 planets ($\sim 2/3$ of all the known extrasolar planets) have been discovered via the RV technique.

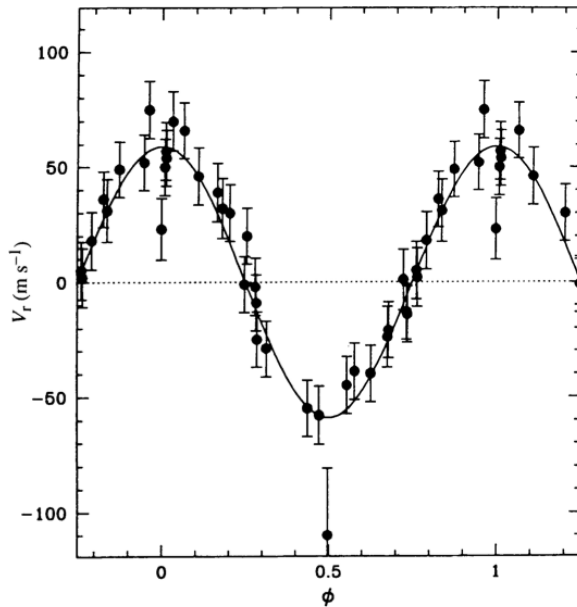


Figure 1.2: Phase folded radial velocity variations of 51 Peg (from Mayor & Queloz 1995). The solid line represents the computed planetary model of $M_p \sin i = 0.47 M_{\text{Jup}}$ and $P = 4.23$ days.

The astrometry method finds a planet by observing positional changes of a star on the sky plane due to the orbital motion of the planet. The semi-major axis of the stellar orbit

with respect to the barycenter of the system, a_* , is equal to $a_p(M_p/M_*)$, where a_p is the semi-major axis of the planetary orbit. This can be seen on the sky plane as the angular size of

$$\theta = \frac{a_*}{d} = 50\mu\text{as} \left(\frac{M_p}{M_{\text{Jup}}} \right) \left(\frac{M_*}{M_{\odot}} \right)^{-1} \left(\frac{a_p}{1\text{AU}} \right) \left(\frac{d}{20\text{pc}} \right)^{-1}, \quad (1.2)$$

where d is the distance between the star and the observer. The astrometric precision obtained from ground-based observations is currently limited to the order of ~ 0.1 mas, and no planet has been discovered via this technique so far. The ground-based interferometers such as VLTI, or future space missions aiming for astrometric observations like GAIA and JASMINE will be expected to discover a number of exoplanets residing outside regions of planetary systems.

1.2.3 Transit

If the orbital plane of an exoplanet almost aligns to the line of sight, the planet periodically passes (transits) in front of the host star and one can see a periodic dimming of the stellar brightness. The dimming ratio corresponds to the ratio of the projected area of the planet to that of the star. In the case of Jupiter and the Sun, the area ratio is about 1%, which drops to 0.0086 % in the case of the Earth instead of Jupiter.

From the transit light curve, one can basically obtain the planet-to-star radius ratio, the transit duration, and the inclination of the planetary orbit. Therefore by combining with radial velocity observations and an estimation of the stellar mass, the true planetary mass as well as the planetary density can be extracted. There is no other way to measure the density of an exoplanet, which is valuable information to speculate the internal composition of the planet. Moreover, a transiting planet provides us many valuable opportunities to observe its atmospheric compositions, the planetary surface temperature, the obliquity of orbital axis against the stellar spin axis, the dynamical interaction with other planets in the same system, and so forth (e.g. Winn 2010).

Since the first discovery of transiting planets, HD 209458b (Figure 1.3, Charbonneau et al. 2000), more than 140 transiting planets have been discovered so far. Because the geometric probability to occur transit for a planet, P_{transit} , is inversely proportional to the distance between the planet and the star:

$$P_{\text{transit}} = \frac{R_*}{a}, \quad (1.3)$$

where R_* is the stellar radius, the discovered transiting planets are strongly biased to those orbiting close to their host stars. In addition, the larger the planet is, the easier it can be detected; this means that “hot Jupiters” are preferably found by this method (See Figure 1.6). Hot Jupiters themselves are interesting for their formation and migration processes, and thanks to the many advantages arising from transiting, the transiting hot Jupiters can be good laboratories to test for these mechanisms.

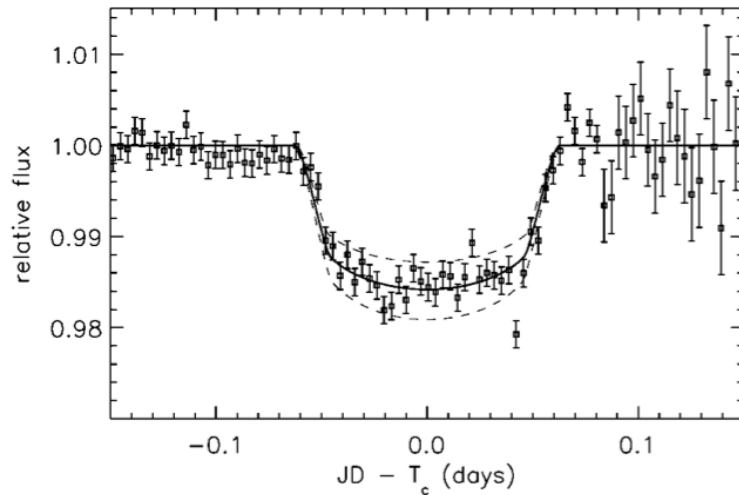


Figure 1.3: Phase folded photometric data of HD209458b (from Charbonneau et al. 2000). Two distinct transit data are combined and binned into 5 m averages. The solid line represents the best-fit transit shape which corresponds to $R_p=1.27 R_{\text{Jup}}$, $i=87^\circ.1$. The lower and upper dashed lines are transit curves that would occur for a planet 10% larger and smaller in radius, respectively.

In March 2009, NASA’s *Kepler* space craft was launched aimed at detecting Earth-like

planets in habitable zones by means of the transit. It has been monitoring about 150,000 stars with magnitudes down to $V=16$. In February 2011, the *Kepler* team announced the detections of about 1,200 candidates of transiting planets with sizes down to \sim Earth radius from its four months' observation (Borucki et al. 2011). From its nominal 3.5-year mission, *Kepler* will finally have found a much larger number of transiting planets including many habitable planets.

1.2.4 Microlensing

The microlensing technique relies on the theory of gravitational relativity. If the light from a source star passes by a massive (lens) object lying between the source star and the observer, the light is bent by the gravity of the lens object, and two separated stellar images are produced. This effect is observed just as a stellar brightening phenomenon, referred to as a “microlensing” effect, when the lens' mass is as less massive as a star and the produced two images do not separate beyond the resolution (Paczynski 1986). If the lens is a single star, this effect can be observed as a symmetric light curve due to the relative motion of the source and the lens stars. On the other hand, if the lens star hosts a planet, the light curve could deviate from the symmetric shape, from which one could recognize the existence of the planet (Mao & Paczynski 1991; Gould & Loeb 1992). Because this technique does not rely on any emissions from the host star nor the planet, it is possible to find planets around low-mass stars or even brown dwarfs. This technique also has an unique sensitivity to low-mass planets lying moderate separations (a few AU) from their host stars, most of which are M-type main sequence stars because of their domination in the galaxy.

Using this technique, the first planet, OGLE-2003-BLG-235/MOA-2003-BLG-53Lb, was discovered in 2003 (Figure 1.4, Bond et al. 2004). Since then, totally 13 planets in 12 systems have been detected. About half of these planets have the masses of Jupiter class, and the others have the masses of Neptune or super-Earth classes; considering the

higher detection efficiency for more massive planets, this fact indicates that the Neptune or super-Earth class planets are more common than the Jupiter-class planets in the region of a few AU around M-type stars (Sumi et al. 2010).

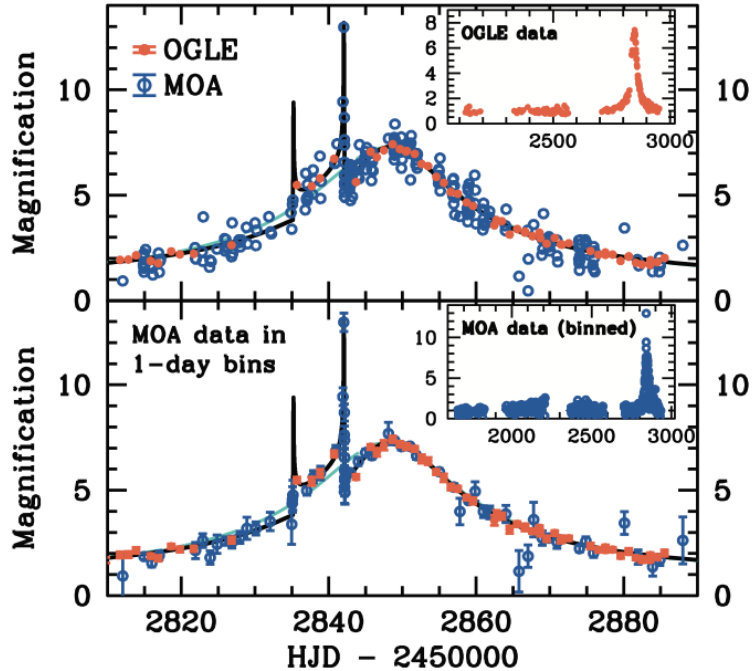


Figure 1.4: Light curve with best fitting (black lines) and single-lens (light blue lines) models of OGLE-2003-BLG-235/MOA-2003-BLG-53Lb (from Bond et al. 2004). The OGLE and MOA measurements are shown as red filled circles and open blue circles, respectively. The top panel presents the complete data set during 2003 (main panel) and the 2001–2003 OGLE data (inset). For clarity, the error bars were not plotted, but the median errors in the OGLE and MOA points are indicated in the legend. The bottom panel is the same as the top panel, but with the MOA data grouped in 1 day bins, except for the caustic crossing nights, and with the inset showing MOA photometry during 2000–2003.

1.2.5 Direct Imaging

The direct imaging technique, as its name suggests, detects angularly-separated planets themselves. This method is considered to be the most effective one to probe the planetary atmospheres. However, it is very challenging because planets are much fainter than host stars and angularly close to the host stars. If the Sun and Jupiter were at 10 pc from

an observer, the contrast of the two would be about 10^9 with the angular separation of only $0''.5$. The contrast reduces by two orders of magnitude when the system is as young as ~ 100 Myr and is observed in infrared wavelength. Nevertheless, for such a small angular separation, the diffraction from a bright host star usually overwhelms the faint planetary signals. In order to overcome this effect, stellar coronagraphs have been developed by placing an opaque mask at the focus of the telescope on top of the central core of the diffraction pattern of a star, and a well-adjusted diaphragm in the relayed pupil plane to block the diffraction residuals (Ferrari et al. 2007). After a decade of effort, several successful detections of giant planets have been reported; an $\sim 8 M_{\text{Jup}}$ planetary mass object with a projected separation of ~ 330 AU from the young solar analog 1RXS J160929.1-210524 (Lafrenière et al. 2008), a $\sim 1 M_{\text{Jup}}$ planet at 119 AU from the A-type star Fomalhaut (Figure 1.5, Kalas et al. 2008), three $\sim 7\text{--}10 M_{\text{Jup}}$ planets with separations of 24–68 AU from the A-type star HR 8799 (Marois et al. 2008), and an $\sim 8 M_{\text{Jup}}$ planet candidate at $\simeq 8$ AU from the A-type star β Pictoris (Lagrange et al. 2009). Such outermost massive planets are challenging to form via the standard planetary formation model known as “core accretion”, and require alternate planetary formation models such as “gravitational instability”.

Future space missions such as NASA’s Terrestrial Planet Finder (TPF), ESA’s Darwin (although they were cancelled), or similar ones will explore a signature of life on Earth-like planets by ultraprecise direct imaging methods.

1.2.6 Planetary Distribution

As of June 2011, more than 550 extrasolar planets¹ have been detected via the several detection techniques. Figure 1.6 shows the distribution of the planets discovered as of 2010 in the plane of semi-major axis normalized by the snow line and planetary mass. The snow

¹<http://exoplanet.eu/>

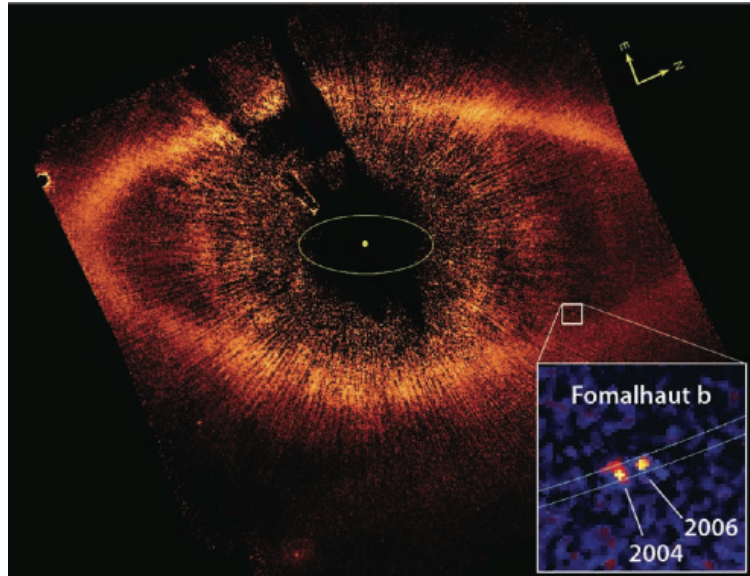


Figure 1.5: HST coronagraphic image of Fomalhaut at 0.6 mm, showing the location of Fomalhaut b (white square) 12.7 arc sec radius from the star and just within the inner boundary of the dust belt (from Kalas et al. 2008). The yellow circle marks the location of the star behind the occulting spot. The yellow ellipse has a semi-major axis of 30 AU at Fomalhaut (3.9 arc sec) that corresponds to the orbit of Neptune in our solar system. The inset is a composite image showing the location of Fomalhaut b in 2004 and 2006 relative to Fomalhaut.

line is a boundary which separates liquid and ice for H_2O . The black, blue, red, magenta, and green points represent the planets discovered via the RV, transit, microlensing, direct imaging, and pulsar timing methods, respectively. Note that the masses of the most RV planets are shown as their lower limits. Each of the methods have its unique sensitivity region, and therefore they are complimentary with each other.

The alphabets in this figure stand for the initials of the planets in our solar system. One can see that the distribution of exoplanets is widely different from that of the planets in our solar system, although this difference may be affected by some detection biases. This fact suggests that planetary systems in the universe are more various than one thought. Especially, one can see the pile-up of close-in massive planets known as hot Jupiters, which are thought to have formed in much outer regions and migrated to the current positions,

in any ways. The migration mechanisms of hot Jupiters are still under debate.

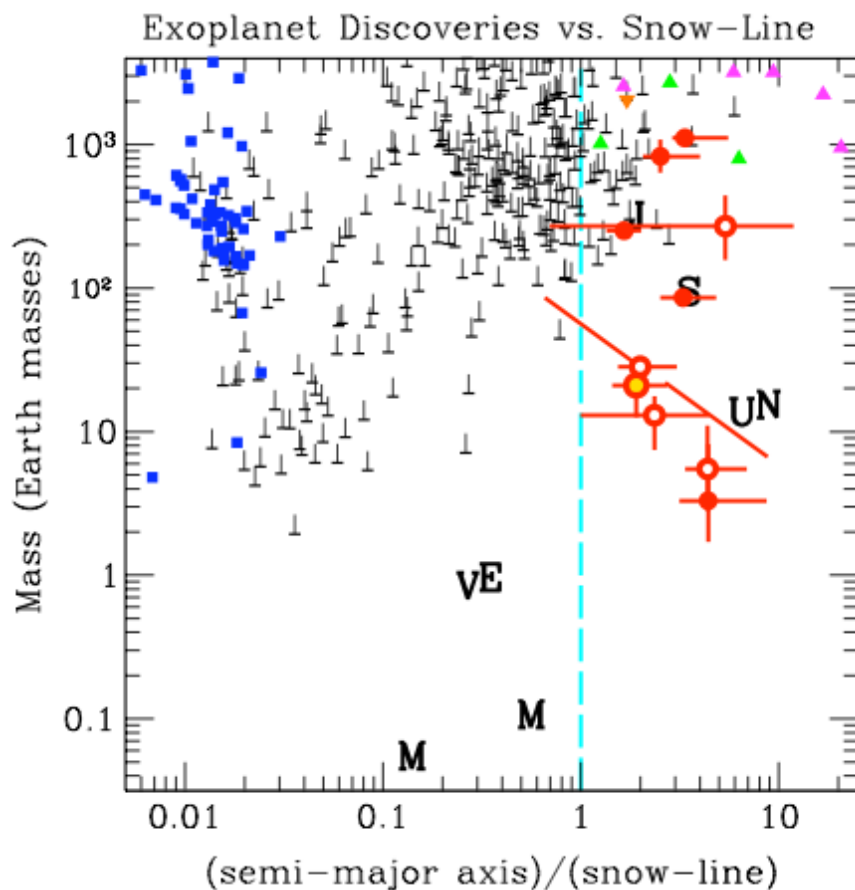


Figure 1.6: Known exoplanets as a function of mass vs. semi-major axis divided by the snow-line, which is taken to be at $2.7 \text{ AU } M_*/M_\odot$. Black, blue, red, magenta, and green points represent the planets discovered via RV, transit, microlensing, direct imaging, and pulsar timing methods, respectively. For the masses of RV planets, their lower limits are indicated. Alphabets indicate the initials of planets in our solar system. From Sumi et al. (2010).

1.3 Planetary Formation Mechanisms

Planets are considered to form from protoplanetary disks, which are generated concurrently with protostars. The disks consist of a mixture of H_2/He gas and small amount of heavy elements. The existence of protoplanetary disks have been confirmed around many young stars, however, there are several models to form planets from these disks, such as

“gravitational instability” and “core accretion” models.

According to the gravitational instability model, gas giant planets can form rapidly (in $\sim 10^3$ years) by disk instability (Cameron 1978; Boss 1997). The gas in a marginally gravitationally-unstable disk forms clumps, which subsequently shrink to planetary densities and become protoplanets. In this model, solid cores might form *a posteriori* through coagulation and sedimentation of dust grains within the protoplanets, and icy or rocky planets might form by losing gaseous envelopes of these protoplanets. However, this model requires a massive and cold enough disk to be gravitationally unstable, and it is difficult to form gas giant planets inside ~ 20 AU from the moderate-size disks ($< 0.043M_{\odot}$) (Boss 2010). Therefore, most scientists think that many of the known extrasolar planets have not formed via the gravitational instability model but via the core accretion model, being described later. Nevertheless, some planets lying outside regions, such as those around HR 8799 (Marois et al. 2008), have difficulties to be explained by the core accretion model, and these might have formed via the gravitational instability model.

The basic idea of the core accretion model, which is also referred to as a standard model, had been developed in 1980s (e.g. Hayashi et al. 1985). This model is based on an assumption that planets form in a protoplanetary disk with the mass of $\sim 1\%$ of the stellar mass consisting of $\sim 99\%$ H₂/He gas as well as $\sim 1\%$ dust grains. In this disk, the dust grains accrete to the mid-plane of the disk and build up as small bodies (planetesimals), and these planetesimals collide with each other to grow up much larger bodies (protoplanets). As the rotational speed of the gas disk is higher in the inner region than the outer one, the growing rate of protoplanets is higher in the inner region. On the other hand, as the materials are richer for the outer region of the disk, especially outer than the snow line, where H₂O can be ice grains, protoplanets at far from a certain distance (a few AU) can be cores which are massive enough to accumulate the surrounding gas and to become massive gas planets. Inner protoplanets will become rocky planets which are too light to capture

the surrounding the gas, while far outer protoplanets will become icy planets without rich gasses, since the disk gas will dissipate as time passes so that the protoplanets cannot reach the critical cores by the time the gas entirely dissipates. This basic overview of planetary formation scenario can, although many detailed contradictions still remain in each stage, explain the present structure of the solar system well. On the other hand, the observed diversity of the extrasolar planets implies that they have migrated significantly after their formations.

1.4 Hot Jupiters and their Migration Mechanisms

Among the planets discovered to date, about one fifth are hot Jupiters. They are thought to have formed in the outer regions of the protoplanetary disks and subsequently migrated inward in any ways. The migration process of a giant planet should affect the stabilities of other planets in the system, and therefore how the process works is an important factor to determine the habitability of the system.

There are two major migration models for hot Jupiters: one is a migration process induced by interactions between disk gas and a planet such as the type-II migration (hereafter disk-planet interaction model, e.g. Lin & Papaloizou 1986), and the other is caused by interactions between multiple planets followed by tidal circularization (hereafter planet-planet interaction model, e.g. Nagasawa et al. 2008). However, these models have large uncertainties, and the hot-Jupiter migration processes are still controversial.

1.4.1 Disk-planet Interaction Model

In the core accretion scheme, planetesimals collide with each other to grow up protoplanets. When a protoplanet becomes massive enough, gravitational interaction between the protoplanet and the disk gas becomes to be effective. The protoplanet's gravity disturbs the surrounding disk gas, and as reaction forces, the protoplanet obtains both outward and

inward torques. The detailed calculations show that the net torque acting on the protoplanet becomes negative, which means that the body migrates inward (type-I migration, e.g. Ward 1986; Tanaka et al. 2002). Although the migration timescale of an Earth-mass body at 1 AU is calculated to be about $\sim 10^5$ years, and this gives rise to a problem to form a giant planet because the typical timescale of giant-planet formation is much longer ($\sim 10^6$ years), several ideas to delay the type-I migration timescale have been proposed (e.g. Masset et al. 2006). Ida & Lin (2008) proposed that even if the type-I migration works effectively so that most protoplanets fall onto the star, in the late stage of the gas depletion when the type-I migration doesn't work effectively on the residual cores, they can even become a massive core so as to capture the remaining gas and to be a gas giant planet.

Once a protoplanet gets a substantial mass ($\sim 10M_{\oplus}$) so that the surrounding gas starts to accrete onto the core, the growing gas-giant planet opens a gap in the disk and lock itself into it. Due to viscous diffusion of the gas disk, most part of the disk gas accretes onto the central star, and the gap-locked planet also migrates inward along with the disk accretion (type-II migration, Lin & Papaloizou 1985). The timescale of the type-II migration is somewhat longer, $\sim 10^6$ years, which is comparable to the timescale of disk dispersion.

In these ways, the type-II migration or a combination of the type-I and type-II migrations can convey a gas giant planet to the vicinity of the host star. Hence, if any migration-halt mechanisms can work on the planet, it could be a hot Jupiter. The planet's migration may stop as a result of tidal interactions with the star, or through truncation of the inner gas disk by the stellar magnetosphere (Lin et al. 1996). Figure 1.7 shows the schematics of the type-II migration and the stellar magnetosphere effect.

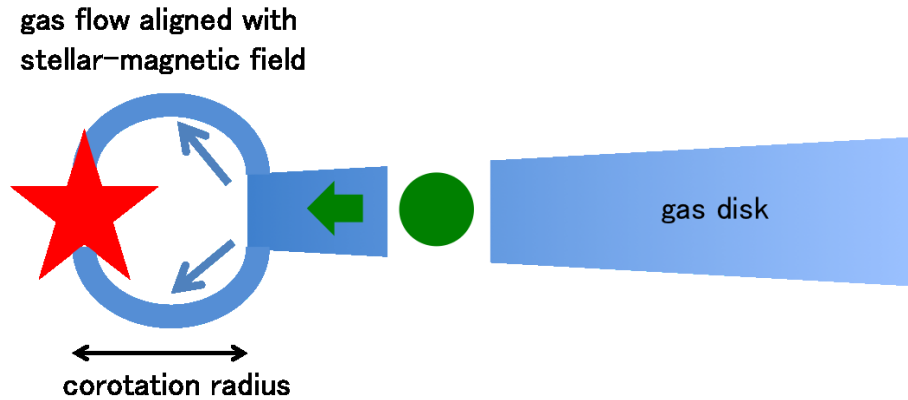


Figure 1.7: A schematic of the type-II migration and one of the migration-halt mechanisms. A gas giant planet (green circle) opens a gap in the gas disk (blue band) and migrates toward the host star (red star) along with the disk accretion. With the existence of the stellar magnetosphere, the inner ionized disk gas is dragged toward the star along the magnetic lines, resulting in a cavity opened in the circumstellar disk. The cavity’s radius is equal to the corotation radius, where the Keplerian orbital period is the same as the stellar spin period. The migrated giant planet will stop at the inner edge of the disk.

1.4.2 Planet-planet Interaction Model

According to the planet-planet interaction model, multiple (especially more than two) giant planets gravitationally interact with each other after the disk gas has dissipated, and one (or some) of the planets can be scattered so as to obtain a large eccentricity. If the eccentricity is large enough that the planet gets close enough to the host star at its pericenter ($\lesssim 0.05$ AU), the eccentricity will be damped by the tidal effect of the host star, and the planet will eventually be a hot Jupiter (see Figure 1.8). However, the probability that the pericenter distances of giant planets become small enough to damp the eccentricities is too small to account for all the observed hot Jupiters. Alternatively, the “Kozai effect” (Kozai 1962) can be responsible for a certain fraction of planets to have large eccentricities (Nagasawa et al. 2008). This effect is a secular oscillation of the eccentricities and the inclinations of two objects, which occur when one is a distant companion, or a massive planet which has been scattered to an outer orbit by the planet-planet scattering.

An inner giant planet existing in such systems can obtain a large enough eccentricity in a long timescale, resulting in a hot Jupiter by the same tidal process as above.

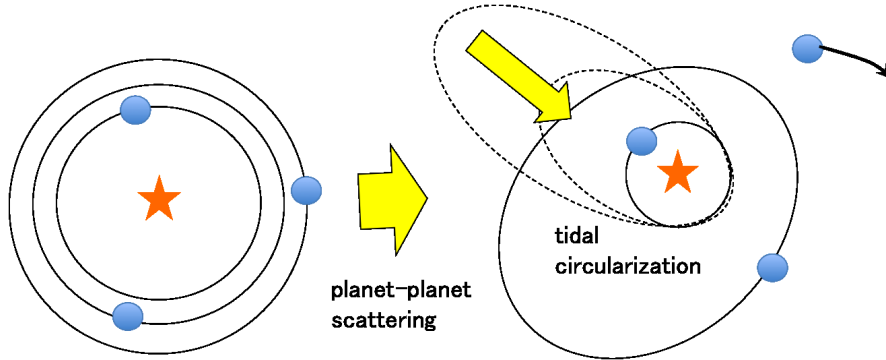


Figure 1.8: A schematic of plane-planet interaction model. Left: Several giant planets (blue circles) have formed on outer circular orbits (solid lines) around a star (orange star). Right: Through planet-planet scatterings, one of the giant planets is ejected (the top right one) and one of the remains gets a large-eccentric orbit (the outer most dotted line), which will be circularized by the stellar tidal force (the yellow arrow) to be a close-in orbit (the inner solid circle). The Kozai effect may also play an important role for a planet to get a large eccentricity, which is not shown in this figure.

1.4.3 The Rossiter-McLaughline (RM) Effect

The discovered hot Jupiters can be considered to have formed via one of such mechanisms described above. Which mechanism has actually worked on a hot Jupiter is an important issue to understand the structure of the system.

One observational evidence to distinguish the two models is measuring an angle of the two axes: the stellar spin axis and the planetary orbital axis. One can expect that the two axes would be well aligned if the hot Jupiter has formed via the disk-planet interaction because the giant planet has migrated along with the gas disk. On the other hand, if the planet-planet interaction is dominant for hot Jupiters, a wide-range distribution of the angles is expected because a planet's orbit could easily be inclined by the planet-planet scattering or by the Kozai effect (Nagasawa et al. 2008).

One of the means to measure the angle of the two axes (spin-orbit angle) is observing an anomaly of stellar radial velocities during the time when the planet transits in front of the star. During a transit, since the planet masks a part of the rotating host star, the observed radial velocity slightly shifts back or forth depending on the planet's position on the stellar disk (the Rossiter-McLaughlin (RM) effect, Rossiter 1924; McLaughlin 1924, see also Figure 1.9). That makes us possible to measure the sky-projected spin-orbit angle.

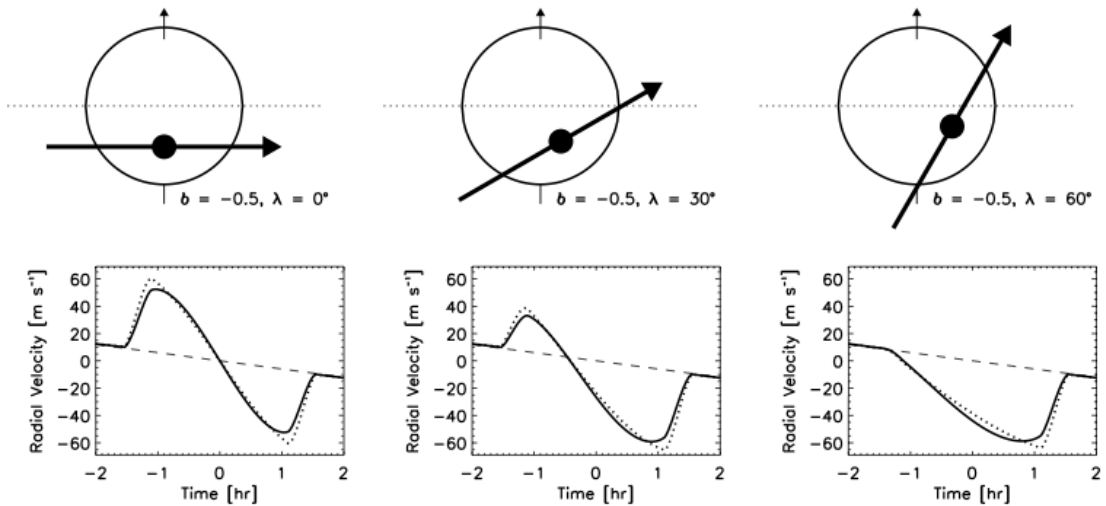


Figure 1.9: An illustration of the RM effect (from Gaudi & Winn 2007). Three different trajectories of a transiting planet on a projected rotating star (upper schematics) and the corresponding RV anomalies (lower panels) are shown. The star rotates as the left side comes to front and the right side moves toward back. The trajectories all have the same impact parameter b and produce the same light curve, but they differ in λ , which is the sky-projected spin-orbit angle, and produce different RM curves (solid lines in the lower panels). The dotted lines are for the case of no limb darkening.

To date, the sky-projected spin-orbit angles of more than 30 transiting hot Jupiters have been measured by means of the RM observations. Among them, about one third are significantly misaligned, even polar or retrograde (e.g. Narita et al. 2009; Triaud et al. 2010). At least such tilted hot Jupiters can be considered to have formed via the planet-planet interaction rather than the disk-planet interaction.

Moreover, it has been revealed that the distribution of the obliquities seems to have a trend that hot Jupiters around hot stars have high obliquities (Winn et al. 2010). Figure 1.10 shows the observed sky-projected spin-orbit angles of hot Jupiters against the effective temperatures of the host stars (from Winn et al. 2010). A transition from mainly aligned to mainly misaligned seems to occur around $T_{\text{eff}} = 6250$ K, where the authors defined as a boundary between “cool” and “hot” stars for descriptive purposes. They also proposed a possible explanation of this trend; obliquities of hot Jupiters were initially distributed in wide range in some way (e.g. the planet-planet interaction), and only cool stars have damped their obliquities through tidal dissipation in their convective zones. The bottom panel of Figure 1.10 shows the estimated mass of the outer convective zone of a main-sequence star as a function of T_{eff} calculated from Pinsonneault et al. (2001), indicating that the convective mass becomes insignificant around $T_{\text{eff}} = 6250$ K. If this explanation is true, all of the observed hot Jupiters could be explained by the planet-planet interaction model as their migration mechanisms.

1.4.4 Multiplicity of Planets in Hot-Jupiter Systems

Another possible trace of migration processes for hot Jupiters is multiplicity of planets in the hot-Jupiter systems. The migration process of a hot Jupiter should affect the stabilities of other planets in the same system, and therefore be reflected in the planetary multiplicity in the system.

Recently, it has been appeared that hot Jupiters tend to be alone in their systems, or at least not to hold other planets near themselves. Figure 1.11 shows the distributions of minimum masses (upper panel) and semi-major axes (lower panel) of planets within 200 pc discovered by RV surveys, being separated into planets in multi-planet systems (solid lines) and those in currently single-planet systems (dashed lines) (from Wright et al. 2009).

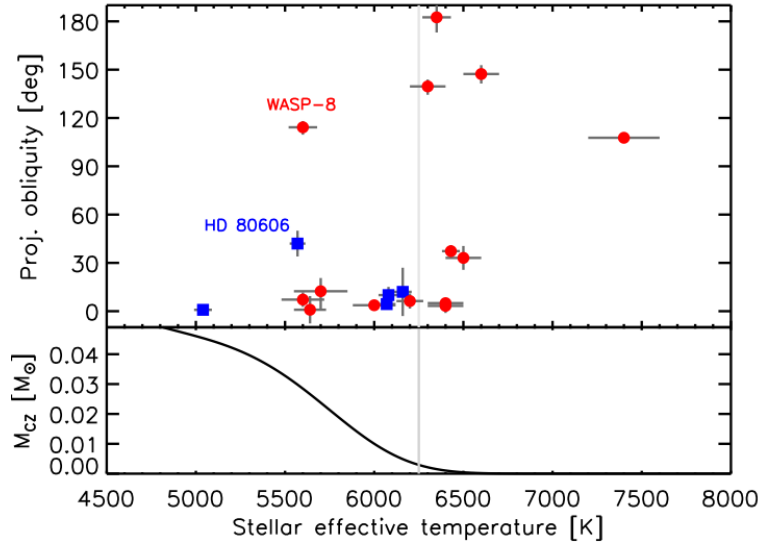


Figure 1.10: The distribution of the observed projected-spin-orbit angles of hot Jupiters (from Winn et al. 2010). Top: the projected obliquity is plotted against the effective temperature of the host star. Blue squares and red circles indicate systems discovered by RV surveys and photometric transit surveys, respectively. The gray vertical line is drawn at $T_{\text{eff}} = 6250$ K, where the authors defined as a boundary between “cool” and “hot” stars. Bottom: the mass of the convective zone of a main-sequence star as a function of T_{eff} . See the original paper for more details.

The upper panel shows an apparent excess of planets around $M_p \sin i \sim 0.01 - 0.1 M_{\text{Jup}}$ in the distribution of multi planets over that of single planets. This might indicate that low-mass planets tend to construct multi-planet systems, or conversely massive planets tend to exist alone, although this tendency may be affected by the selection bias; just that the sensitivity to additional low-mass planets in the single-planet systems have not been reached. Meanwhile, the lower panel also shows an apparent disagreement of the two distributions, where the samples are same as those in the upper panel. Especially, there is a pile-up between 0.03 and 0.07 AU in the distribution of single planets in contrast to that of the multi planets. Since most of these single planets are massive ones, the close-in piled-up single planets are mostly hot Jupiters; in other words, hot Jupiters tend to be alone in the systems, although again this tendency might be affected by the observational bias. This tendency may be a consequence that the hot Jupiters have scattered other planets away

through the planet-planet interaction processes. However, due to the potential bias, true frequency that a hot-Jupiter system holds another planet is not clear yet.

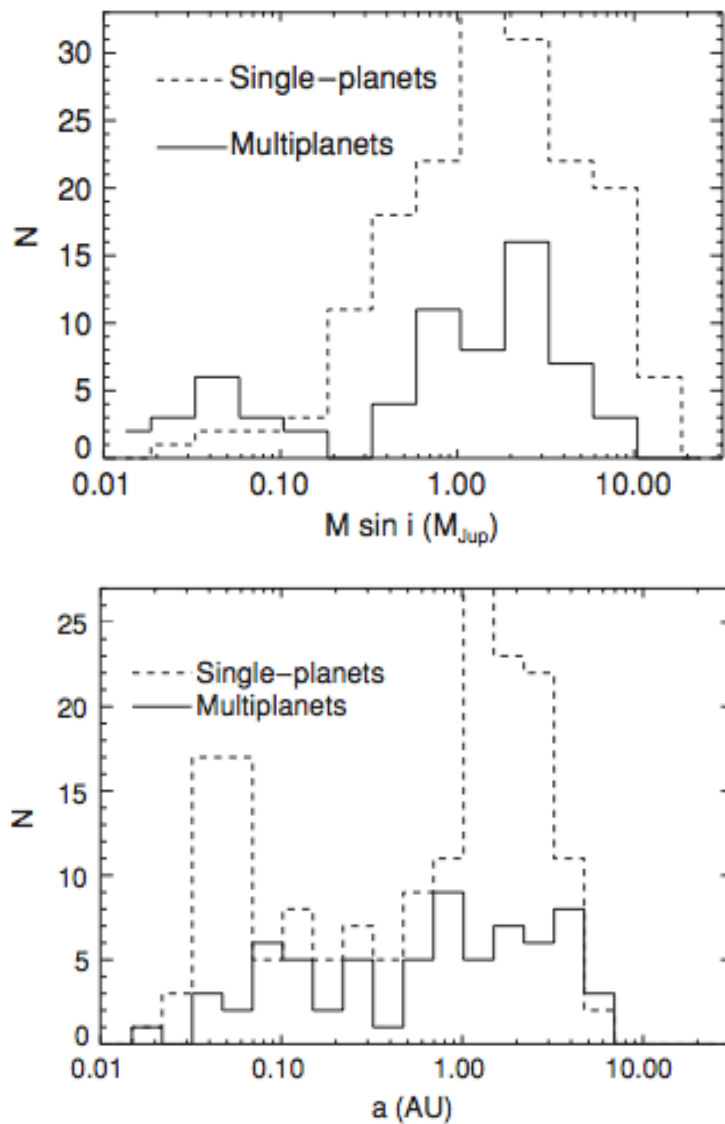


Figure 1.11: Distributions of masses (upper panel) and semi-major axes (lower panel) of discovered planets in single-planet systems (dashed line) or in multiple-planet systems (solid line) (Wright et al. 2009). The samples were selected so that the distance of systems are within 200 pc.

More recently, the *Kepler* team released more than 1,200 candidates of transiting planets from *Kepler*'s first four months' data, including small-size candidates as small as sub-

Earth radius (Borucki et al. 2011). They found that Neptune-size candidates are much more abundant rather than super-Earth size and Jupiter-size or larger candidates, and among these candidates, $\sim 34\%$ are part of multi-candidate systems. Figure 1.12 shows the distribution of the candidates in the radius-period plane. The blue dots represent the candidates in multi-candidate systems, while the red dots represent the candidates in single-candidate systems. Obviously, there is a lack of hot Jupiters in the multi candidates. This paucity is little biased as long as considering the period of $\lesssim 50$ days, and thus this tendency should be real.

This paucity must be reflected by the migration processes of the hot Jupiters. It can naturally be explained by the planet-planet interaction scenario as hot-Jupiter migration models, because a giant planet tend to scatter the neighboring planets away during its orbital evolution. However, it may also be possible to explain the paucity by the disk-planet interaction scenario, because a slowly-migrating giant planet can also tend to scatter the neighbors. In this case, because the ability to scatter them is weak compared to the planet-planet interaction, the giant planet may just stir up the surrounding planets so that they get somewhat tilted orbits where they do not transit the host star. Such planets cannot be detected by the transit method in principle.

Therefore, more careful searches for additional planets around hot Jupiters are necessary to infer which migration scenario is dominant.

1.4.5 Planetary Pairs in Mean Motion Resonances

Currently any obvious evidences for the disk-planet interaction as a hot-Jupiter migration mechanism have not been observed. On the other hand, the evidences that the disk-planet interaction might have worked on distant (not close-in) planets have been found; those are, planetary pairs captured in mean motion resonances (MMRs), which can occur

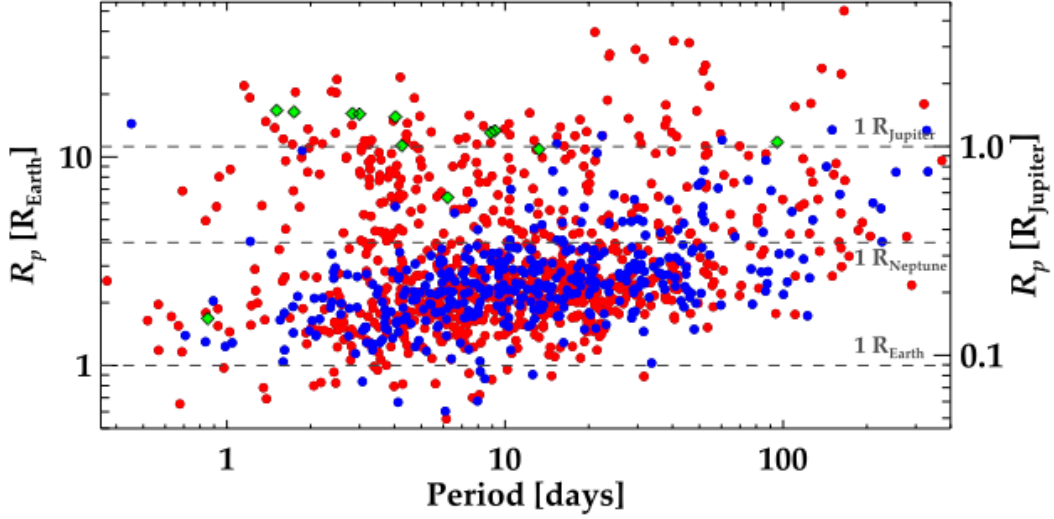


Figure 1.12: Distribution of the *Kepler* candidates in the radius-period plane (from Latham et al. 2011). Planetary candidates in single-candidate systems are plotted in red, and those in multiple-candidate systems are plotted in blue. The published *CoRoT* planets are plotted in green, for comparison, all of which are currently not in multi-transiting-planet systems.

when two planets' orbital periods are close to a ratio of two integers, e.g., Neptune and Pluto in 3:2 MMR, and GJ876 b and c in 2:1 MMR (Laughlin & Chambers 2001). In a MMR state, any of the relevant resonant angles librate so that the two planets are locked in the state and stable until external forces will break it (Murray & Dermott 1999). For the case of the first order MMR state, where the period ratio is $j : j + 1$ (j is an integer), the three resonant angles are expressed as

$$\theta_1 = (j + 1)\lambda_2 - j\lambda_1 - \omega_1, \quad (1.4)$$

$$\theta_2 = (j + 1)\lambda_2 - j\lambda_1 - \omega_2, \quad (1.5)$$

$$\theta_3 = \omega_1 - \omega_2, \quad (1.6)$$

where λ_i are the mean longitudes of the inner and outer bodies, and ω_i are the longitude of pericenter of these bodies. Many theoretical works have been done for producing MMR pairs, and showed that two planets or satellites are naturally trapped in MMRs during

their convergent migrations (e.g. Goldreich 1965; Lee & Peale 2002). In general, the probability that two planets enter a resonance depends on the relative migration rate and the eccentricities; the probability decreases with increasing the relative migration rate and eccentricities (e.g. Mustill & Wyatt 2011). Therefore, the planet-planet interaction process rarely produce resonant pairs, but the disk-planet interaction process can do it more easily.

Figure 1.13 shows a chart of exo-planetary pairs in or near MMRs. Of the 43 well-determined multi-planet systems discovered by RV surveys around normal stars, about one third include planetary pairs in or near MMRs (Wright et al. 2011). This fraction may increase by future followup observations, and such a high fraction cannot be explained by random period ratios, and therefore these planets can be thought to have experienced some sort of slow convergent migrations such as the disk-planet interaction. For instance, because generally the type-I migration is more rapid than the type-II migration, an inner giant planet migrating inward via the type-II migration and an outer small planet migrating in the same direction via the type-I migration are undergoing convergent migrations, and are naturally trapped in MMRs (e.g. Ketchum et al. 2011). Or, a giant planet undergoing the type-II migration would force (shepherd) interior planets into further inner orbits, and the inner planets could be captured in an MMR with the giant planet (Podlewska & Szuszkiewicz 2008). Note that, however, it might also happen that the surrounding small planets could be scattered into outer orbits, or be trapped at the edge of the gap opened in the gas disk by a giant planet.

On the other hand, any hot Jupiters are not included in the current sample of MMR planetary pairs. The reason is not clear yet, but it might be due to the higher migration rate for more inner planets; therefore it might be hard to be trapped in an MMR at much inner region, or a planetary pair once trapped in an MMR at outer region would migrate inward further and the MMR state might break at the inner region. However, since such migration and MMR-trapping processes are highly complicated, theoretical predictions for

the effectiveness of producing MMR pairs involving hot Jupiters include large uncertainties. Therefore, observational constraining of the probability that a hot Jupiter hold an MMR planet is highly important. In addition, if such a system is discovered, that would be the first case that a hot Jupiter would have migrated via the disk-planet interaction scenario. The transit timing variation method, which will be described in the next section, can be a powerful tool to find such resonant planets with hot Jupiters.

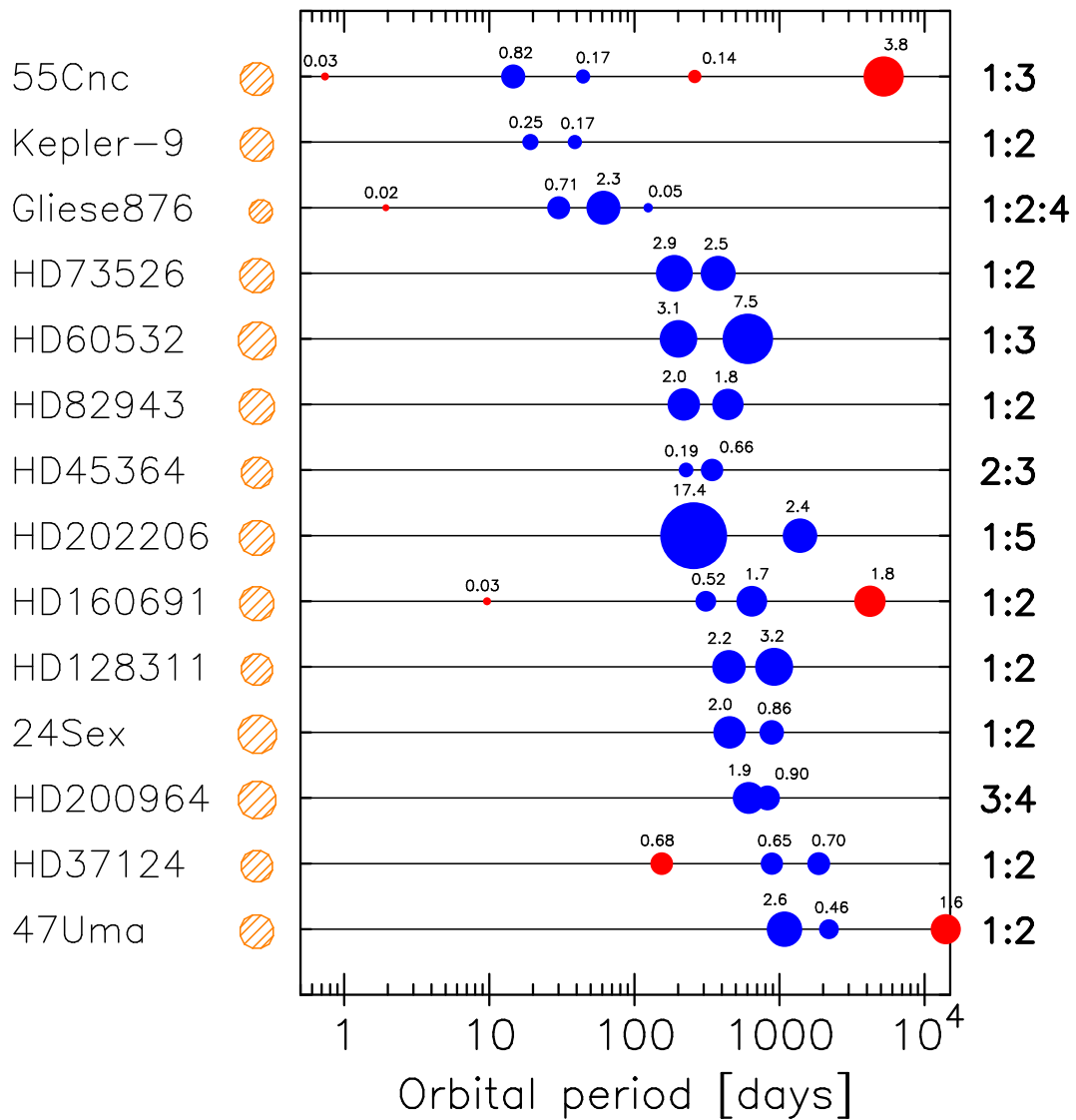


Figure 1.13: Chart of orbital periods for planetary systems which include planetary pairs in or near MMRs. The left-side texts indicate the host stars' names with their masses depicted as orange circles' radii so as to be proportional to the cube root of the stellar masses. The blue circles represent planets in MMRs (the type of MMR is indicated at the right side), and the red ones are the other (non-MMR) planets in the systems. The radius of a circle is proportional to the cube root of the minimum mass of the planet, which is also indicated above the circle in unit of Jupiter mass. The sample is partly extracted from Wright et al. (2011)

Chapter 2

Transit Timing Variations

If a transiting planet is the unique body orbiting a star, its orbital period should be constant. On the other hand, if another perturbing planets exist in the system, the orbital period will no longer be constant. Therefore, by searching for the transit timing variations (TTVs) one can find additional planets (Agol et al. 2005; Holman & Murray 2005). This novel approach to discover new extrasolar planets is called the TTV method. This method especially has high sensitivity to planes in MMRs with transiting planets, and even Earth-mass planets in such regions can be detectable with current ground-based telescopes. This method is also capable of testing the different hot-Jupiter formation mechanisms, by applying it to transiting hot Jupiters. In section 2.1, we describe a brief history of the TTV method. We explain about the planetary TTV signals and other effects to cause TTVs in section 2.2 and 2.3, respectively. In section 2.4, we describe the capability of testing the hot-Jupiter formation mechanisms by means of the TTV method.

2.1 Brief History

Phenomena of eclipse-period variations have been well known for eclipsing binaries since early times. Eclipse timings of Algol, which is the first eclipsing binary ever discovered,

was recorded at least as early as in 1782 (Goodricke 1783). Nowadays the period variations of 32-year and 1.9-year periods as well as several other irregular variations in Algol are well known. The 32-year period variations are caused by the apsidal motion of the binary and the 1.9-year period variations are due to the light travel time effect (see section 2.3), both can be attributed to the presence of a third body in the system, while the irregular period variations can be attributed to some stages of binary evolution (e.g. Frieboes-Conde et al. 1970).

The first extrasolar planets, discovered around the pulsar PSR 1257+12, were detected by using the similar phenomena; period changes of the pulsar timings caused by the perturbing planets (Wolszczan & Frail 1992). Likewise, the possibility of detecting additional planets in transit-planetary systems by the TTV method has been recognized at least as early as in 1996 (Dobrovolskis & Borucki 1996). Miralda-Escudé (2002) studied the possibilities of long-term period changes of transiting planets caused by the precessions of periastron of the planets, either due to the quadrupole moment of host stars or due to additional perturbing planets. However, the level of these variations are $\sim 1 \text{ s yr}^{-1}$, though depending on the situation, which is too small to detect with current observational facilities.

In 2005, Agol et al. (2005) and Holman & Murray (2005) both studied the feasibility of detecting additional planets by means of the TTVs, and found that even an Earth-mass planet can be detectable with current telescopes if the perturbing planet and the transiting planet are in low-order MMRs. Following their suggestions, several groups started to search for TTVs in known transiting planets. Steffen & Agol (2005) first conducted such exploration for the transit timing data of TrES-1b, and found no significant variation. They put upper limits on the mass of the hypothetical second planet from the absence of TTVs as a function of the semi-major axis ratio of the two planets, and showed that the data has a sensitivity to sub-Earth mass planets.

Since then, more than a dozen of transiting planets have been observed and analyzed to find TTVs, but most of them have failed. Maciejewski et al. (2010) observed 6 transits of the hot Jupiter WASP-3b with several 60-cm class telescopes and found that the observed transit timings cannot be explained by a constant period but by a periodic variation (see figure 2.1). They also found that the existence of a second planet of mass $\sim 15M_{\oplus}$ located close to the 2:1 MMR is the most likely scenario reproducing the observed TTVs. However, the significance of the TTVs was not so high that the detection can be believed (only three points have variations with significances of greater than 3σ), and there has been no other observation that confirmed the second-planet scenario yet. Likewise, Maciejewski et al. (2011) observed 9 transits of the hot Jupiter WASP-10b with several 0.6-2.0 m telescopes and also found a periodic variations in the transit timings (see figure 2.2). The authors claimed that the existence of an additional planet of mass $\sim 0.1 M_{\text{Jup}}$ located close to the 5:3 MMR with WASP-10b is the most likely scenario to explain the observed TTVs. Although any other photometric observations have not confirmed the claimed TTVs, the significance of the TTVs is higher than that of WASP-3b, and the residuals of RV data for WASP-10 support the most likely scenario. If at least one of these TTV detections will be confirmed by future followup observations, that would be the first TTV detection among transiting hot Jupiters, and moreover, the additional planet would be the first one existing close to an MMR with a hot Jupiter. Therefore this fact would be the first positive evidence that at least one hot Jupiter has formed via the disk-planet interaction scenario (see section 2.4).

In 2010, the *Kepler* team announced the first firm detection of TTVs in Kepler-9b and c, whose TTV signals reached as large as tens of minutes due to the fact that the two planets are near 1:2 MMR (see Figure 2.3, Holman et al. 2010). Several RV observations obtained for the system also supported the nature of the TTV signals and were used to determine the masses of these planets combined with the TTV data. More recently, Kepler-11 system was announced to host six transiting planets, of which five show significant TTVs that

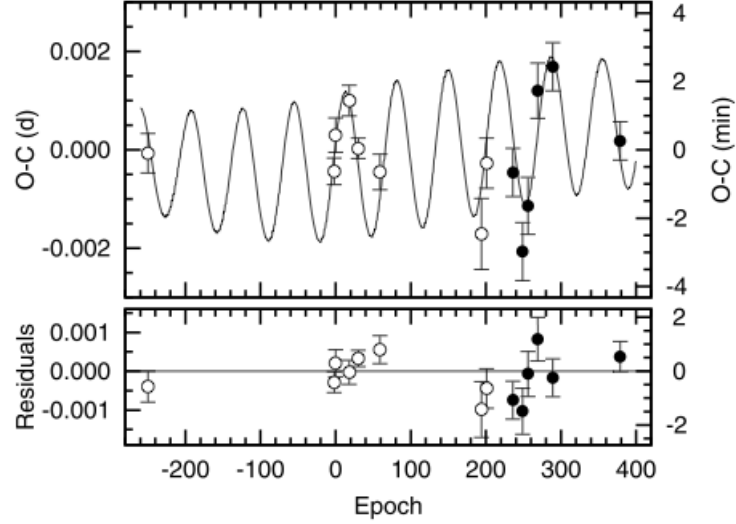


Figure 2.1: Observed TTVs in WASP-3b (from Maciejewski et al. 2010). Transit timing residuals from a constant period are shown in the upper panel. Black points are Maciejewski’s data, while open circles are the data of previous works. The solid curve represents the most likely TTV model caused by a $\sim 15 M_{\oplus}$ second planet near 2:1 MMR with WASP-3b. Their residuals are shown in the lower panel.

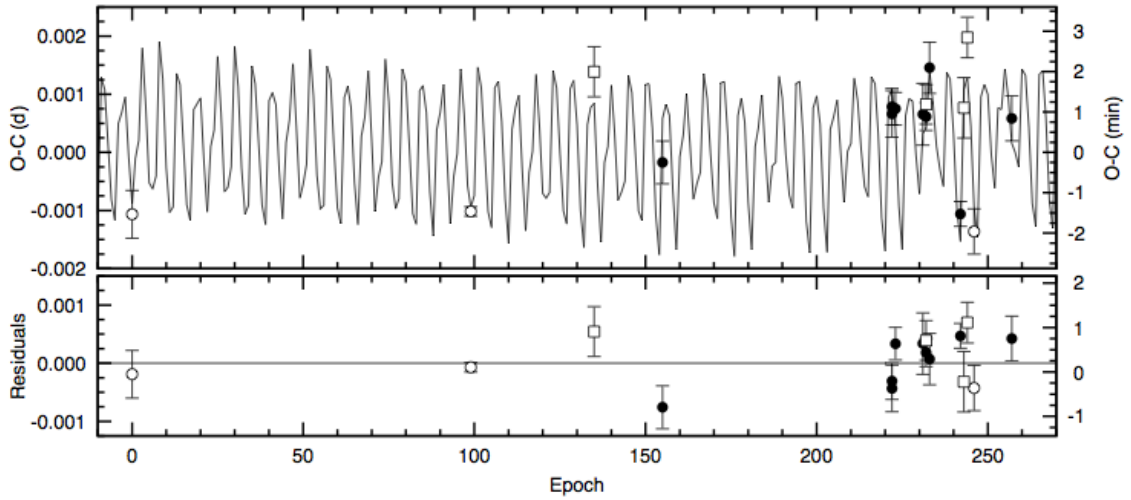


Figure 2.2: Observed TTVs in WASP-10b (from Maciejewski et al. 2011). The meaning of the panels and symbols are same as Figure 2.1, but the open squares are the literature’s data reanalyzed by Maciejewski et al. The solid line is based on the best second-planet model with the mass of $\sim 0.1 M_{Jup}$ and the location of near 5:3 MMR with WASP-10b.

were used to determine their masses without any RV observations (Figure 2.4, Lissauer et al. 2011). Note, however, that any planets in the both systems are not hot Jupiters but moderately outer “cool Jupiters” (Kepler-9b, c) or “super Earths” (Kepler-11b, c, d, e, f). Therefore, currently any conclusive TTVs have not been detected in any transiting hot-Jupiters.

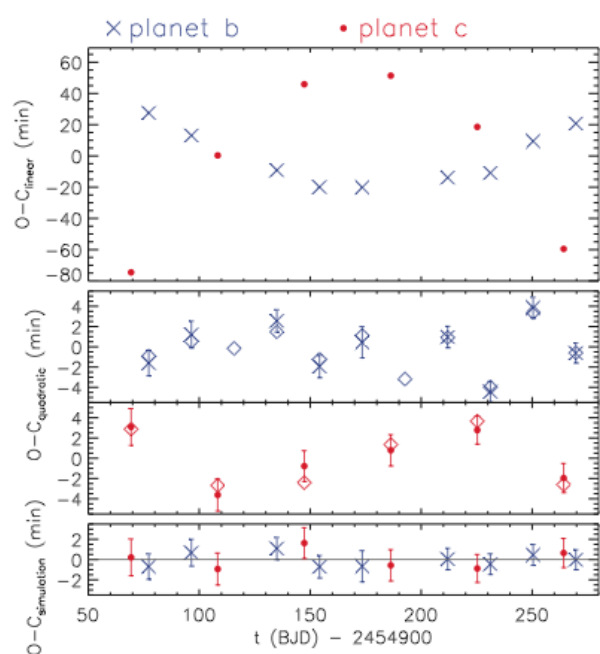


Figure 2.3: Offset of the observed transit times for Kepler-9b (blue \times symbols) and Kepler-9c (red dot symbols) compared to those calculated with linear ephemerides (top panel) and quadratic ephemerides (middle panel) (from Holman et al. 2010). The diamond symbols indicate the best-fit dynamical model. Residuals from the dynamical models are shown in the bottom panel.

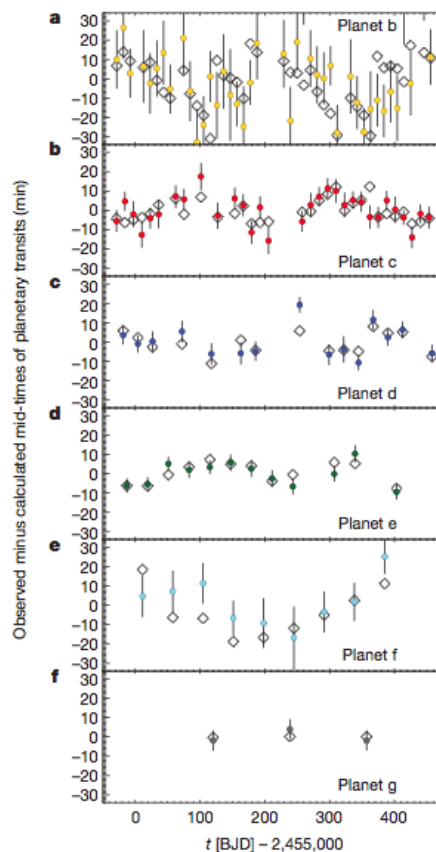


Figure 2.4: Observed transit times minus a calculated linear ephemeris are plotted as dots with 1σ error bars (from Lissauer et al. 2011). The panels of **a** through **f** show data of Kepler-11b (the inner most planet) through Kepler-11g (the outer most one).

2.2 Planetary TTV signals

When a second planet or a companion exists in a transiting-planetary system, several effects can cause TTVs. These effects are basically classified into three: (a) the light travel time effect (e.g. Irwin 1959); (b) secular perturbations (e.g. Miralda-Escudé 2002); (c) instantaneous plane-planet or planet-star gravitational interactions. In the case of (a) and (b), the libration periods of detectable TTVs become so long that long-term observations in the timescale of tens to hundreds of years are needed to recognize them. In this paper we treat only the case (c) as planetary TTV signals. In addition, throughout this paper, we adopt an assumption that the two planets are coplaner and the orbital plane is perfectly edge-on for simplicity.

Agol et al. (2005) investigated the magnitude of TTVs caused by the case (c), and derived analytical formulae in the form of standard deviation of the transit timings, here expressed as σ_{TTV} , for several limiting cases: (i) interior perturbing planets with much smaller periods; (ii) exterior perturbing planets on eccentric, much larger-period orbits; (iii) both planets on circular orbits with arbitrary period ratio but not in resonance; (iv) planets on initially circular orbits locked in MMRs. In addition, they investigated the TTV magnitude by means of numerical simulations for an another case; (v) close planets with non-zero eccentricities. We summarize their findings for the cases (i) through (v) in the following sections of 2.2.1 through 2.2.5, respectively.

2.2.1 Interior Perturbing Planets with Much Smaller Periods

In this case, planet-planet perturbations are negligible and the main effect is wobble of the star on the sky plane due to the interior planet. Approximating that the eccentricities

of the two planets are zero, the TTV magnitude is given by

$$\begin{aligned}\sigma_{\text{TTV}} &= \frac{\mu_2 a_2 P_1}{2^{3/2} \pi a_1} \\ &\sim 0.1 \left(\frac{\mu_2}{10^{-5}} \right) \left(\frac{a_2/a_1}{0.5} \right) \left(\frac{P_1}{3\text{days}} \right) \text{ [s]},\end{aligned}\quad (2.1)$$

where μ is the planet-to-star mass ratio, a is the semi-major axis, and P is the orbital period, and the subscripts ‘1’ and ‘2’ denote the transiting and perturbing planets, respectively. Note that this kind of perturbations would disappear if the periods have a ratio $P_1 : P_2$ of the form $j : 1$ for some integer j , because the wobble of the star would always have only the radial component at the times of transit.

2.2.2 Exterior Perturbing Planets on Eccentric, Larger Orbits

A perturbing planet at a large distance from an inner transiting planet changes the effective mass of the inner binary (transiting planet + star) by $-(1/2)M_2(a_1/r_2(t))^3$, where M is the mass and $r(t)$ is the distance from the star at the time t . This works as a slight increase in the period of the inner planet. Therefore the non-zero eccentricity of the outer planet causes the orbital period of the inner planet to vary. The standard deviation of the TTVs produced in the inner planet over the period of the outer planet is given by

$$\sigma_{\text{TTV}} \sim \frac{1}{3} \left(\frac{a_2}{a_1} \right)^{-3/2} \frac{\mu_2 e_2 P_1}{(1 - e_2^2)^{3/2}},\quad (2.2)$$

where e is the eccentricity (for a more accurate formula, see equation (27) of Agol et al. 2005). This approximation breaks down for $a_2(1 - e_2) \lesssim 5a_1$ and $e_2 \lesssim 0.05$. Adopting the values of $P_1 = 3$ [d], $\mu_2 = 10^{-3}$, $a_2/a_1 = 15$, and $e_2 = 0.5$, one gets $\sigma_{\text{TTV}} \sim 1$ [s].

2.2.3 Both Planets on Initially Circular, non-MMR Orbits

In this case, the planets interact most strongly at conjunction, so the perturbing planet causes a radial kick to the transiting planet, giving it eccentricity. The change in eccentricity causes a change in the orbital period, which produces TTVs. When the planets are not exactly on resonance, the longitude of conjunction will drift with time, causing the kicks to cancel after the longitude drifts by $\simeq \pi$ in the inertial frame. Thus, the TTV amplitude grows over a time equal to half of the circulation-period of the longitude of conjunction. The closer the planets are to a resonance, the longer the period of circulation and thus the larger the TTVs become. For halfway between two successive first-order resonances, the timing deviation becomes

$$\sigma_{\text{TTV}} \sim 0.7 \mu_2 [a_1 / (a_1 - a_2)]^2 P_1. \quad (2.3)$$

Figure 2.5 shows the analytical solutions derived from this equation, with a numerical simulation of the standard deviation of the TTVs done by Agol et al. (2005). This figure also shows the case that the two planets are in MMRs, which will be described next.

2.2.4 Planets on Initially Circular Orbits Locked in MMRs

This is the most interesting case because some planetary systems are actually known to be in MMRs, and perturbations induced in such systems become quite large. Considering a first order, $j : j + 1$, resonance (where j is an integer) of two planets of which massive one is the transiting planet, the two planets have successive conjunctions at exactly the same longitude in the inertial space. Strong interactions that occur at conjunctions lead to build up the eccentricity of the planets, and cause a change in their semi-major axis and period. The libration period of the transit period becomes $\sim j^{-4/3} \mu_1^{-3/2} P_1$, leading to long-period

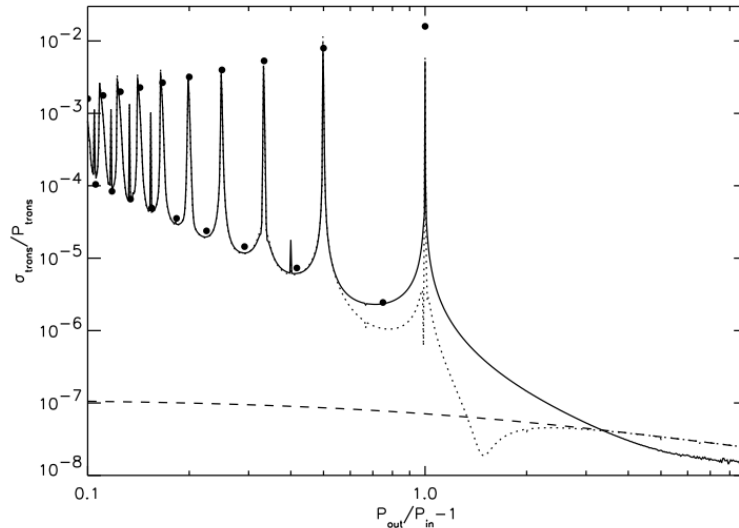


Figure 2.5: Standard deviation of TTVs for two planets of mass $M_1 = 10^{-5}M_*$ and $M_2 = 10^{-6}M_*$ on initially circular orbits in units of the period of the transiting planet, as a function of $P_{\text{out}}/P_{\text{in}} - 1$, where P_{out} and P_{in} are periods of outer and inner planets (from Agol et al. 2005). σ_{trans} and P_{trans} in this figure correspond to σ_{TTV} and P_1 in our context, respectively. The solid (dotted) line is the numerical calculation for the inner (outer) planet averaged over 100 orbits of the outer planet. The dashed line is equation (2.1). The large dots are equation (2.4) on MMRs and equation (2.3) on halfway between MMRs.

TTVs. An analytical formula of the maximum TTVs that occur at an exact resonance is given by

$$\sigma_{\text{TTV}} \sim \frac{P_1}{4.5j} \frac{M_2}{M_1 + M_2}, \quad (2.4)$$

where the factor of $1/4.5$ was determined by a fit to the data of numerical simulations shown in Figure 2.5. Figure 2.5 also shows the standard deviations of TTVs for first-order MMRs calculated from equation (2.4), indicating that the TTV signals reaches tens to hundreds of seconds in the case that P_1 , M_1 , and M_2 are several days, $10^{-5}M_*$, and $10^{-6}M_*$, respectively.

2.2.5 Close Planets with Non-zero Eccentricities

When either of the eccentricities of the two planets is large enough, higher-order resonances become important. Because the parameter space becomes too large to treat it analytically, Agol et al. (2005) conducted numerical calculations of TTV signals for various eccentricities and periods of an Earth-mass perturber lying exterior of the transiting planet HD 209458b, which has a mass of $0.67 M_{\text{Jup}}$ and a circular orbit with a period of 3.5 d. The results are shown in Figure 2.6. One can see that the number of regions where TTV signals are enhanced increases as the eccentricity of the perturbing planet increases. This map can be applied to other systems with different masses and periods, since the timing variations scales as $\sigma_{\text{TTV}} \propto P_1 M_2$ (except for planets in MMRs).

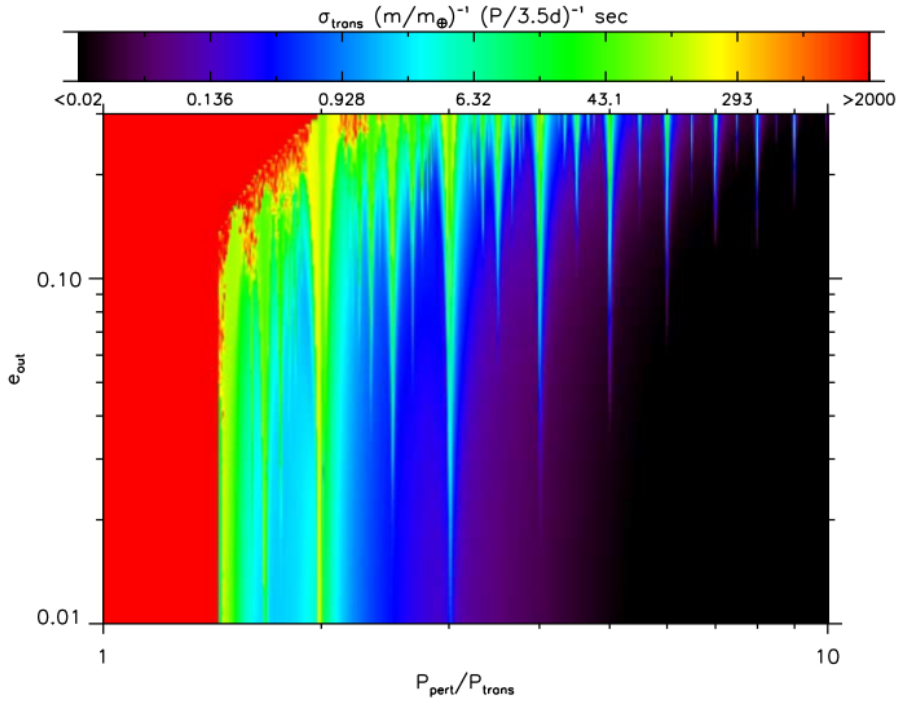


Figure 2.6: TTV amplitudes of HD 209458b due to perturbations induced by an exterior Earth-mass planet with various eccentricities and periods (from Agol et al. 2005). e_{out} denotes the eccentricity of the perturber. The clear red region becomes chaotic (unstable).

2.2.6 Planetary Detection Sensitivity

The possibility of detecting additional planets by using the TTV method depends strongly on (i) period of the transiting planet, (ii) closeness to an MMR of the two planets, and (iii) eccentricities of the planets. The detectability of such planets also depends on the measurement errors of transit timings and the number of transit timing measurements. In addition, the observations should be made over a time longer than the period of the TTVs.

The uncertainty of a transit mid-time measurement depends mainly on diameter of the telescope, brightness of the host star, transit depth, and ingress/egress duration of a transit. When a series of continuous photometric observations of a planetary transit is done with a photometric precision of σ_{ph} and a sampling rate of Γ , then the transit timing precision, σ_{T_c} , is approximated by

$$\sigma_{\text{T}_c} \simeq (t_e/2\Gamma)^{1/2} \sigma_{\text{ph}} (R_p/R_*)^{-2}, \quad (2.5)$$

where t_e is the ingress/egress duration (Ford & Gaudi 2006). Assuming a typical hot-Jupiter case of $R_p/R_* = 1\%$ and $t_e = 0.2$ hours, one can expect to get $\sigma_{\text{T}_c} \simeq 15$ s when one observes the stellar brightness with $\sigma_{\text{ph}} = 0.1\%$ and $\Gamma = 1 \text{ min}^{-1}$.

Compared to this, as seen in Figure 2.5 and 2.6, the TTV signals can reach a few minutes even if the perturber is an Earth-mass planet as long as it lies near low-order MMRs or has high eccentricity. Considering a simple case of a transiting hot Jupiter with a 3-d period that is perturbed by a lighter, exterior planet on a circular orbit in the 2:1 MMR, the standard deviation of the TTVs is expected as

$$\sigma_{\text{TTV}} \sim 3 \left(\frac{M_2}{M_{\oplus}} \right) \text{min}. \quad (2.6)$$

In this case, the libration period is estimated as

$$t_{\text{cycle}} \sim 150 \left(\frac{M_1}{M_{\text{Jup}}} \right)^{-2/3} \text{ d.} \quad (2.7)$$

Therefore, the detection of such a low-mass planet lying an MMR is feasible with observations of several months or years.

Figure 2.7 shows a comparison of planetary detection sensitivity for several techniques to a secondary planet in HD 209458b, calculated by Agol et al. (2005). In the figure, the solid, dashed, dotted lines are for the TTV, the astrometric, and the RV methods, respectively. The signal-to-noise ratio of 10 was required as a detection threshold, and for the RV and the astrometric methods, the measurement precision of 0.5 m s^{-1} and $1 \mu\text{arcsec}$ were assumed, respectively. As one can see, the TTV method is much more sensitive than the other methods at low-order MMRs.

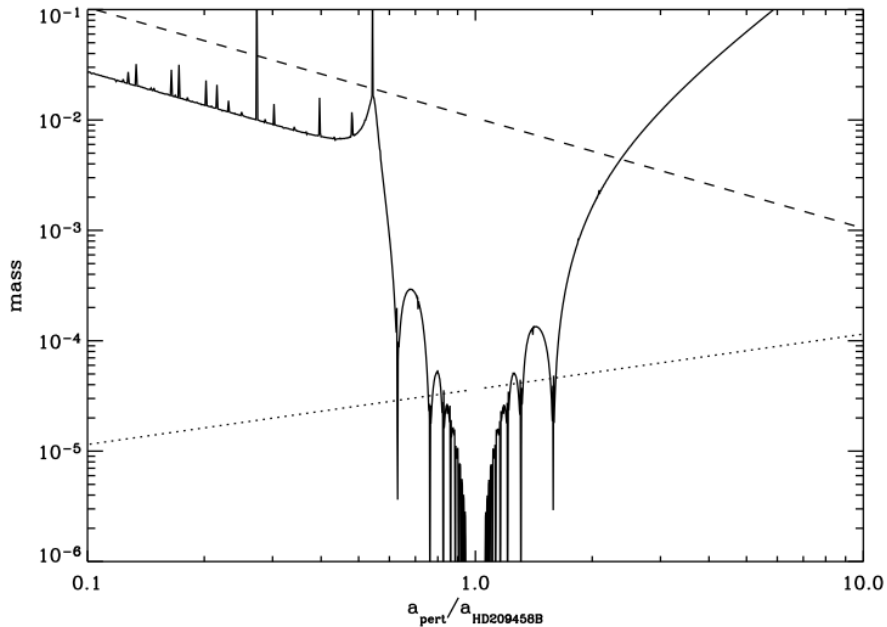


Figure 2.7: Planetary detection sensitivity of several techniques to a secondary planet in HD 209458b (from Agol et al. 2005). The vertical axis is the second-planet mass in units of M_{\odot} , and the horizontal axis is the ratio of the semi-major axes of the planets. The solid, dashed, and dotted lines are for the TTV, astrometric, and RV methods, respectively.

2.3 Other Effects Causing TTVs

TTVs can be caused by other effects rather than by perturbing planets. There are several types of effects, such as the light travel time effect (e.g. Irwin 1959), the orbital precessions of the transiting planet due to several effects: such as the quadrupole moment of the host star, secular perturbations caused by a second planet, the general relativistic effect, tidal deformations induced on the star and the planet, and variations of the quadrupole moment of the star driven by stellar activity (Miralda-Escudé 2002; Jordán & Bakos 2008; Watson & Marsh 2010), tidal decay of the transiting planet (Hellier et al. 2009), and perturbations induced by smaller bodies such as exo-moons (Kipping 2009b). Nevertheless, all these effects are negligible compared to the planetary TTV signal of more than a few seconds.

Here we explain about the light travel time effect, which can be significant when a massive planet or a companion exists on an outer orbit, although it is still negligible unless we consider long-term TTVs. The second, large distant companion changes the distance of the host star with respect to the observer, leading to variations of observed periods of the transiting planet (e.g. Irwin 1959). Assuming a circular orbit of the second companion, the TTV amplitude of this effect is expressed as

$$\Delta t = 0.5 \left(\frac{a_c}{\text{AU}} \right) \left(\frac{M_c \sin i_c}{M_{\text{Jup}}} \right) \left(\frac{M_{\odot}}{M_*} \right) [\text{sec}], \quad (2.8)$$

where a_c , M_c , and i_c are the semi-major axis, the mass, and the orbital inclination of the second companion, respectively, and M_* is the mass of the host star.

2.4 Test for Hot-Jupiter Formation Mechanisms

As discussed in Section 1.4.4, detecting another planets around a hot Jupiter could be an important evidence that the hot Jupiter has migrated via the disk-planet interaction model.

Especially, as discussed in Section 1.4.5, planets in MMRs with a hot Jupiter could be a more important evidence of the disk-planet interaction model because the planet-planet interaction process is generally not likely to form an MMR-planetary pair. However, none of such planets has clearly been detected in any hot-Jupiter systems so far. This fact disfavors a certain type of migration models, i.e., the models which can produce abundant planets surviving around hot Jupiters. However, since many of the RV observations did not have sufficient sensitivities to low-mass planets, and the multi-planets or their candidates detected by the space-based transit surveys are limited to only coplaner ones, more detailed observations are still needed.

The TTV method can detect even somewhat inclined (non-transiting) planets, and even Earth-mass planets if they are in or near low-order MMRs. Therefore, TTV observations for hot Jupiters can be an independent tool to check the loneliness of hot Jupiters, and therefore to test for the hot-Jupiter formation mechanisms. As of June 2011, transit timings of about 15 transiting hot Jupiters have been observed to search for TTVs, and only two of them have been argued to show significant TTVs: WASP-3b and WASP-10b. Table 2.1 lists the transiting hot Jupiters for which substantial transit timings have been observed; we select a sample of planets which have masses above $0.5 M_{\text{Jup}}$ and periods below 10 days, as well as for which more than 7 timing data with uncertainties of less than 90 s have been obtained. Note that the hot Jupiters which have non-zero eccentricities (e.g. XO-3b) and have additional, outer planets (e.g. HAT-P-3b) are excluded from this sample, because these may be signs of the planet-planet interaction model.

In this paper, we present our photometric observations of another transiting hot Jupiter, WASP-5b. The rest of this paper is organized as follows. Chapter 3 describes about the MOA project and its instruments as well as a study of the noise property. In Chapter 4, we show our observations and data reduction. Chapter 5 and Chapter 6 present a transit light curve analysis and a combined analysis with published data, respectively.

An analysis of upper limits on the mass of the second companion is shown in Chapter 7. Discussion and conclusion are described in Chapter 8 and Chapter 9, respectively.

Table 2.1: List of hot Jupiters for which transit timing analyses have been done.*

Name	$M [M_{\text{Jup}}]$	P [d]	λ [deg]	N_{tr} ^a	Second-planet mass or its upper limit [M_{\oplus}] (MMR) ^b	Reference
CoRoT-1b	1.03	1.51	-77 ± 11	35 (35)	< 1 (2:1)	Csizmadia et al. (2010)
HAT-P-3b	0.60	2.90	—	8 (8)	< 0.33 (1:2) ^c	Nascimbeni et al. (2011)
HAT-P-4b	0.68	3.06	—	12 (12)	—	Christiansen et al. (2011)
HD 189733b	1.15	2.22	$0.85^{+0.05}_{-0.10}$	49 (41) ^d	< 0.15 (1:2)	Hrudková et al. (2010)
HD 209458b	0.714	3.52	-4.4 ± 1.4	28 (28)	< 0.3 (1:2, 2:1)	Miller-Ricci et al. (2008)
OGLE-TR-111b	0.54	4.01	—	16 (12)	< 0.5 (1:2, 2:1)	Hoyer et al. (2011)
OGLE-TR-132b	1.17	1.69	—	10 (8)	$< 5\text{--}10$ (1:2, 3:2)	Adams et al. (2011)
TrES-1b	0.76	3.03	30 ± 21	16 (16)	< 1 (3:2, 2:1)	Rabus et al. (2009)
TrES-2b	1.25	2.47	-9 ± 12	18 (18) ^e	< 0.11 (1:2)	Kipping & Bakos (2011)
TrES-3b	1.91	1.31	—	24 (24)	< 0.71 (2:1) ^f	Christiansen et al. (2011)
WASP-3b	2.04	1.85	$3.3^{+2.5}_{-4.4}$	15 (15)	~ 15 (2:1)	Maciejewski et al. (2010)
WASP-4b	1.24	1.34	4^{+34}_{-43}	15 (13) ^g	—	Sanchis-Ojeda et al. (2011)
WASP-10b	3.06	3.09	—	16 (16)	~ 30 (5:3)	Maciejewski et al. (2011)
XO-1b	0.92	3.94	—	31 (25)	< 1 (2:1)	Burke et al. (2010)

* A sample of transiting hot Jupiters are selected with three criteria: (i) planetary mass is above $0.5 M_{\text{Jup}}$; (ii) orbital period is less than 10 days; (iii) more than 7 transit-timing measurements with their uncertainties of less than 90 s have been obtained. Note that the hot Jupiters which have non-zero eccentricities (e.g. XO-3b) and have additional, outer planets (e.g. HAT-P-3b) are excluded from this sample, because these may be signs of the planet-planet interaction model.

^a The number of transit timing measurements analyzed in the literature. The number in parentheses represents that of timing data whose uncertainties are less than 90 s.

^b For WASP-3b and WASP-10b, the claimed mass of the second planet and its location (in parentheses) are listed. For the others, the most stringent upper limit on the second planet's mass over the period and its location (in parentheses) are listed.

^c Constrained by Gibson et al. (2010).

^d In Section 8.3, we used 34 of them excluding those derived by Bakos et al. (2006) due to poor quality.

^e In Section 8.3, we added 22 timing data derived by some peer-reviewed literatures, which are listed in Table 5 of Kipping & Bakos (2011) but were not used for estimating the upper-limit mass.

^f Constrained by Gibson et al. (2009).

^g In Section 8.3, we excluded the two poor timing data.

Chapter 3

The MOA Project and Instruments

3.1 The MOA Project

Microensing Observations in Astrophysics (MOA) is a Japan–New Zealand collaboration, which started in 1996 aiming for detecting gravitational microlensing events caused by MAssive Compact Halo Objects (MACHOs), following the Paczyński’s suggestion (Paczynski 1986) and the foregoing successive observations by several groups (MACHO, EROS, OGLE and DUO). MOA had started observations of stars toward the Galactic Bulge and the Large Magellanic Cloud by using the 61-cm Boller and Chivens (B&C) telescope (Figure 3.1), which is located at Mt. John University Observatory (MJUO) in New Zealand. The telescope had initially been equipped with a mosaic CCD camera of nine $1\text{k} \times 1\text{k}$ CCD chips (MOA-cam1), which was upgraded to a new one consisting of three $2\text{k} \times 4\text{k}$ CCD chips (MOA-cam2, Yanagisawa et al. 2000) in 1998. In 2004, the 1.8-m MOA-II telescope was newly built beside the B&C dome, equipped with a new camera consisting of ten $2\text{k} \times 4\text{k}$ CCD chips (MOA-cam3, Sako et al. 2008), aiming for solving the problem of MACHOs’ fraction in the galaxy and detecting planetary microlensing events by monitoring much more stars with higher sampling rate. From the spring of 2006, steady-survey observations had begun with the MOA-II telescope instead of the B&C telescope, and after that,

the MOA-cam2 on the B&C telescope was replaced with a fast-readable $1\text{k} \times 1\text{k}$ CCD camera (Apogee cam), and the focal ratio of the telescope was also changed from F/6.25 to F/13.6, in order to follow-up notable microlensing events. After a while we noticed the capability of TTV observations by using the B&C telescope with Apogee cam, and from the spring of 2008, we started observations of planetary transits during low-priority observation time (i.e., there is no notable ongoing microlensing event). Table 3.1 shows information of MJUO.

Table 3.1: Information of MJUO

Mt. John University Observatory (MJUO)	
Longitude	+170°27'.9
Latitude	-43°59'.2
Altitude	1029 m
Typical Seeing ^a	2".0
Observational Efficiency ^b	38 %

^a The median value of seeings measured for the MOA-II data over the period between Jul. 2008 and Nov. 2010.

^b The ratio of the telescope running time to the total night time for the MOA-II telescope over the period from Jul. 2008 to Nov. 2010, excluding the time from Nov. 2009 through Jan. 2010.

3.2 Telescope and Camera

B&C is a 61-cm Ritchey-Chrétien Cassegrain telescope with the focal length of 8.3 m. Apogee-cam, the camera currently mounted on the telescope, is Alta U47 of the Apogee Image Systems inc., which has a $1\text{k} \times 1\text{k}$ CCD chip with the pixel size of $13 \mu\text{m}$. Thus this system provides the pixel scale of $0''.33$ and the FOV of $5'.5 \times 5'.5$. The readout time of the camera is about 5 s. The system has a filter-wheel in which four filters are equipped:

Bessel V , R , and I , and a clear one. The telescope, the camera, and the filter-wheel are all remotely controllable. The system does not have any realtime auto-guide system, and the telescope tracking error becomes up to $\sim 1.5 \text{ pixel min}^{-1}$ ($0'.5 \text{ min}^{-1}$). Table 3.2 summarizes the properties of the telescope and the camera used in this study.

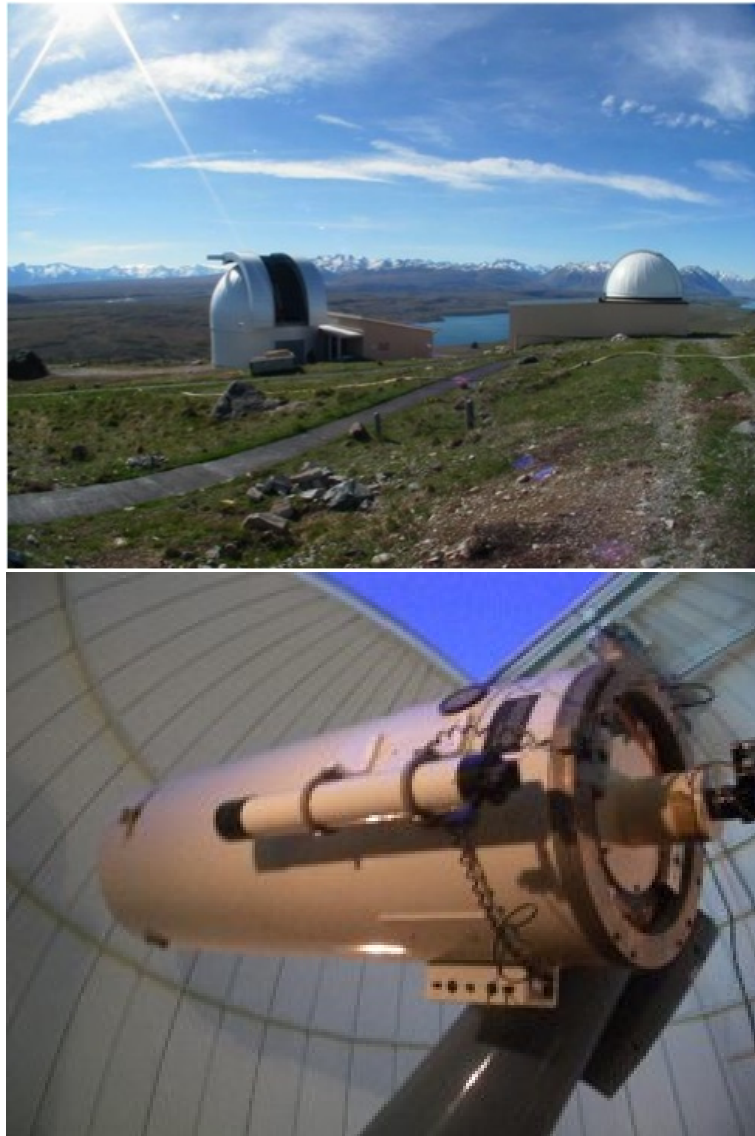


Figure 3.1: The B&C and the MOA-II domes (right and left, respectively, in the left figure), and the B&C telescope (right figure).

Table 3.2: Properties of the Telescope System

The Boller and Chivens (B&C) telescope	
Telescope type	Ritchey-Chrétien Cassegrain
Aperture [m]	0.61
Focal length [m]	8.3
Tracking error [arcsec min ⁻¹]	≤ 0.5
Apogee-cam	
Product name	Alta U47 (Apogee Image Systems inc.)
Detector	peltier-cooled Charge Coupled Device (CCD)
Array size [pixel ²]	1,024 × 1,024
Pixel size [μm ²]	13 × 13
Readout time [s]	5
Readout noise [e ⁻ pixel ⁻¹]	11.5
Gain [e ⁻ ADU ⁻¹]	1.19
Dark noise [e ⁻ pixel ⁻¹ s ⁻¹]	~0.03
Temperature [degree]	-40
Total	
Field of view [arcmin ²]	5.5 × 5.5
Pixel scale [arcsec pixel ⁻¹]	0.33

3.3 Study of Noise Property

In TTV observations, we measure the central times of planetary transits from continuous photometric observations over the course of the transits. Since the depth of a planetary transit is generally very shallow (1.2 % for WASP-5b), careful observations are necessary so as not to bury the transit and to measure the mid-transit time with meaningful precision. Therefore, it is important to reduce photometric noises as much as possible. There exists many sources of photometric noises, such as instrumental, atmospheric, and astronomical origins as well as the random photon noise. In this section we estimate the impact of instrumental-origin noises on the photometry.

3.3.1 Readout Noise

The instrumental noises are produced mainly from the CCD readout noise, the dark-current noise, and incompleteness of the pixel-to-pixel sensitivity calibration.

The readout noise is a random noise introduced in each pixel during the readout process, due to imperfect conversion from an analog signal to a digital number, or unwanted electrons produced by the electronics (Howell 2006). This noise level can be estimated by using a statistical relation between the mean flux and the variance over an uniform image, which can be produced as follows. First, an uniformly-illuminated image is produced in some way (often by using diffused light reflected by a white board fitted inside the dome). Next, the image is divided by an unity-mean master-flat-field image, which is generated by stacking a lot of uniformly-illuminated images so that the statistical fluctuation on the master-flat image is smoothed out and the image responds only to the pixel-to-pixel sensitivities and the optical-system non-uniformity. Ideally, the fluctuations of the fluxes on the generated uniform image can be explained only by the poisson noise of photon; on the other hand, the actual fluctuations can be higher than the ideal one due to the production of the readout noise. Taking the readout noise into account, the standard deviation, σ_F ,

of the fluxes over the uniform image is expressed as

$$\sigma_F^2 = \frac{\sigma_p^2 + \sigma_{\text{read}}^2}{g^2}, \quad (3.1)$$

where σ_p is the poisson photon noise in unit of photoelectron, σ_{read} is the readout noise in unit of electron, and g is the analog-to-digital conversion factor (or gain) in unit of electron AUD⁻¹. Here, using the statistical relation of $\sigma_p = \sqrt{gF}$, where F is the mean flux of the image, equation (3.1) is rewritten by

$$\sigma_F^2 = \frac{F}{g} + \frac{\sigma_{\text{read}}^2}{g^2}. \quad (3.2)$$

Since the actual value of g is also unknown here, g and σ_{read} are simultaneously determined by fitting a linear function to a set of the values of F and σ_F^2 , which is provided from a number of uniform images of which the mean-flux levels are changed variously. The actual exercise for Apogee-cam was done as follows.

First, a filament lamp was set in the dome in order to make an (approximative) uniform source by diffusely reflecting the light on a white screen fitted on a wall inside the dome. Then the telescope was directed to the screen, and the voltage of the lamp was adjusted so that a taken image began to saturate with the exposure time of around 60 s. Next, we took a series of exposed images, changing the exposure times such as 1 s, 5 s, 10 s, ..., and 60 s. For each exposure time five images were taken. For 40-s exposure time, additional 35 images were taken to create a master flat-field image combined with the previously obtained 5 images. 40 zero-second bias images were also taken to create a master bias image, which was subtracted from each of the exposed images. Then each of the bias-subtracted images was divided by the master flat-field image to make an uniform image, from which the mean flux and its variance were measured. Figure 3.2 shows a plot of the measured mean-fluxes and variances. For a same exposure time, the five data points are seen as a cluster except

for the 60-s images, whose data points are dispersed due to saturation. Therefore we found that the saturation level of the CCD lies between 52,000 and 55,000 ADU. The plot was then fitted by a linear function excluding the 60-s data, providing the results of $g = 1.19$ electrons ADU^{-1} and $\sigma_{\text{read}} = 11.5$ electrons pixel^{-1} . Note that the forty 40-s images were also not used for the fit, because each 40-s image is included in the master flat-field image.

On the photometry of stars, the impact of the readout noise of 11.5 electrons pixel^{-1} is small relative to the photon noise. For instance, when receiving 1,000,000 photons coming from a star with 300 pixels, the expected photon noise is 1,000 photoelectrons. In contrast, the expected readout noise is $11.5 \times \sqrt{300} \simeq 200$ electrons, which is about 5 times less than the photon noise.

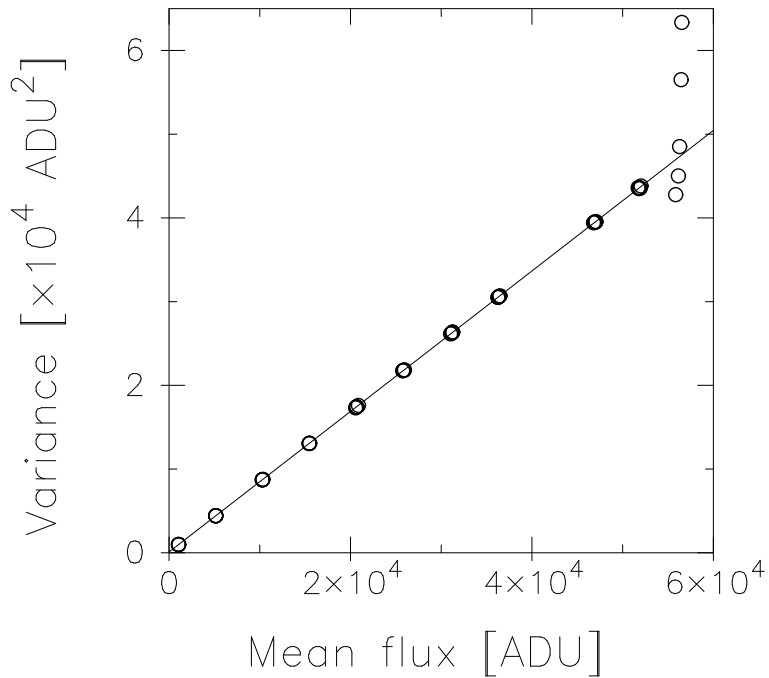


Figure 3.2: Flux variances of uniform images versus these mean fluxes. Each bunch, which contains five circles, represents a group of data for the same exposure time. The large dispersions of the rightmost five points are due to the CCD saturation. A line indicates the best linear fit for all data points except for the saturated data. The fit provides $g = 1.19$ electrons ADU^{-1} and $\sigma_{\text{read}} = 11.5$ electrons pixel^{-1} .

3.3.2 Dark Noise

The dark noise, or the thermal current noise, is another source of noises produced randomly by thermal electrons. Although the noise level increases linearly with the exposure time, that can be reduced by cooling CCD camera. Apogee-cam has a peltier device which can keep the CCD temperature as -40 degrees or below during most of nights (except for very warm nights, which are rare at our site). In order to estimate the level of the dark noise, we examined the dark images, which are exposed images with the camera's shutter closed, as follows.

Dark images are routinely taken on every night (before or after observations) whenever any observation is done, with the same exposure times as the observations, in order to subtract the bias and dark-noise levels from the observation images. Usually more than 4 dark images are obtained for each night and each exposure time, in order to remove cosmic ray events and to increase statistics. Among the dark images taken from June 2008 to November 2009, we selected a set of images with fulfilling three conditions: i) taken on the nights when at least three different exposure-time observations were done (and the corresponding dark images were also taken); ii) taken on the nights when the time difference between the shortest and the longest exposure times of the observations is longer than 89 s; iii) the dark images had been taken with the CCD temperature kept at lower than -40 degrees. As a result, dark images of totally 12 nights were selected. Then for each night, a linear relation between exposure time and mean flux of the dark images was examined. Figure 3.3 shows those relations for the 12 nights' data.

We found that the gradient of the time-flux relation, which corresponds to the dark noise in units of $\text{ADU pixel}^{-1} \text{ s}^{-1}$, vary night-to-night in the range from 0.004 to 0.08, with the median value of 0.028 and the first and third quartiles of 0.015 and 0.052, respectively. The reason of this variation is not clear, but that might be attributed to the instability of the electronics. Nevertheless, we found that the integrated dark noise over 60 s, which

is the typical exposure time of the transit observations, does not exceed $\simeq 6$ electrons pixel $^{-1}$. This level is smaller than that of the readout noise (11.5 electrons pixel $^{-1}$), and so does not provide a large impact on the photometry of stars. Note that the mean flux of a zero-second dark image corresponds to the bias level of an image, and the level seems to vary along with the observational epoch; this can be attributed to the electronics problem (secular drifts due to age or poor stability in the electronics, Howell 2006), and is no impact on the photometry since the bias level is to be subtracted from observation images.

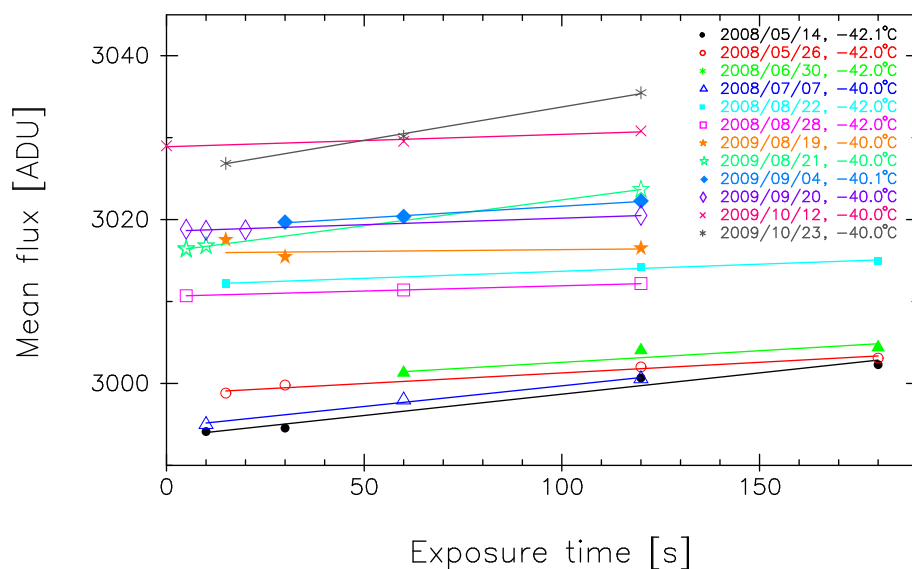


Figure 3.3: Nightly relations between exposure time and mean flux of dark images. 12 nights were selected and examined according to the context. The different color and symbol indicate different night, as shown in the legends at the upper right in the figure. The CCD temperatures at the times the dark images were taken are also shown in the legends.

3.3.3 Flat-field Noise

The other contributor to the instrumental noises is the flat-field noise, which comes from incompleteness of the flat-field correction. The top two images of Figure 3.4 show different flat-field images, each was generated from different sets of 40 uniformly-illuminated images taken in different nights. The bottom one in the same figure shows an image which was generated by taking the ratios of the top image to the middle one (the divisional image). If the artificially-generated uniform source were ideal, the two flat-field images would be same. However, slightly-different patterns are seen between the two images, and more clearly, irregular patterns are seen on the divisional image, indicating that the approximated uniform source is not perfect. Such incompleteness of the flat-field image can affect the photometry of stars, in case that the stellar positions on the CCD and/or the seeing vary significantly over a night, so that the stellar light is collected by different pixels through the night.

The standard deviation of the values over the divisional image is about 0.16 %. This value is larger than the expected value of 0.10 %, which is derived by taking only the random noises account, i.e. calculating square-root of sum of squares of the photon noise, the readout noise, and the dark noise quadratically. This fact indicates that the systematic noise caused by the flat-field incompleteness is about 0.12 %.

A further investigation for the degree of the flat-field noise was done as follows. The uniformly-illuminated images used in section 3.3.1 were divided by a different master flat-field image, which was generated by an another set of 40 uniformly-illuminated images taken on a different night. Then, similarly to section 3.3.1, mean fluxes and variances of these calibrated images were measured. Figure 3.5 shows the two sets of flux-variance relations: the open circles are the same ones as shown in Figure 3.2 with exclusion of the saturated data, while red pluses represent the data derived above. A clear discrepancy is seen between the two data sets, and this discrepancy can be attributed to the flat-field

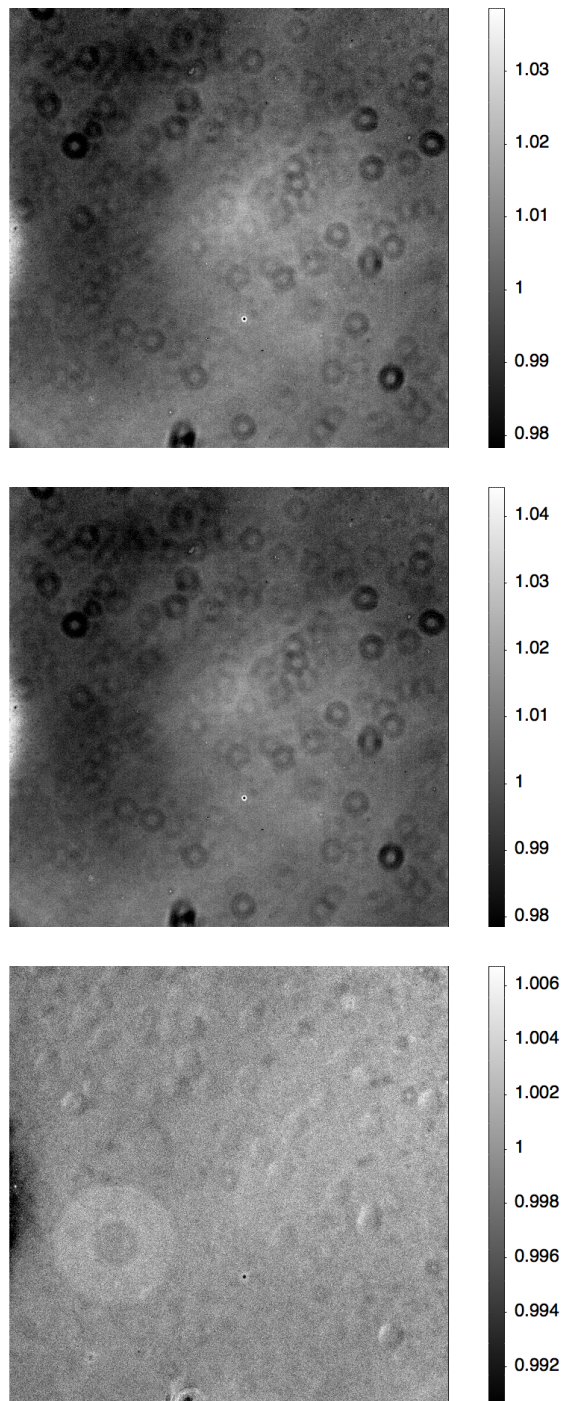


Figure 3.4: (top) A flat-field image generated from a set of 40 uniformly-illuminated images taken in October 10, 2009. (middle) Similar one, but from a different set of 40 images taken in October 14, 2009. (bottom) A divisional image generated so that the former flat-field image was divided by the other.

incompleteness.

Here, we introduce an additional component of variance as the flat-field noise to the equation (3.2), assuming that this noise is produced randomly in each pixel in the form of $f_{\text{flat}}F$, where f_{flat} is a coefficient. Then the equation of variance is expressed as

$$\sigma_F^2 = \frac{F}{g} + \frac{\sigma_{\text{read}}^2}{g^2} + f_{\text{flat}}^2 F^2. \quad (3.3)$$

This is a quadratic function of F . We fitted this function to the latter dataset with fixing the values of g and σ_{read} to 1.19 electrons ADU^{-1} and 11.5 electrons pixel^{-1} , respectively, and then obtained $f_{\text{flat}} = 0.118\%$ (red solid line in Figure 3.5). This value is consistent with the value of 0.20%, which is the standard deviation of the divisional image. Note that in this fitting procedure we included the forty 40-s images, which were excluded for the linear fit for the former dataset in section 3.3.1.

Next, we examine the impact of the flat-field noise on the photometry. We continue the assumption that the flat-field noise behaves as a random noise in the form of $f_{\text{flat}}F$. When the flux of a star, F_{star} , falls onto m_{pix} pixels, the total flat-field noise of the star, $\sigma_{\text{flat,total}}$ is expressed as

$$\sigma_{\text{flat,total}} = \frac{1}{\sqrt{m_{\text{pix}}}} \sum_i^{m_{\text{pix}}} f_{\text{flat}} F_i = \frac{f_{\text{flat}} F_{\text{star}}}{\sqrt{m_{\text{pix}}}}, \quad (3.4)$$

where F_i is the flux at pixel i . When the point spread function (PSF) of a star is a gaussian with the seeing size (full width at half maximum of the PSF) of $2''$, about 99.7% of the stellar flux falls onto $m_{\text{pix}} = 250$ pixels; in this case, substituting $f_{\text{flat}} = 1.2 \times 10^{-3}$, we get $\sigma_{\text{flat,total}} \simeq 7.6 \times 10^{-5} \times F_{\text{star}}$. This value is less important when we discuss about the photometric precision of the order of 10^{-3} , which is the case we consider.

However, in reality, the flat-field noise is a systematic one having a certain ‘pattern’ over the flat-field image, rather than a random one. Therefore, if the stellar positions move around a CCD area where is much uneven, the measured flux could be much affected by

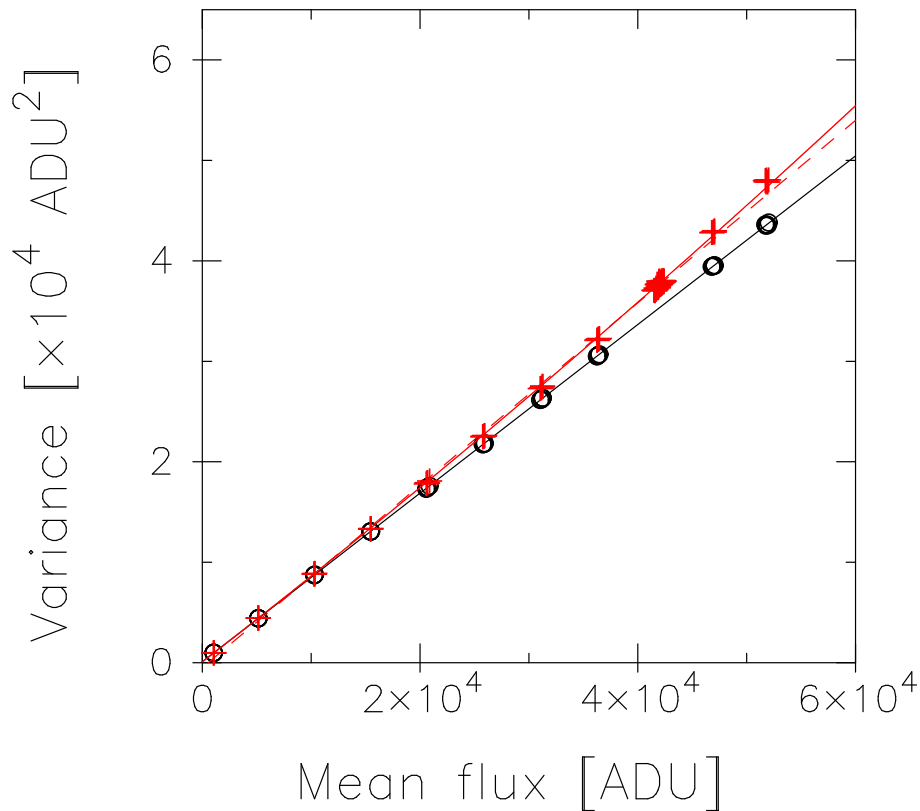


Figure 3.5: Open circles and a linear line along with the circles are the same as in Figure 3.2 but saturated data are excluded, while red pluses represent mean fluxes and variances of a different set of calibrated uniform images generated by using the same raw uniformly-illuminated images as used in Figure 3.2 and a different master flat-field image generated from an another set of 40 uniformly-illuminated images taken in a different night (October 10, 2009). The red dashed line represents the best fit with a linear function for the latter dataset and the red solid line shows the best fit with a quadratic one for the same dataset with fixing the values of gain and readout noise to the ones determined in section 3.3.1.

the flat-field noise. Since the B&C telescope has no realtime auto-guide system and the tracking error becomes up to $1.5 \text{ pixel min}^{-1}$, such effect could be considerable.

3.3.4 The Semi-Realtime Auto Guiding Software

To avoid the systematic flat-field noise, it is necessary to fix a star at a certain position on the CCD during observations over a night. An auto-guiding system, which requires an

additional guiding telescope equipped with a CCD camera, can always keep the stars at the same positions even under observation, leading to reduce the flat-field noise. Because the B&C telescope has no such system, we had corrected the tracking error by hand occasionally when the accumulated stellar drift on the CCD becomes large.

To improve this situation, we developed a software which keeps on correcting tracking errors in semi-realtime, i.e. a correction is done during the interval time of two successive observations. This semi-realtime auto guiding (SRAG) software measures the positional changes of astronomical objects between on a reference image and on the previously observed image, and feeds back the information to the telescope to correct the tracking error. When continuous observations are being carried out, the calculation is performed during the current observation, and the feed back will be done during the interval time between the current exposure and the next one. Therefore the tracking corrections are performed once every two exposures. SRAG was installed it into the B&C system in August 2009.

Figure 3.6 shows the effectiveness of the SRAG software. The upper panel shows the behaviors of a star, WASP-5, on the CCD plane during the observations on 18 Jun 2008, when SRAG was off. The exposure time was set to 60 s and the total number of exposure was 342. The standard deviation of the object's position, from the mean position of $(x, y) = (907.1, 176.2)$, was 25.7 pixels. On the other hand, the lower panel shows the behaviors of the same star but on 4 September 2009, when the observations had been done with SRAG on. The total exposures of 167 were taken with the same exposure time. The standard deviation was reduced to 3.9 pixels with the mean position of $(x, y) = (882.0, 135.3)$. This size is well within the typical seeing size of $2''$, or 6 pixels.

Nevertheless, any apparent improvement on the photometric precisions have not been achieved with SRAG, possibly because the local unevenness around the measured stars was not significant.

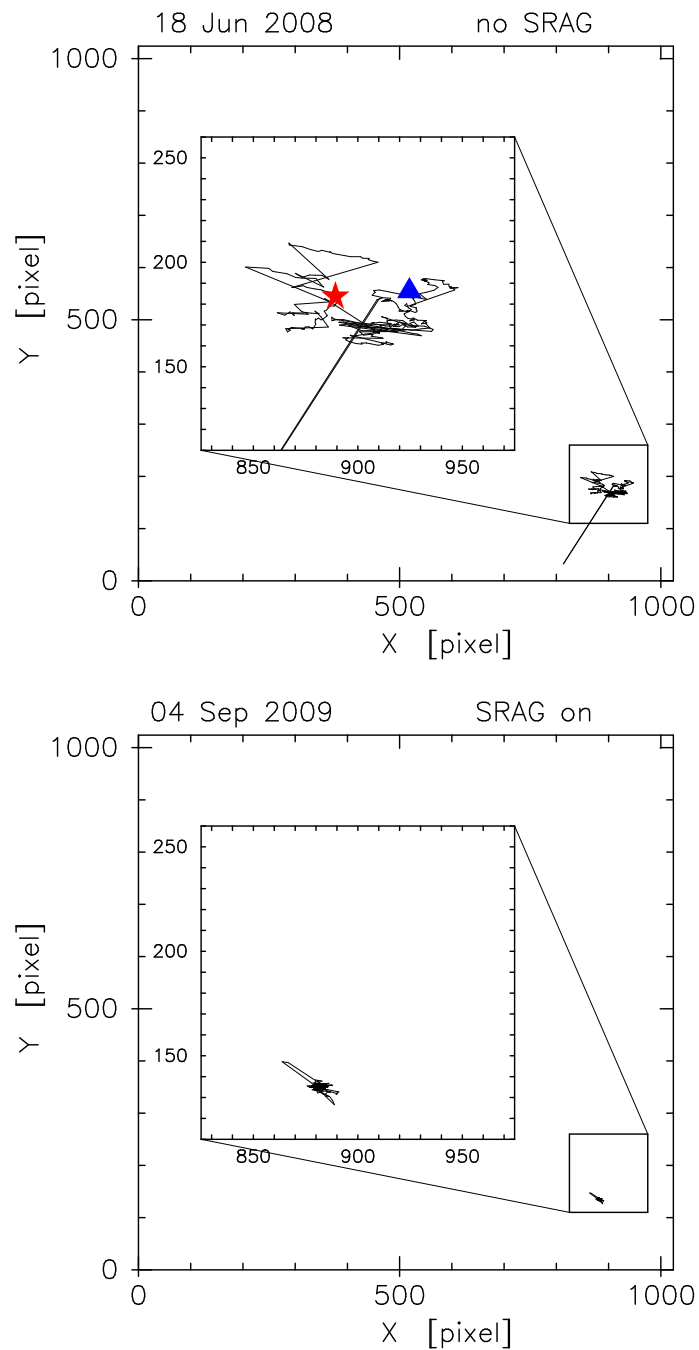


Figure 3.6: Behaviors of WASP-5 on the CCD plane during transit observations on 18 June 2008, when the SRAG software had been off (top), and on 4 September 2009 with SRAG on (bottom). The 12-mag target star had been placed on the lower right of the CCD during the observations, and these trajectories are drawn with lines. The magnified views are inset in both figures, while the start and the end positions of the target star are marked as red star and blue triangle, respectively, for only the top figure.

Chapter 4

Observations and Data Reduction

4.1 Target Selection

For TTV observations, it is critical to measure mid-transit times precisely. The main factors determining a mid-transit time precision are brightness of the host star, transit depth, and transit ingress/egress duration. Considered a series of continuous photometric observations of a planetary transit with a photometric precision of σ_{ph} and a sampling rate of Γ , the transit timing precision, σ_{Tc} , is approximated as

$$\sigma_{\text{Tc}} \simeq (t_e/2\Gamma)^{1/2} \sigma_{\text{ph}} (R_p/R_*)^{-2}, \quad (4.1)$$

where t_e is the ingress/egress duration (Ford & Gaudi 2006). Therefore favorable transiting system as a TTV target is such that the host star is brighter and the planet-star radius ratio is larger, as well as the ingress/egress duration is longer. As of the beginning of our TTV campaign (June 2008), there were only several transit systems which can be seen from the observatory and are bright enough ($V < 13$ mag), such as WASP-4, WASP-5, and WASP-18. Planets in those systems are all hot Jupiters orbiting sun-like stars and so produce transit depths of $\sim 1\%$ or more. Then we have started TTV observations for those

systems. In this paper, we focus on the analysis for WASP-5b, which have been claimed to show dispersions of the transit timings against a constant period (Gillon et al. 2009)

4.2 The WASP-5 System

The transiting planet WASP-5b was discovered by Anderson et al. (2008, hereafter A08) as a $1.58 M_{\text{jup}}$ hot Jupiter orbiting a $V = 12.3$ (G4V) star with a period of 1.63 d. Table 4.2 summarizes the information of the WASP-5 system.

Gillon et al. (2009, hereafter G09) conducted photometric and spectroscopic follow-up observations of high precision for this system using the 8.2-m Very Large Telescope (VLT). Although their photometric data were not analyzed accurately due to uncorrectable systematic errors, and were not used for their analysis, they checked and reanalyzed the photometric and RV data presented in A08, and found the planetary orbit to be marginal nonzero eccentricity ($\sim 2\sigma$). They also found that the reduced χ^2 of a linear fit for four transit timing data was 5.7, which might be a sign of additional bodies. Southworth et al. (2009, hereafter S09) presented two high-quality photometric transit light curves obtained with the 1.54-m Danish telescope and with residual standard deviations relative to theoretical fits of 0.50 and 0.59 mmag. They argued that the inconsistency between the transit data and a linear ephemeris could be associated with a relatively poor transit light curve from the Faulkes Telescope South (FTS). Triaud et al. (2010, hereafter T10) presented 33 new RV data obtained with the HARPS spectrograph, including data during a transit, and 5 CORALIE data in addition to the eleven given by A08. They derived a sky-projected spin-orbit angle of $\lambda = 12^{\circ}.1_{-10^{\circ}.0}^{+8^{\circ}.0}$, which is consistent with a spin-orbit alignment that is naturally expected from the type-II migration model for the migration mechanism of WASP-5b. However, the planet-planet interaction model followed by the stellar obliquity dumping could still be an alternative scenario, because the host star is a “cool star” in the context of Winn et al. (2010) (see section 1.4.3), which might easily dump

Table 4.1: Information of the WASP-5 system.

The star WASP-5	
R.A. (J2000)	23:57:23.74
Dec. (J2000)	-41°16'37".5
Distance [pc]	300 ± 50
Spectral type	G4V
Mass [M _⊙]	0.99 ± 0.08
Radius [R _⊙]	0.97 ± 0.06
The planet WASP-5b	
Mass [M _{Jup}]	1.58 ^{+0.13} _{-0.08}
Radius [R _{Jup}]	1.090 ^{+0.094} _{-0.058}
Orbital period [d]	1.6284296 ^{+0.0000048} _{-0.0000037}
Semi-major axis [AU]	0.02683 ^{+0.00088} _{-0.00075}
Eccentricity	0 (adopted)
Inclination [degree]	> 85.0
λ [degree] ^b	12.1 ^{+8.0} _{-12.0}

Note: The values are extracted from Anderson et al. (2008), except for λ.

^b Sky-projected spin-orbit angle of the system, derived by Triaud et al. (2010).

the stellar obliquity. We cannot exclude this scenario at this point in time, and therefore searching for additional planets near MMRs with WASP-5b by means of the TTV method is useful for testing these migration scenarios for this planet.

4.3 Observations

We have successfully observed 7 transits of WASP-5b by using the B&C telescope from June 2008 though June 2010. The observations were done on the nights when the transits were predicted and the sky was clear as well as there was no important microlensing event to be followed up. Exposure time was set to either 30 or 60 s, and the Bessel *I*-band filter was used for all the observations. The focus was optimized properly for all observations except for some nights when the telescope was defocused so that the full width at half maximum of the stellar PSF was 3''-4''. An observation log is shown in table 4.2.

Table 4.2: Observing log.

Date	Epoch ^a	Exp. [s] ^b	Filter	# of data ^c	Focus/defocus ^d	Airmass ^e
2008 Jun. 18	160	60	<i>I</i>	248	focus	1.55 → 1.00
2008 Nov. 2	244	30	<i>I</i>	393	focus	1.00 → 1.35
2009 Sep. 4	432	60	<i>I</i>	168	focus	1.03 → 1.00 → 1.07
2009 Oct. 5	451	60	<i>I</i>	313	focus	1.07 → 1.00 → 1.39
2009 Oct. 18	459	60	<i>I</i>	248	defocus	1.01 → 1.80
2010 Jun. 16	607	30	<i>I</i>	307	focus	2.60 → 1.23
2010 Jun. 29	615	60	<i>I</i>	202	focus	1.78 → 1.04

^a Transit epoch relative to a reference transit at BJD = 2454375.62510.

^b Exposure time.

^c The number of data, after discarding some apparent outliers.

^d Focus condition of the telescope, either focusing or defocusing.

^e Airmass change from the observation start through the end times.

4.4 Data Reduction

All images were initially bias subtracted and flat-field corrected in the standard manner. Figure 4.1 shows a sample of the calibrated images. We then performed an optimized aperture photometry, called ‘scaled aperture photometry’, for the target star WASP-5 and some (2-4) comparison stars in the same field of view as follows. Note that each star to be measured is isolated enough from the closest star so as not to be contaminated.

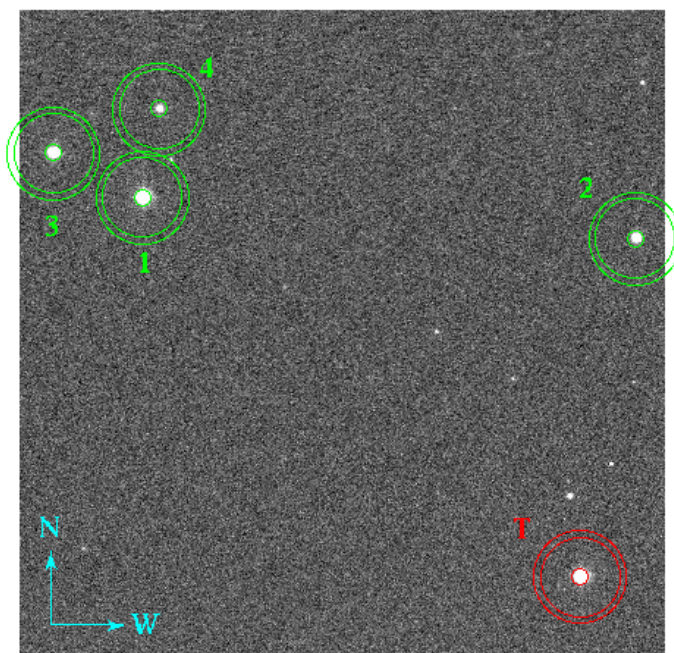


Figure 4.1: A sample of the calibrated (flat-corrected and bias-subtracted) images of the field for WASP-5. The lower right star denoted by T is WASP-5, and the other stars denoted by 1 through 4 are comparison stars to be used in the photometry. Each of the innermost circle represents the aperture within which the stellar flux is counted, while the outer two circles represent the inner and outer radii of the annulus where the sky background flux is calculated. Upper and right directions of the image are north and west, respectively.

First, for each image j , we searched for an initial photometric aperture radius, $r_{\text{opt},j}$, that maximized the signal-to-noise ratio of the target flux, using a step size of 0.1 pixels.

The target flux, F_{star} , is calculated so as to be equal to the total flux in the aperture $r_{\text{opt},j}$ minus the corresponding sky flux, $F_{\text{sky}} = m_{\text{pix}} f_{\text{sky}}$. Here, m_{pix} is the total number of pixels in the aperture and f_{sky} is the median flux per pixel within an annulus where the inside and outside radii are $r_{\text{opt},j} + 50$ and $r_{\text{opt},j} + 60$ pixels, respectively.

The total noise contribution to the signal is modeled as

$$N = \sqrt{N_{\text{star}}^2 + N_{\text{sky}}^2 + N_{\text{read}}^2 + N_{\text{dark}}^2 + N_{\text{scin}}^2}, \quad (4.2)$$

where $N_{\text{star}} = \sqrt{F_{\text{star}}/g}$ is the poisson noise of the target star's flux, $N_{\text{sky}} = \sqrt{F_{\text{sky}}/g}$ is the sky background noise, $N_{\text{read}} = \sqrt{m_{\text{pix}}\sigma_{\text{read}}/g}$ is the readout noise, $N_{\text{dark}} = \sqrt{m_{\text{pix}}\sigma_{\text{dark}}\Delta t}$ is the dark current noise, and N_{scin} is the atmospheric scintillation noise. Here, Δt is the exposure time in seconds; g , σ_{read} , and σ_{dark} are defined and determined in Section 3.3. The scintillation noise can be expressed as

$$N_{\text{scin}} = \sigma_0 \frac{z^{7/4}}{D^{2/3}(\Delta t)^{1/2}} \exp\left(-\frac{h}{8000\text{m}}\right) F_{\text{star}}, \quad (4.3)$$

where z is the airmass, D is the telescope diameter in cm, and $h = 1029$ m is the observatory altitude (Dravins et al. 1998; Young 1967). σ_0 is a coefficient that is often taken to be 0.064, and we also adopted this value. Under normal conditions with an exposure time of 60 s, the main contributor to the total noise was the photon noise ($\sim 0.12\%$ of the target flux); the contributions from the other noises were one or two orders of magnitudes less than that.

Next, after determining the $r_{\text{opt},j}$ value for the target star, this radius was applied to the other comparison stars on the same image to measure their fluxes. The target flux was then normalized to a reference flux that was created as the weighted average of the fluxes of the comparison stars. The derived light curve of each transit was then normalized by the median flux of the light curve. The photometric error of a normalized flux was initially

estimated by using equation (4.3) and the error propagation equation.

Finally, for each transit E , we searched for a scaling factor γ_E (in the range of 0.7 to 1.50), to the initial radius $r_{\text{opt},j}$ in order to minimize the rms scatter of the derived out-of-transit (OOT) light curve (either before or after transit). Figure 4.2 shows schematics of the scaled aperture photometry performed here. The derived light curves of the 7 transits are displayed in Figure 4.3. All light curves show apparent planetary transits, while apparent trends on the baselines, which are expected to be constant, are also seen. Corrections of these trends will be described in the next section.

In order to assess the validity of the scaled aperture photometry, we also performed standard aperture photometry with a fixed radius $r_{\text{fix},E}$ for each transit, which was selected so as to produce the minimum rms scatter for the OOT light curve. The result of this exercise was that the OOT rms values derived from the scaled aperture photometry were slightly better than those from the standard one, for all transit light curves except for the transit $E=615$, for which there are a relatively small number of OOT data points, possibly leading to a large statistical fluctuation. Table 4.3 shows a comparison of OOT rms values derived by the two methods. In order to maintain consistency, all light curves were generated by using the scaled aperture photometry, and these were used for further analyses.

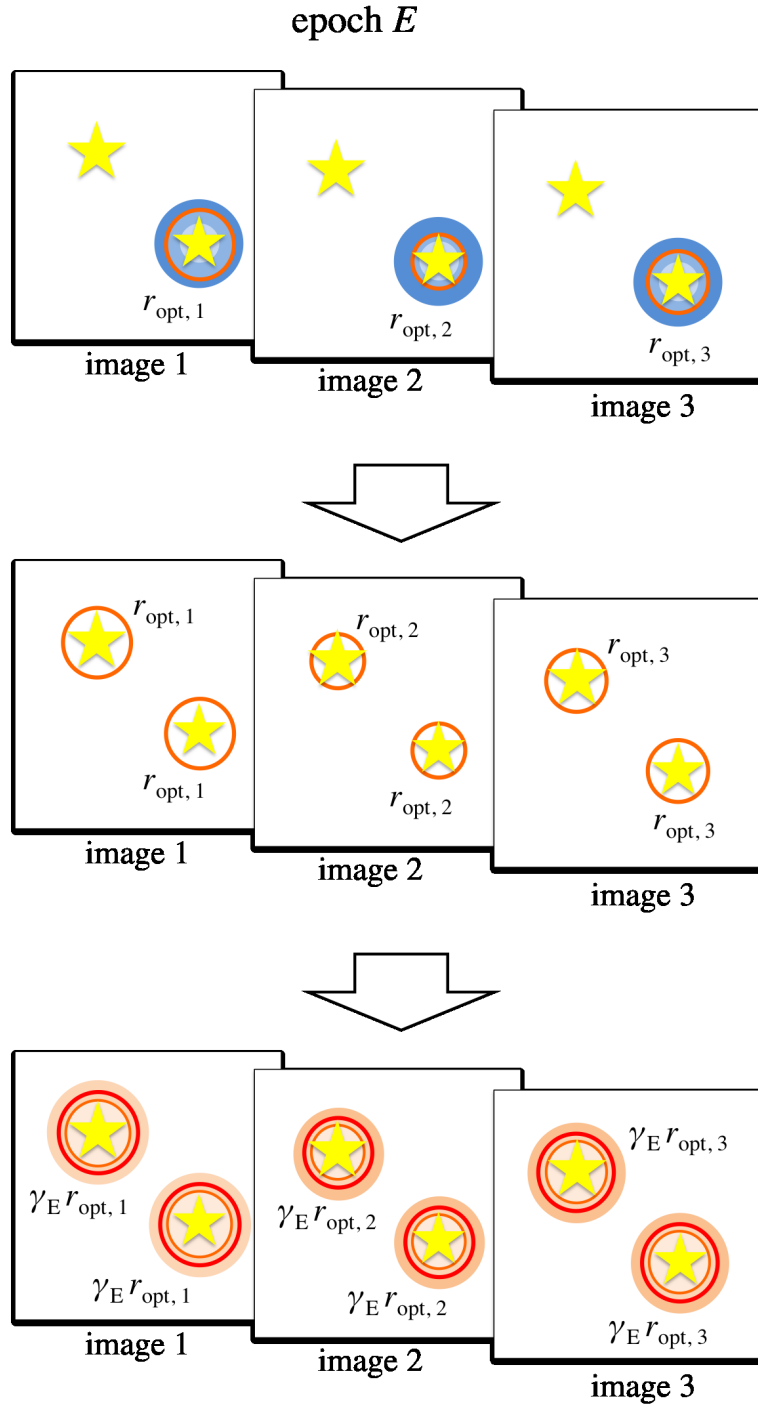


Figure 4.2: Schematics of the scaled aperture photometry. (Top) For each image j of a transit epoch E , an initial aperture radius $r_{\text{opt},j}$ is selected so that the signal-to-noise ratio of the flux of the target star (lower right one on each image) is maximized. (Middle) The selected radii are applied to the other comparison stars to measure these fluxes and derive a target's relative light curve. (Bottom) An optimum scaling factor γ_E , which multiplies every $r_{\text{opt},j}$, is searched so that the scatter of the out-of-transit light curve is minimized.

Table 4.3: Comparisons of rms scatters. *

Epoch	N_{OOT}	γ_E	$\gamma_E r_{\text{opt},j}$	$r_{\text{fix},E}$	rms scatter for OOT (%)	
			[pixels]	[pixels]	$\gamma_E r_{\text{opt},j}$	$r_{\text{fix},E}$
160	75 (a)	0.96	9.6 - 13.1	13.1	0.177	0.178
244	119 (a)	1.27	13.1 - 18.5	15.8	0.488	0.492
432	50 (b)	1.34	11.5 - 14.5	14.1	0.205	0.205
451	77 (a)	1.47	14.4 - 16.0	14.0	0.282	0.284
459	52 (b)	1.24	13.9 - 17.1	13.9	0.179	0.181
607	49 (a)	1.42	12.5 - 14.3	13.0	0.287	0.288
615	44 (a)	1.30	11.1 - 13.7	12.7	0.161	0.158

* Comparisons of rms scatters between OOT light curves derived using optimized radii ($\gamma_E r_{\text{opt},j}$) and that derived using fixed radii ($r_{\text{fix},E}$). N_{OOT} is the number of OOT (either before or after the transit) data points and ‘b’ and ‘a’ in parentheses stands for ‘before’ and ‘after’ the transit, respectively.

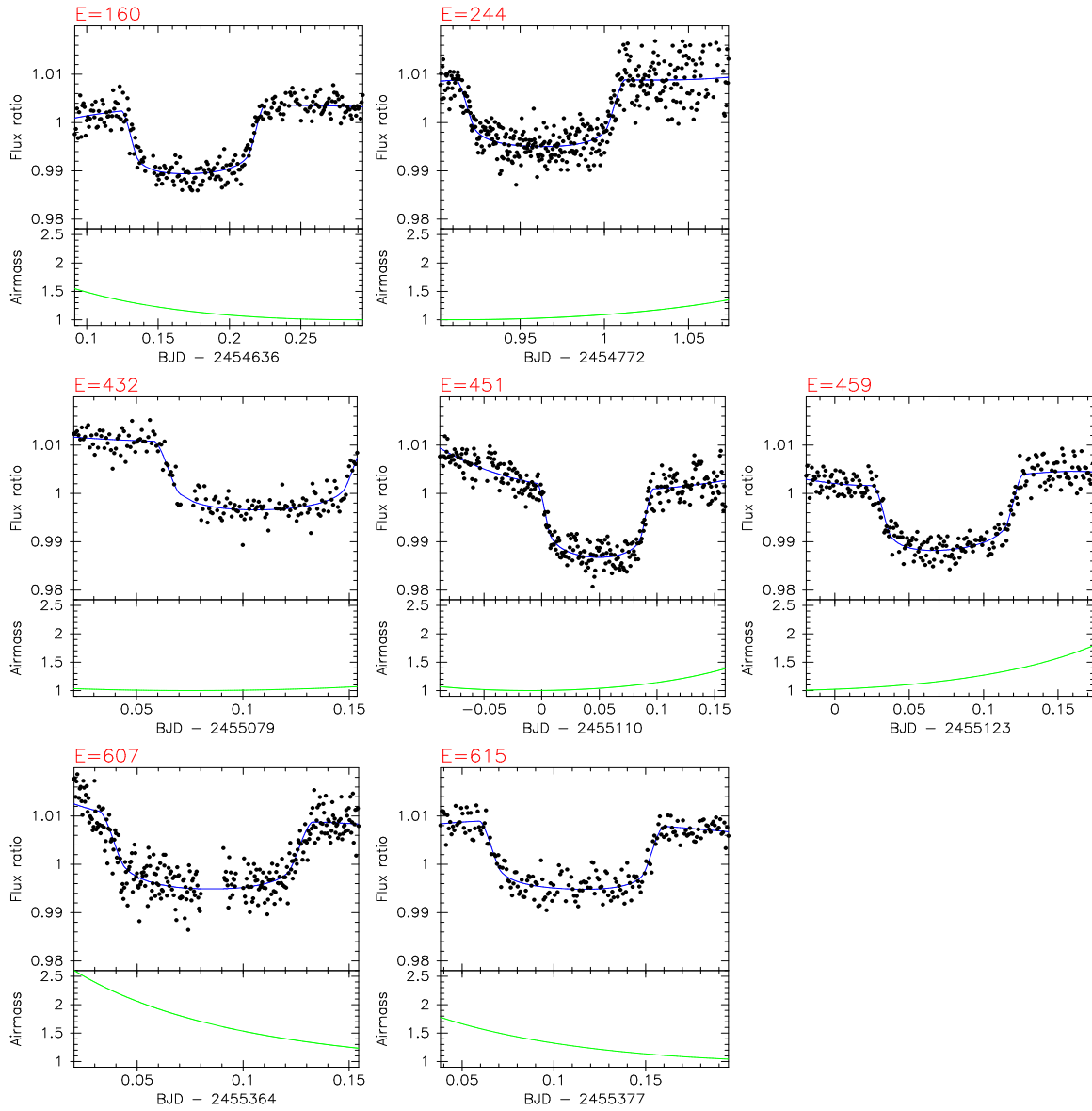


Figure 4.3: Baseline-uncorrected light curves of WASP-5b (upper panels) and the time variations of airmass on the respective nights (lower panels). X-axes are TDB-based BJD minus integers of BJDs at the respective mid-transit times. The blue lines show the best-fit baseline models with fixing the transit parameters to those determined by S09. The E number on top left of each figure stands for the corresponding transit epoch.

Chapter 5

Light Curve Analysis

In this section, we will describe analysis of the obtained light curves. we will present procedures of systematic-error correction and error normalization in these light curves in section 5.1, and estimation of time-correlated systematic noise in section 5.2. Light curve fitting and its results will be shown in section 5.3.

5.1 Baseline Systematic Correction

Since apparent systematic trends are seen in the derived light curves, corrections of the systematic trends are necessary. The systematic trends can arise from the changing airmass, variations in the atmospheric extinction coefficient, slow variability in the brightness of the target or comparison stars, and so forth. The time variations of airmass during the transit observations are shown in the bottom panels of Figure 4.3.

By using the correction factor, Δm_{corr} , in the magnitude scale, the corrected flux, F_{corr} , can be expressed as

$$F_{\text{corr}} = F_{\text{obs}} \times 10^{-0.4\Delta m_{\text{corr}}}, \quad (5.1)$$

where F_{obs} is the observed flux of the target normalized by the reference flux. If we assume that amplitudes of the intrinsic stellar variability and variations in the second-order atmospheric extinction coefficient both are proportional to time, Δm_{corr} can be expressed as

$$\Delta m_{\text{corr}} = k_0 + k_z z + k_t t + k_{zt} zt \quad (5.2)$$

where z is the airmass, t is the time, and (k_0, k_z, k_t, k_{zt}) are the relevant coefficients (see Appendix). This equation is similar to equation (1) of Winn et al. (2009), although we here use four coefficients instead of three. Provided there were enough data points, only the OOT light curve segments were fitted to estimate the systematic-correcting function. However, three of the light curves ($E=244$, 432, and 607) did not have an adequate amount of data points in their OOT sections, and also apparent systematic variations were seen in the first half part of the light curve of $E=451$ transit, which could not be corrected if only the OOT data were used. Therefore, we decided to fit each light curve including the transit section while fixing the parameters defining the transit shape to the values derived by S09, who obtained two transit light curves with higher precision than ours.

To create the parameterized transit light curve, an analytic model of Mandel & Agol (2002) (see Appendix B.1) was used. This model requires 6 parameters: the planet/star radius ratio, R_p/R_* , the semi-major axis of the planetary orbit in units of the star radius, a/R_* , the orbital inclination to the line of sight, i , the orbital period, P , and two stellar limb-darkening coefficients, u_1 and u_2 . We used a quadratic limb darkening law,

$$I(\mu) = 1 - u_1(1 - \mu) - u_2(1 - \mu)^2, \quad (5.3)$$

where I is the intensity and μ is the cosine of the angle between the line of sight and the line from the center of the star to a position of the stellar surface. For correcting systematic

errors, these parameters were fixed to the values of $R_p/R_* = 0.1110$, $a/R_* = 5.4142$, $i = 85^\circ.8$, $P = 1.6284246$ d (adopted from S09), $u_1=0.257$, and $u_2=0.341$ (adopted from the tables of Claret 2000). By using this model and the equation (5.1) and (5.2), each light curve was fitted by the χ^2 minimization method with five free parameters: k_0, k_z, k_t, k_{zt} , and the mid-transit time T_c . The derived coefficients and their 1σ uncertainties are listed in Table 5.1, and the best-fit light curve models are overplotted with blue lines in Figure 4.3. Figure 5.2 shows the baseline-corrected light curves. The electric tables of these light curves are found in the Online Materials of Fukui et al. (2011) ¹.

Table 5.1: The derived baseline-correction coefficients and their 1σ uncertainties*.

Epoch	k_0	k_z	k_t	k_{zt}	T_c
160	0.016 ± 0.004	-0.0099 ± 0.0035	-0.03 ± 0.06	0.02 ± 0.08	0.17464 ± 0.00038
244	0.16 ± 0.14	-0.17 ± 0.16	-0.13 ± 0.13	0.15 ± 0.14	0.96209 ± 0.00042
432	-0.01 ± 0.03	0.03 ± 0.03	0.1 ± 0.3	-0.1 ± 0.3	0.10852 ± 0.00048
451	-0.039 ± 0.005	0.041 ± 0.005	0.053 ± 0.035	-0.11 ± 0.03	0.04646 ± 0.00036
459	-0.083 ± 0.027	0.083 ± 0.026	0.19 ± 0.07	-0.30 ± 0.10	0.07624 ± 0.00040
607	0.11 ± 0.11	-0.029 ± 0.035	0.14 ± 0.11	-0.46 ± 0.46	0.08263 ± 0.00063
615	0.02 ± 0.04	-0.01 ± 0.02	-0.1 ± 0.2	0.0 ± 0.3	0.10968 ± 0.00052

* Fittings were done for the light curves of which the integers of BJDs of the respective mid-transit times had been subtracted from the original BJDs.

To test the validity of this correction, we alternatively made corrections of the $E=160$ complete transit light curve by fitting only its OOT parts, and then compared the two corrected light curves. Figure 5.1 shows the two light curves (open and filled circles) and their differences. The difference was not larger than 0.00048, which is well within the typical error bar estimated by equation (4.3) (~ 0.002). Since we obtained highly similar results for two other complete transits ($E=459$ and 615), we decided to use the light curves corrected by the former method for further analyses.

¹<http://pasj.asj.or.jp/v63/n1/630123/OM/idx.html>

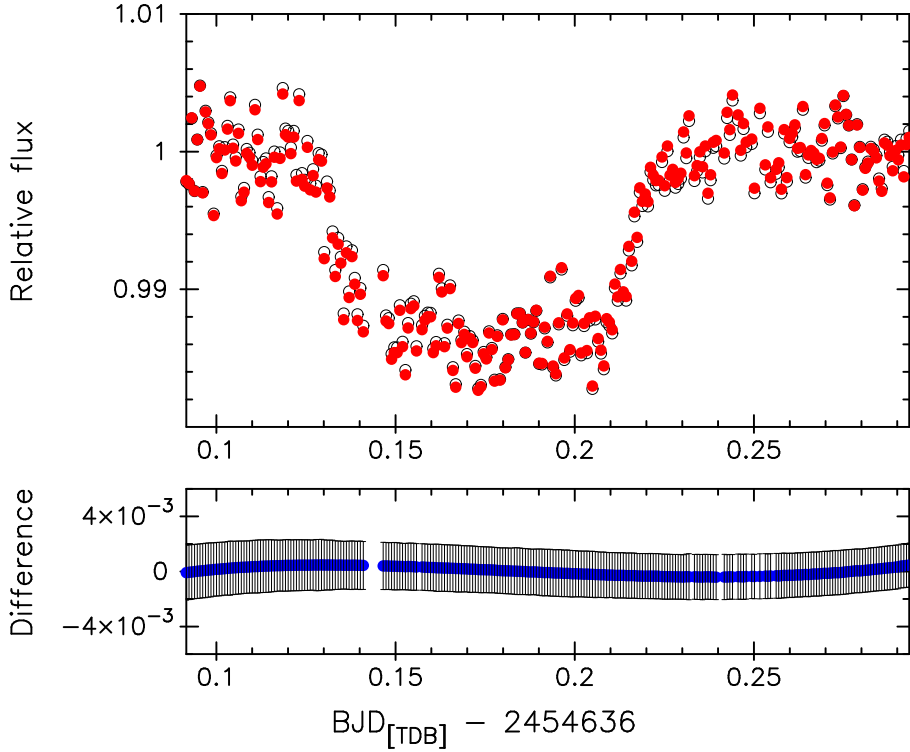


Figure 5.1: Difference (lower panel) between the light curve corrected using coefficients derived by fitting only the OOT part (open circles in upper panel) and the one corrected using coefficients derived by fitting the overall light curve with the transit-model parameters fixed at the values presented in S09 (filled circles in upper panel). The initial error bars estimated from the equation (1) are overplotted on the differential data.

The right most column of Table 5.1 shows the best fit T_c values and their uncertainties, which are what we wanted to derive. However, because the T_c values depend on the transit parameters which can be improved compared with the adopted parameters by fitting all available data including ours, we used the T_c values derived here only for correcting the light curve baselines, and the final T_c values and their uncertainties were determined by the procedure described in the following sections. In addition, we suppose that these baseline corrections do not affect the T_c values so much. The T_c uncertainties derived here are too conservative, because many of the baseline coefficients (k_0, k_z, k_t, k_{zt}) are consistent with zero, which indicate that the number of coefficients may be redundant, while the four coefficients are required for correcting the light curve of $E = 451$. We used the corrected

light curves for further analyses, assuming the baseline corrections were perfect. The impact of the baseline corrections on the T_c values will be discussed in Section 8.2.

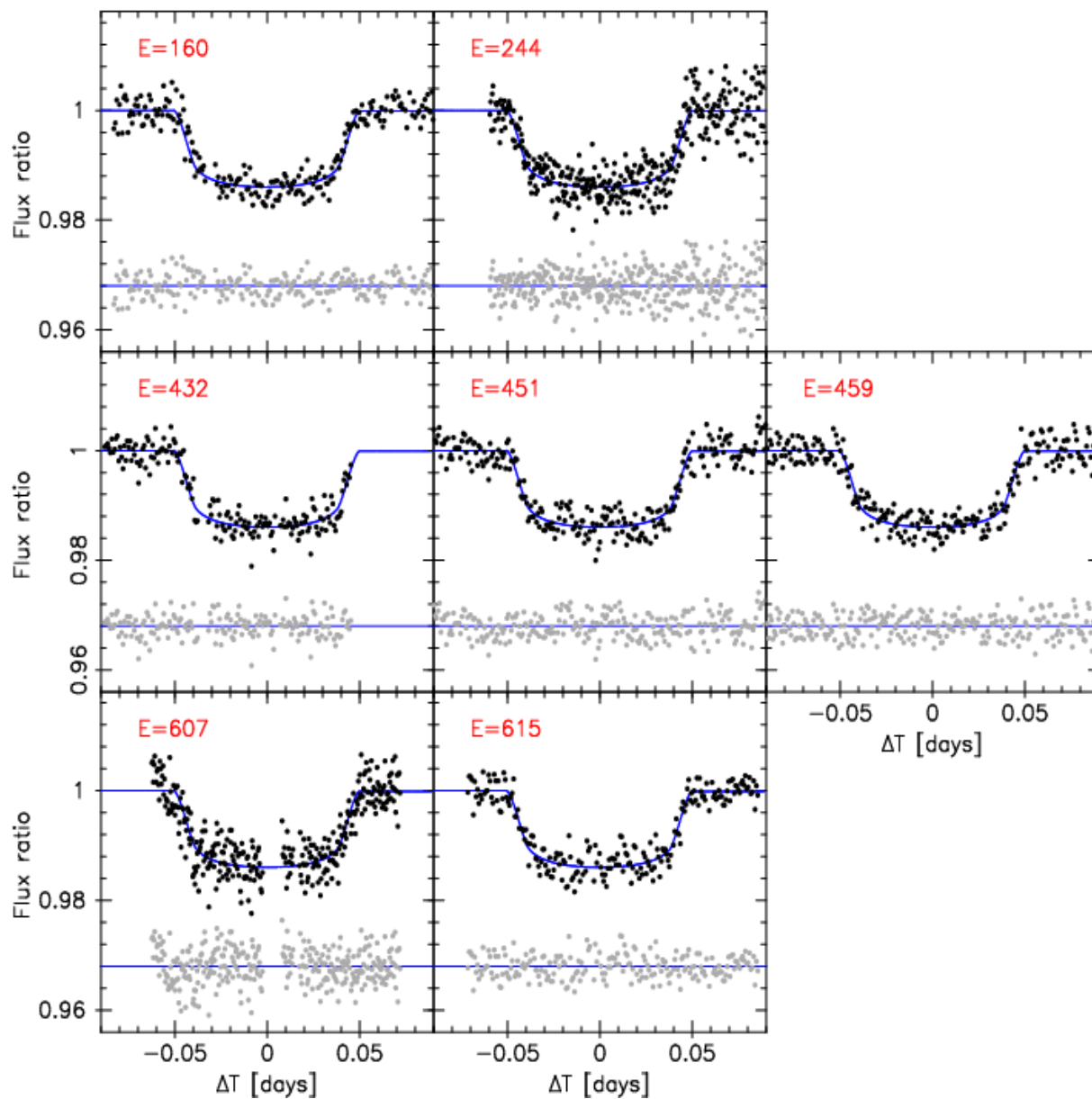


Figure 5.2: Baseline-corrected light curves of WASP-5b (black points) and their residuals (gray points) from the best fit model (blue lines), which was determined by the simultaneous fit for the seven transit light curves with their normalized error bars taking the red noises into account. 0.968 is added to each residual light curve for display. E numbers stand for the corresponding transit epochs.

5.2 Estimation of Time-Correlated Systematic Noise

In order to estimate a statistical weight for each light curve, we fitted the light curve separately and rescaled the initial error bars so that each reduced- χ^2 became unity. we also estimated the time-correlated systematic noise (red noise) by the "time-averaged" method used in e.g. Winn et al. (2008). By this method, an error scaling factor β (> 1) is calculated for each light curve by analyzing a difference between the best-fit model and the light curve. If the red noise is not significant, the expected standard deviation after binning the residuals into M bins of N points, $\sigma_{N,\text{exp}}$, would be

$$\sigma_{N,\text{exp}} = \frac{\sigma_1}{\sqrt{N}} \sqrt{\frac{M}{M-1}}, \quad (5.4)$$

where σ_1 is the standard deviation of the unbinned residuals. On the other hand, the observed value of the standard deviation of the binned data, $\sigma_{N,\text{obs}}$, is measured by

$$\sigma_{N,\text{obs}} = \frac{1}{M} \sum_i^M y_i^2 - \left(\frac{1}{M} \sum_i^M y_i \right)^2, \quad (5.5)$$

where

$$y_i = \frac{\sum_j^N y_{i,j} / \sigma_{i,j}^2}{\sum_j^N (1/\sigma_{i,j}^2)}, \quad (5.6)$$

is the value of the i -th binned data; where $y_{i,j}$ is the value of the j -th unbinned data of the i -th bin and $\sigma_{i,j}$ is the initially estimated uncertainty of $y_{i,j}$. $\sigma_{N,\text{obs}}$ is usually larger than $\sigma_{N,\text{exp}}$ by a factor β due to the existence of red noise. We therefore multiplied every uncertainties of the unbinned data by β , in order to take the red noise into account approximately. Since the value of β depends on the choice of N and M , we adopted the maximum β value in the range from $N = 5$ to 30. The derived values of β and entire rms scatters of residuals are shown in Table 5.2.

Table 5.2: Derived values*.

Epoch	β	N_{\max}	σ_1 [%]	Numbers of data	telescope
160	1.15	15	0.197	248	B&C
244	1.16	14	0.364	386	B&C
432	1.09	6	0.205	168	B&C
451	1.76	18	0.234	313	B&C
459	1.01	8	0.220	247	B&C
607	1.31	17	0.322	306	B&C
615	1.19	13	0.210	202	B&C
5	1.16	10	0.094	138	Euler
7	2.28	27	0.262	335	FTS
204	1.28	15	0.046	73	Danish
218	1.34	15	0.054	101	Danish

* Estimated red-noise factor β , the number of data points in one bin (N_{\max}), unbinned rms scatter from the best-fit model (σ_1), and the total number of data points, for each transit light curve are listed.

5.3 Light Curve Fitting

To assess the quality of our light curves against that of the previous works, we fitted the seven transit light curves from the B&C telescope simultaneously and compared the resultant parameters with those of S09 and T10, in which independent data sets were used. At this time we used the same parameterization as in the previous section, and used formulae of Ohta et al. (2009) for creating a transit light curve model (see Appendix B.2). We used common parameters of i , R_p/R_* , a/R_* , u_1 , and u_2 to all transit light curves, while we used respective mid-transit times, $T_{c,E}$. This fitting allowed the parameters of i , R_p/R_* , a/R_* , u_1 , and each $T_{c,E}$ to vary, while forced u_2 to the theoretical value of 0.321. We fixed u_2 in the fitting process, since the u_1 and u_2 quantities are so strongly correlated that they both could not be well determined from the light-curve fitting. The eccentricity was also fixed to zero, which also could not be constrained from the light curves.

We then derived the best fit parameters by minimizing the χ^2 statistics using the AMOEBA algorithm (Press et al. 1992) and estimated uncertainties using the $\Delta\chi^2 = 1.0$ criterion, following Narita et al. (2007). The resultant parameters and their 1σ uncertainties are shown in Table 6.2. The parameters derived from the B&C are consistent with those of S09 and T10 within their error bars, except for the period P , which may be a sign of the TTVs (discussed in section 6.3).

Figure 5.3 compares phase folded, 120-s binned light curves from the B&C and the Danish (obtained from the online data of S09) telescopes. Before folding the Danish data, the quoted errors were normalized and rescaled by using the same procedures as were done for the B&C data, described in section 5.2; i.e. the quoted errors were normalized so that the reduced χ^2 for the best-fit to each transit was unity and rescaled by a factor β taking the red noise into account. The derived β values are presented in Table 5.2.

The rms values of the residuals for the folded datasets of Danish and B&C from respective best-fit models are 0.00046 and 0.00081, respectively. The rms value of B&C is

about twice larger than that of Danish, however, the uncertainties in the transit-model parameters from the B&C data are comparable to those from the Danish data presented in S09 (see Table 6.2). This result initially appears surprising; however, we found that the values of the error-rescaling factor β for the Danish data are larger than most of those for the B&C data (see Table 5.2). As a consequence, the average values of the binned errors of the Danish and B&C data sets are 0.00061 and 0.00084, respectively, which are more comparable. Moreover, the R -band filter used for the Danish observations would have resulted in a larger limb-darkening effect than that seen using the I -band filter employed in the B&C observations. This leads to a relatively poorer determination of the model parameters for the Danish data (e.g., Pál 2008). In addition, S09 included limb-darkening model dependencies in their error estimation, which enlarged the errors of the transit-model parameters. However, all general limb-darkening models produce symmetrical transit shapes, which have little effects on the errors of transit timings. For this reason, we do not include model dependencies derived from limb-darkening in this paper.

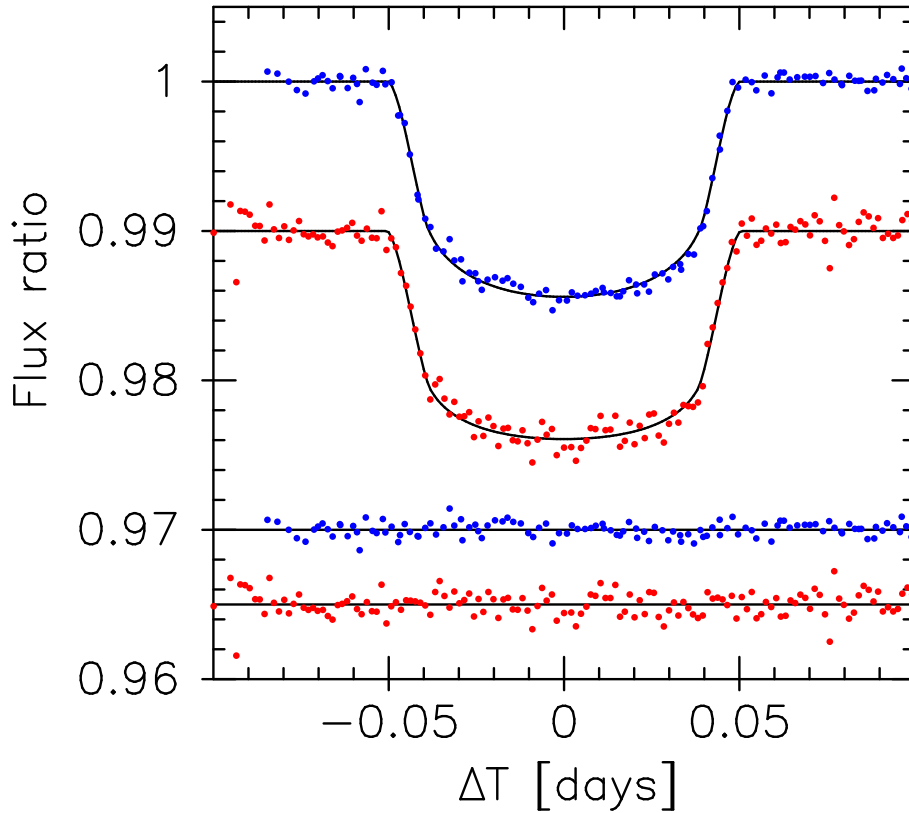


Figure 5.3: Phase folded, 120-s binned light curves of WASP-5b from the Danish telescope (top, blue points) (S09) and the B&C telescope (second, red points) are shown. Black solid lines show the best-fit models for the Danish data (for the case using the quadratic limb-darkening law presented in S09) and for the B&C data (derived from the joint-fit analysis to the seven light curves). Third and bottom plots show their residuals (0.965 and 0.970 are added to respective datasets for display). The rms scatters of respective residuals are 0.00046 and 0.00081, respectively.

Chapter 6

Combined Analysis with Published Data

In order to revise the physical parameters of the transiting planets and derive the transit timings of all collected light curves in a homogeneous manner, we assemble all available photometric and RV data in addition to our own data, and fit them jointly. The data sets used here are described in section 6.1 and the model fitting and derived parameters are explained in section 6.2. We present the measurement of transit timing variations in section 6.3.

6.1 Data Sets

The whole set of the WASP-5b data consists of 11 photometric and two RV data sets. Of the photometric data sets, one is from the 1.2 m Euler telescope (with 133 data points) and one is from the 2.0 m FTS telescope (335 data points) both analyzed in A08 (obtained by private communication), two are from the 1.54 m Danish telescope (174 data points) that are presented in S09, and seven are from the B&C telescope (1870 data points). Of the RV data sets, one includes 16 data points obtained with the CORALIE instrument and

the other one includes 33 data points obtained with the HARPS instrument both presented in T10.

In these available data sets, all time stamps are provided either in the form of Heliocentric JD (HJD) (Euler, FTS, and Danish) or BJD (CORALIE and HARPS). However, time-standards (e.g., UTC or TDB) on which these time systems are based are unspecified in the publications. As Eastman et al. (2010) pointed out, specifying the time standard is important in order to achieve 1 minute accuracy, and the authors recommended to use TDB-based BJD as time system. We confirmed that all time systems in the available data were based on UTC (in private communications), and therefore we converted all of them to TDB-based BJD.

In order to treat the additional photometric data equally with the B&C data, their quoted errors were normalized and rescaled in the same manner as was done for the B&C data, as described in section 5.2. The derived value of β and the rms scatter of the residuals for each transit are given in Table 5.2. For the RV data, systematic errors of $\sim 7 \text{ m s}^{-1}$ may be presented in addition to the quoted internal errors (A08 and T10); these often come from stellar activity (stellar jitter). To add statistical weight to the RV data, we rescaled the quoted RV errors for both the CORALIE and the HARPS data by adding 7 m s^{-1} quadratically. This value is consistent with the upper one of an empirical model of Wright (2005) for a G-type star. We show the collected light curves and RV data in Figure 6.1 and 6.2, respectively, with the best-fit model which is derived in the fitting procedure described in the next section.

6.2 Model Fitting

We fitted all the error-rescaled photometric and RV data jointly with seven additional parameters: the RV semi-amplitude, K , two RV offsets, $V_{\text{offset},j}$ ($j=\{\text{CORALIE, HARPS}\}$), the sky-projected stellar rotational velocity, $V \sin I_s$, and the sky-projected

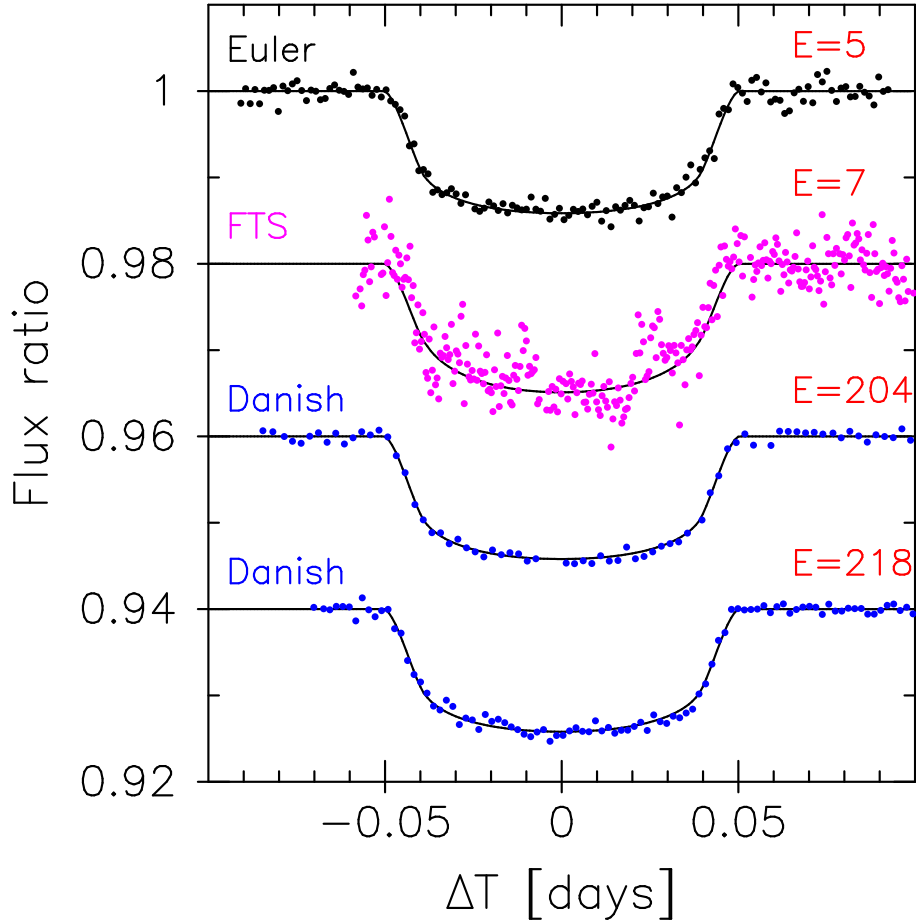


Figure 6.1: The all collected light curves of WASP-5b except for the B&C data. The top light curve with black points was taken by the 1.2 m Euler telescope, the second one with magenta points was obtained by the 2.0 m FTS telescope, and the bottom two with blue points were obtained by the 1.54 m Danish telescope. The Danish’s light curves are the same data shown in Figure 5.3 but are decomposed. The black solid lines show the best-fit models, which will be derived in Section 6.2.

spin-orbit alignment angle, λ , where the last two parameters were needed to model the Rossiter-McLaughline (RM) effect during transits of WASP-5b. The RM formula we used was based on Hirano et al. (2010) (see Appendix C), which is more appropriate than the old one used in the previous work (T10). The formula allowed the parameters of i , R_p/R_* , a/R_* , $T_{c,E}$, K , $V \sin I_s$, $V_{\text{offset},j}$, and λ to be free. We also fitted u_1 for each telescope of the photometric data sets, while u_2 was fixed at the theoretical value (Claret 2000, 2004), because, as mentioned previously, it was difficult to determine unique values for both u_1

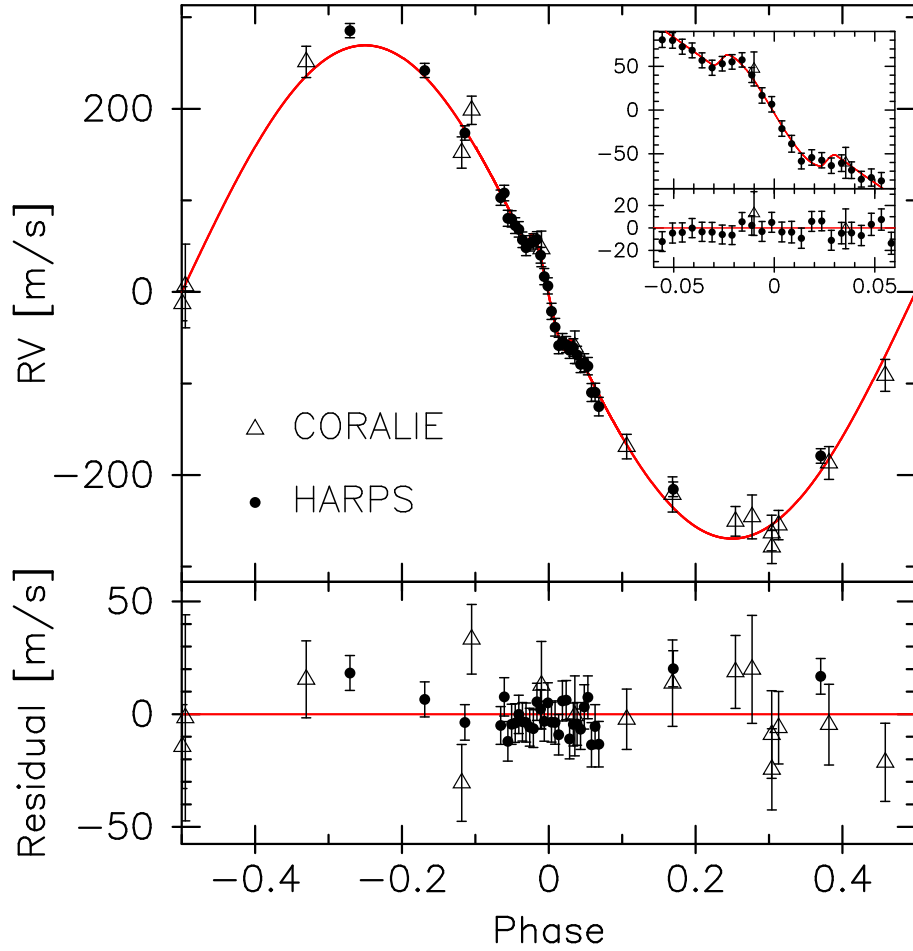


Figure 6.2: The top panel shows the collected RV data obtained by the COLALIE (triangles) and the HARPS (points) instruments with the best-fit model (red line), which will be determined in Section 6.2. The bottom panel shows the residuals. The inset in the top panel shows the zoom around the part where the RM effect is seen.

and u_2 simultaneously due to their strong correlation. As for the eccentricity, we first allowed it to be free, and obtained a value of $0.002^{+0.010}_{-0.002}$. This value is consistent with zero within $1\text{-}\sigma$, and also consistent with the result of T10 ($e < 0.0371$, 2σ), but marginally inconsistent with G09 ($e = 0.049^{+0.020}_{-0.017}$). However, F09 used a smaller RV data set in comparison with T10 and us, and hence we adopted zero for the eccentricity and re-fitted the data. The derived value of u_1 as well as the fixed value of u_2 for each telescope are listed in Table 6.1, and the other best-fit parameters are shown in Table 6.2. The χ^2 values for

the COLALIE and HARPS data sets are 16.0 and 32.7 respectively, which are very close to the number of data points (16 and 33 respectively).

From the combined fit, we refined the transit model parameters of i , R_p/R_* , and a/R_* against the published values, while they are consistent within their error bars. Uncertainties in K and $V \sin I_s$ became larger than the ones determined by T10 because we incorporated the stellar jitter in the RV errors. We adopted the value of the stellar mass as the one determined spectroscopically by T10, and used this to convert fitted parameters to physical parameters. The derived parameters are given in Table 6.3.

We confirmed that the projected spin-orbital angle λ is consistent with zero ($\lambda = 7.2^{+9.5^\circ}_{-9.5^\circ}$), which was first reported by T10, by adding independent photometric data (the B&C and Danish data) and using an improved RM formula.

Table 6.1: Limb-darkening coefficients. *

Telescope	Filter	u_1 (fitted)	u_2 (fixed)
Euler	R	$0.33^{+0.05}_{-0.05}$	0.32
FTS	SDSS i'	$0.49^{+0.12}_{-0.13}$	0.32
B&C	I	$0.27^{+0.05}_{-0.05}$	0.32
Danish	R	$0.34^{+0.04}_{-0.04}$	0.32

* Quadratic limb-darkening coefficients (u_1 and u_2) for each telescope used for the final joint fit. Each u_1 was allowed to be free while each u_2 was fixed at the theoretical value extracted from tables of Claret (2000) or Claret (2004).

Table 6.2: Best-fit parameters and their 1σ uncertainties.*

	This work (B&C only)	This work (all)	Southworth et al. (2009)	Triaud et al. (2010)
P [days]	1.6284301 ± 0.0000012	$1.62843142 \pm 0.00000064$	1.6284246 ± 0.0000013	$1.6284229^{+0.0000044}_{-0.0000039}$
T_0 [$BJD_{TDB} - 2450000$]	4375.62589 ± 0.00052	4375.62510 ± 0.00019	4375.62569 ± 0.00024	$4373.996764^{+0.00015}_{-0.00014}$
i [°]	$85.01^{+1.17}_{-0.78}$	$85.58^{+0.81}_{-0.76}$	85.8 ± 1.1	$86.2^{+0.8}_{-1.7}$
R_p/R_*	$0.1116^{+0.0010}_{-0.0014}$	0.1108 ± 0.0011	0.1110 ± 0.0014	$0.1105^{+0.0019}_{-0.0007}$
a/R_*	$5.26^{+0.23}_{-0.17}$	5.37 ± 0.15	$5.41^{+0.17}_{-0.18}$	$5.49^{+0.37}_{-0.12}$
K [m s^{-1}]	-	269.4 ± 3.3	-	$268.7^{+1.7}_{-1.9}$
e	0 (adopted)	0 (adopted)	0 (adopted)	< 0.0371
$V \sin I$ [km s^{-1}]	-	3.05 ± 0.41	-	$3.24^{+0.34}_{-0.35}$
λ [°]	-	7.2 ± 9.5	-	$12.4^{+8.2}_{-11.9}$

* Best-fit parameters and their $1\text{-}\sigma$ uncertainties for WASP-5b derived from joint fits for the 7 B&C light curves (the second column) and for all available RV and photometric data (the third column) are listed. Parameters derived by S09 (the fourth column) and T10 (the rightmost column) are shown for comparison.

Table 6.3: Derived physical values and their uncertainties for the WASP-5b system.*

	This work	Southworth et al. (2009)	Triaud et al. (2010)
a [AU]	0.02702 ± 0.00059	$0.02729 \pm 0.00049 \pm 0.00027$	$0.02709^{+0.00056}_{-0.00062}$
R_* [R_\odot]	1.082 ± 0.038	$1.084 \pm 0.040 \pm 0.011$	$1.056^{+0.080}_{-0.029}$
M_* [M_\odot]	1.000 ± 0.065^a	$1.021 \pm 0.055 \pm 0.030$	$1.000^{+0.063}_{-0.067}$
ρ_* [ρ_\odot]	0.79 ± 0.10	$0.803 \pm 0.080 \pm 0.000$	$0.84^{+0.07}_{-0.15}$
R_p [R_{jup}]	1.167 ± 0.043	$1.171 \pm 0.056 \pm 0.012$	$1.14^{+0.10}_{-0.04}$
M_p [M_{jup}]	1.568 ± 0.071	$1.637 \pm 0.075 \pm 0.033$	$1.555^{+0.067}_{-0.070}$
ρ_p [ρ_{jup}]	0.92 ± 0.11	$1.02 \pm 0.14 \pm 0.01$	1.05 ± 0.20

* The values presented in S09 and T10 are shown for comparison.

^a The value derived by T10 was adopted.

6.3 Measurement of TTVs

We give the derived transit timings with 1σ uncertainties in Table 6.4. By using these data, a new ephemeris was calculated via a linear fit using a function,

$$T_{c,E} = T_{c,0} + EP, \quad (6.1)$$

where $T_{c,0}$ is a reference time of $E=0$. The results are $T_{c,0}$ [BJD_{TDB}] = 2454375.62510 \pm 0.00019 and $P = 1.62843142 \pm 0.00000064$ d. This fit yields $\chi^2 = 32.2$ for 9 degrees of freedom, which indicates that the fit does not match the data at a confidence level of 99.982%, or 3.7σ . Figure 6.3 shows the timing residuals from the fit.

This result implies that we see excess variations in transit time either due to unknown

Table 6.4: Transit Timings and their uncertainties.

Epoch	Transit Timing [BJD _{TDB} - 2,450,000]	1 σ uncertainty	Telescope
5	4383.76751	0.00028	Euler
7	4387.02286	0.00086	FTS
160	4636.17465	0.00047	B&C
204	4707.82531	0.00021	Danish
218	4730.62252	0.00022	Danish
244	4772.96212	0.00051	B&C
432	5079.10849	0.00044	B&C
451	5110.04645	0.00073	B&C
459	5123.07627	0.00041	B&C
607	5364.08262	0.00057	B&C
615	5377.10969	0.00048	B&C

systematic effects or possibly due to real TTVs. A liner fit for the B&C data only yields $\chi^2 = 17.1$ for 5 degrees of freedom, which corresponds to a confidence level of 99.57% or 2.9 σ , while the fit for the other 4 data yields $\chi^2 = 9.8$, which corresponds to a confidence level of 99.27% or 2.7 σ . Even if we discarded two data points that have the largest uncertainties (corresponding to the epochs of $E=7$ and 451) in all the 11 timing data, suspecting large systematics in the two, a liner fit still gives the χ^2 value of 27.1 for 7 degrees of freedom, which corresponds to a confidence level of 99.968% or 3.6 σ . These results imply that the TTV excess found by G09 still presents, who measured $\chi^2/dof = 5.7$ for a linear fit to four timing data (two of them were derived from the same photometric data), which corresponds to a significance of 99.67% or 2.9 σ . We will discuss a possibility of a systematic effect arising from the baseline corrections of the light curves in section 8.2; although, the timing excess cannot be explained entirely.

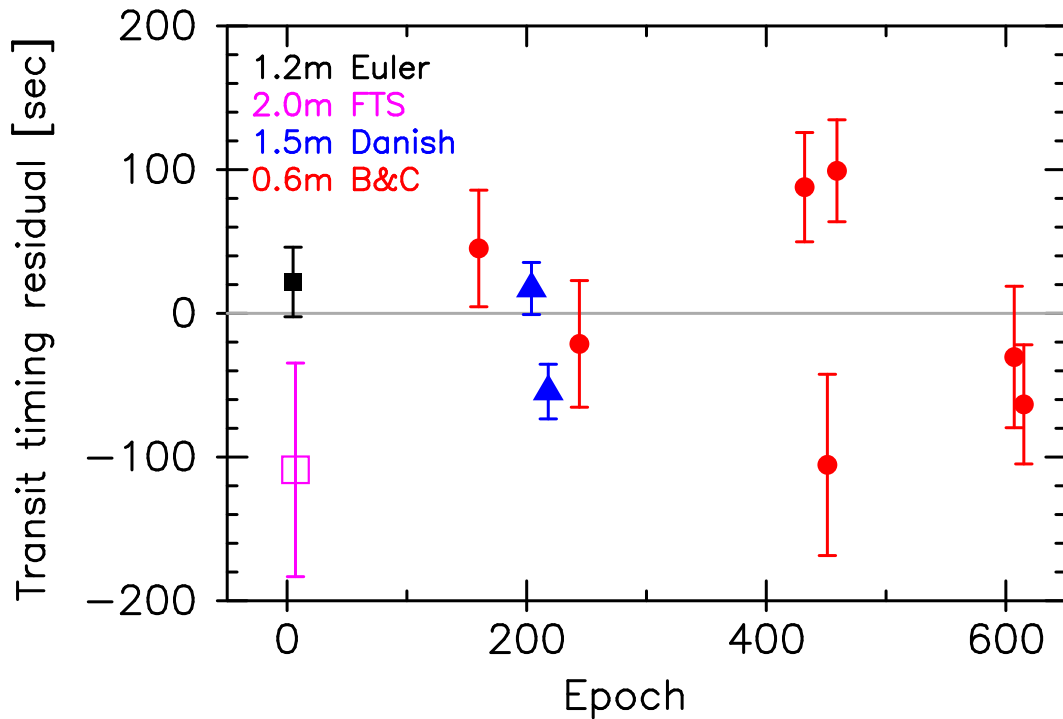


Figure 6.3: Transit Timing residuals for WASP-5b using the new ephemeris determined in this work. The black filled square is the Euler data, the magenta open square is the FTS data, two blue triangles are the Danish data, and seven red circles are the B&C data.

The standard deviation of the observed timing residuals is 68 s, and the mean of the timing uncertainties is 41 s; therefore, if this is a real TTV signal, the actual standard deviation of the TTV is expected to be ~ 50 s. Such a large timing deviation could not be explained by any effect other than additional perturbing bodies. The sizes of these alternative possibilities are: the Applegate effect (~ 1.5 s per 11 yr, Watson & Marsh 2010), the light travel time effect due to an outer massive body ($\lesssim 1$ s per 3 yr, e.g. Agol et al. 2005), the orbital decay caused by tidal dissipation (~ 5 ms yr $^{-1}$, Hellier et al. 2009), and the orbital precessions due to tidal deformations, due to the general-relativity effect, and due to the stellar quadrupole moment (< 130 ms yr $^{-1}$, < 2 ms yr $^{-1}$, < 0.005 ms yr $^{-1}$,

respectively, Heyl & Gladman 2007; Jordán & Bakos 2008) (see Table 6.5). In addition, the presence of an exomoon also could not be responsible for the signal, because Weidner & Horne (2010) placed an upper mass, $9.1 \times 10^{-4} M_{\oplus}$, and distance, $4.39 R_{\text{Jup}}$, of a possible moon for the WASP-5b system by considering the three-body stability issue; such moon would result in only ~ 0.02 s TTVs. Thus, the remaining possibilities for explaining the signal are additional planets or Trojan companions (bodies at 1:1 MMR).

Table 6.5: Expected TTVs for WASP-5b induced by effects other than that of an additional perturbing planet or Trojan. *

Effect	Expected TTVs	Reference
The Appregate effect	$\sim 1.5 (T_{mod}/11\text{yr})$ [s]	Watson & Marsh (2010)
Light travel time effect	$\lesssim 1$ [s/3yr] ^a	e.g. Agol et al. (2005)
Exo-moon	$\lesssim 20$ [ms]	Kipping (2009a); Weidner & Horne (2010)
Tidal dissipation	~ 5 [ms yr ⁻¹] ^b	Hellier et al. (2009)
Orbital precessions due to ...		
tidal deformations	< 130 [ms yr ⁻¹] ^c	Heyl & Gladman (2007); Jordán & Bakos (2008)
general relativistic effect	< 2 [ms yr ⁻¹] ^c	Heyl & Gladman (2007); Jordán & Bakos (2008)
stellar quadrupole moment	< 0.004 [ms yr ⁻¹] ^c	Heyl & Gladman (2007); Jordán & Bakos (2008)

* T_{mod} denotes the modulation time-scale of the host star.

^a The case having a Jovian-mass secondary planet with an orbital period of ~ 3 years, which corresponds to the actual observational period. This produces the RV amplitude of $\sim 21 \text{ m s}^{-1}$ which corresponds to the upper limit placed from the RV data.

^b Adopted a value estimated for OGLE-TR-56b, whose properties are similar to the ones of the WASP-5b system, as an approximation.

^c Equations of (5), (1), and (3) of Jordán & Bakos (2008) are used for calculating precession rates due to tidal deformations, the general relativistic effect, and stellar quadrupole moment, respectively, and an equation (23) of Heyl & Gladman (2007) into which the rates are substituted is used for calculating the transit timing delays. Eccentricity of the primary planet of 0.032 is adopted which is 3σ upper limit derived in this work.

Chapter 7

Upper Limits on the Mass of the Secondary Companion

Although an excess of transit timings from a linear ephemeris is seen in WASP-5b, the significance is too marginal to be convinced as a planetary signal. With such a low significance, even if the excess is actually caused by an additional planet, it is impossible to determine the characteristics of the planet at this time, because there is a large parameter space: planetary mass, orbital period, eccentricity, position of periapsis, reference phase, mutual inclination, and position of ascending node. Alternatively, from the absence of significant TTVs, we place upper limits on the mass of the hypothetical additional planet as a function of period ratio of the two planets (WASP-5b and the secondary body) by conducting numerical three-body simulations. Section 7.1 describes the numerical simulation and its result, and Section 7.2 shows how we constrained an excess of Trojan mass by using both RV and transit timing data.

7.1 Numerical Simulation

In order to simplify things, we assume that the secondary planet orbits on the same plane as the primary planet, WASP-5b, and that the two planets have initially circular orbits. The coplanarity would be a natural consequence of the disk-planet interaction scenario, which is supported from the observed alignment of the sky-projected spin-orbit angle for WASP-5b. As for the eccentricity, considering only the initially circular orbit is sufficient to put the upper limit of the second planet mass, because the TTV amplitude generally increases as the eccentricity of the second planet increases (e.g. Gibson et al. 2010).

Given an initial orbital-period ratio P_2/P_1 , mass M_2 , and initial phase θ_2 of the secondary planet, we performed numerical integrations of the equations of motion for the three-body system,

$$\frac{d^2\mathbf{x}_i}{dt^2} = - \sum_{j=0(j \neq i)}^2 \frac{GM_j(\mathbf{x}_i - \mathbf{x}_j)}{|\mathbf{x}_i - \mathbf{x}_j|^3}, \quad (7.1)$$

where $i = \{0,1,2\}$ denotes the host star or either of the two planets, \mathbf{x} describes position vectors of these bodies, and G is the gravitational constant. The integrations were performed by using the 4th-order Runge-Kutta method and a time step of 1 s. For each integration, it lasted until an equivalent elapsed time reached 3,000 d, which is three times longer than the actual observational duration. When the primary planet approached the star-observer line in the numerical procedure, the time step was reduced to 0.001 s in order to record the exact transit timing. The recorded transit timings were then fitted with a linear function to obtain a "practical" orbital period and an artificial TTV data. Transit timings of the secondary planet were also extracted in order to calculate its practical orbital period. We also performed a long-term run for the same secondary-planet model up to 10^5 yr with a time step of 100 s, in order to check the long-term stability of the system. A second-planet model was eliminated when the system became unstable, i.e. two planets or

a planet and the star collided, or either of the two planets was scattered away.

The produced artificial TTV data were then compared to the actual TTV data in order to obtain the χ^2 value by using the equation

$$\chi^2 = \sum_{i=1}^{11} \frac{(TTV_{E_i} - TTV_{m,E_i})^2}{\sigma_{TTV_{E_i}}^2}, \quad (7.2)$$

where TTV_{E_i} is the actual TTV of the i th epoch E_i , $\sigma_{TTV_{E_i}}$ is its uncertainty, and TTV_{m,E_i} is the artificial TTV of the epoch E_i , which is the epoch relative to an arbitrary reference one. For a given secondary-planet model (P_2/P_1 , M_2 , and θ_2), a χ^2 value was chosen so as to be a minimum by shifting the reference epoch of the artificial TTV data sequentially.

Assuming that the TTV amplitude was proportional to M_2 (Agol et al. 2005; Holman & Murray 2005), we integrated only the case of $M_2 = 3 \times 10^{-6} M_\odot$ for given P_2/P_1 and θ_2 , and rescaled M_2 (i.e. the amplitude of the artificial TTV data) so that the $\Delta\chi^2$, between the χ^2 value derived above and the χ^2 value for a linear fit, becomes 9.0 (3 σ confidence limit). This procedure was repeated for P_2/P_1 in the range from 0.2 to 5.0 being scaled by a factor 1.005, and for θ_2 being changed by 30° from 0 to 360. We then derived 12 upper-limit values of M_2 from 12 models of θ_2 as a function of the practical period ratio. For a practical period ratio, we derived a maximum upper-limit value by taking a maximum value from linearly-interpolated upper limit lines.

The derived 3 σ upper limits are shown in Figure 7.1. The overplotted green thick-dashed line represents the boundary of the Hill-stable region calculated by the equation of Barnes & Greenberg (2006). We also draw an upper-limit line estimated from the RV data (blue dotted line), which corresponds to an RV amplitude of 21 m s^{-1} ; we take this value by assuming the added error of 7 m s^{-1} to the original RV uncertainties is entirely caused by a possible secondary planet and multiplying the value by three. As a result, outside the Hill-stable region boundaries, we placed much more stringent upper limits down to $2 M_\oplus$ in the 1:2 and 2:1 MMRs than the limits from RV, which correspond to 22-70 M_\oplus over the

period ratio from 0.2 to 5.0.

This result shows that our photometric transit data, combined with some literatures' data, have surely high sensitivity to low-mass planets near 1:2 or 2:1 MMRs with WASP-5b. Moreover, this result excludes a certain type of migration models for WASP-5b: a model which produces additional, several Earth-mass or more massive planets lying near 1:2 or 2:1 MMRs.

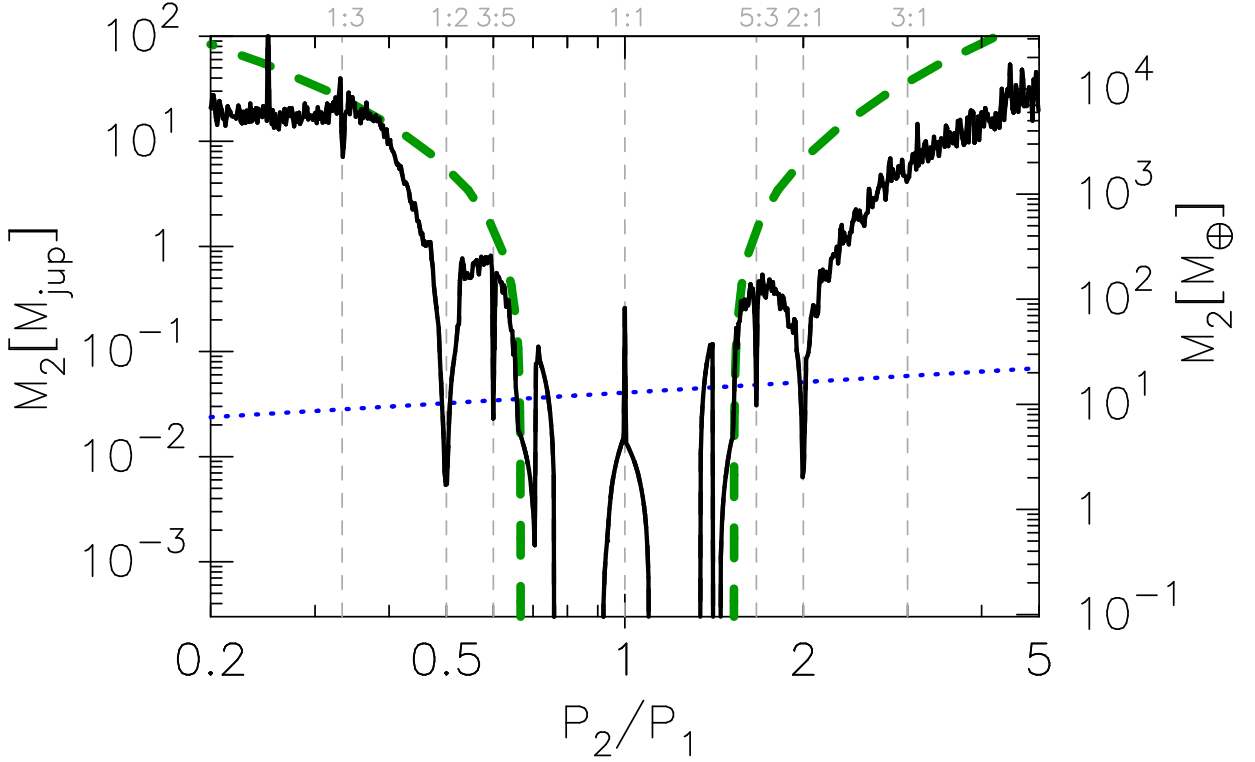


Figure 7.1: Estimated 3σ upper limits on mass of the hypothetical secondary planet as a function of the “practical” orbital-period ratio (black thick-solid line), assuming two planets are coplaner and have initially circular orbits. The blue dotted line represents upper limits on the secondary mass estimated from the RV data, which corresponds to a line causing the RV amplitude of 21 m s^{-1} due to the secondary body. The green thick-dashed line shows boundary of Hill-stable region calculated from Barnes & Greenberg (2006). The gray vertical-dashed lines represent corresponding MMRs.

7.2 Constraining on Excess of Trojan Mass

Bodies on the orbit of 1:1 MMR could be surviving if they lie near the stable Lagrangian L4/L5 points (that lead/trail the planet by $\simeq 60^\circ$). The existence of such bodies on the Jupiter’s orbit in our solar system are well known as Trojan asteroids. Although the total mass of the Trojan asteroids on the Jupiter’s orbit is only $\sim 10^{-4} M_\oplus$ (Jewitt et al. 2000), extrasolar planets may have more massive, even planetary mass, Trojan companions.

From the numerical simulations done in the previous section, we could put an upper limit on the mass of a Trojan body as $\sim 100 M_\oplus$ (3σ), which is seen as a peak feature of the upper-limit line at 1:1 MMR in Figure 7.1. It may seem that the upper limit from the RV data places more stringent limit of $\sim 40 M_\oplus$ at 1:1 MMR, however, it is not true. If a Trojan body exists at either the L4 or L5 point, the observed RV would show as if one planet was orbiting at the barycenter of the primary planet and the Trojan companion. Therefore, in principle, the RV method cannot detect such Trojan objects.

Alternatively, a method to find an excess of Trojan mass by using both RV and photometric information has been proposed by Ford & Gaudi (2006). The schematic view of this method is shown in Figure 7.2. The basic idea of this method is to observe a difference between the time of vanishing stellar RV variation (T_0) and the time of the mid-transit (T_c). Using this method, Madhusudhan & Winn (2009) estimated the upper mass of the imbalance of Trojan companions in the WASP-5 system as $< 54.7 M_\oplus$ (2σ), based on the data of A08. Here, we improved this estimate, by employing more RV and photometric data. We measured the time difference at the transit epoch of 0, $\Delta t = T_{c,0} - T_{0,0}$, with (without) RV data during transit (14 data points), adopting an eccentricity of WASP-5b of zero. Consequently, we derived $\Delta t = 4.8 \pm 4.4$ min (12.8 ± 4.8 min). From this result, we could not find any significant difference in the two times. Accordingly, using this result, we set upper limits on the mass excess of the Trojan companions, M_T , which is defined as the difference in the mass at L4 ($M_{T,L4}$) and the mass at L5 ($M_{T,L5}$) (namely,

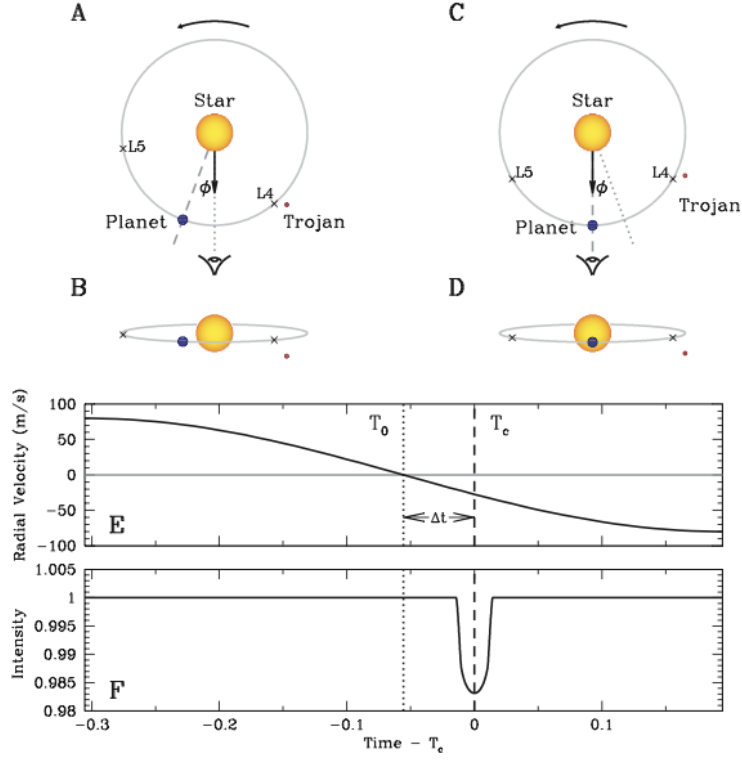


Figure 7.2: Illustration of the method to detect Trojan companions of transiting planets by comparing the transit and RV observations (From Ford & Gaudi (2006)). Views of face-on (A, C) and edge-on (B, D) of a planet+Trojan system are shown at the top. The gray circle shows the orbit of the planet and Trojan. The dotted line indicates the direction of the acceleration of the star, the dashed line indicates the direction of the transiting planet, and ϕ is the angle between these two directions. The vector shows the direction toward the observer. Panels A and B show the position at T_0 , the time of the stellar reflex RV null. Panels C and D show the position at T_c , the time of the central transit. Panel E shows the stellar reflex RV as a function of time (in units of the period of the planet), with the times T_0 and T_c indicated. Panel F shows the intensity of the transit light curve. The Trojan is assumed to be inclined so that it does not transit the parent star.

$M_T \equiv M_{T,L4} - M_{T,L5}$), through the relation

$$M_T = M_p \left(\frac{2 \tan(2\pi\Delta t/P)}{\sqrt{3} - |\tan(2\pi\Delta t/P)|} \right), \quad (7.3)$$

where P and M_p are the orbital period and mass of WASP-5b, respectively [equation (2) in Madhusudhan & Winn (2009) and originally from equation (1) in Ford & Gaudi (2006)

]. We then found $M_T = 7.4 \pm 6.8$ (19.8 ± 7.7) M_\oplus , and put the upper limit on the excess mass of Trojans near the L4 point of $\sim 28 M_\oplus$ ($\sim 43 M_\oplus$) at the 3σ confidence level. This result lowered the limit derived from only the TTV data ($< 100 M_\oplus$), and improved it compared with that derived by Madhusudhan & Winn (2009) by at least a factor 2.

Chapter 8

Discussion

8.1 Example Models of Secondary Planet

The significance of the observed TTVs is too weak to conclude the detection of a second planet in the WASP-5 system. Nevertheless, it is worthwhile to illustrate example TTV models that could account for the transit timing data to see the possibility of the future detection of an hypothetical additional planet. We then searched for well-explainable models by fitting simulated TTV data to the observed one. Using the artificial TTV data generated in Section 7.1, we searched for the best-fit solution for each orbital period ratio by scaling the TTV amplitude and shifting a reference epoch of the artificial TTV data. At this time, we used only the case that the initial phase of the secondary planet is zero, i.e. initially the star, the second planet, and the observer are aligned, for the sake of simplicity. Since a libration period of TTVs increases rapidly as the period ratio approaches to an MMR, solutions around MMRs should be searched finely. Therefore we generated a set of additional simulated TTV data around MMRs of 1:4, 1:3, 3:5, 5:3, 2:1, 3:1, and 4:1, by 10 times denser than those for the other regions, and searched for best-fit solutions for these additional data. We then converted the best-fit TTV amplitudes to the secondary planet masses, assuming that the TTV amplitude is proportional to the second planet mass. The

derived best-fit mass of the hypothetical second planet is shown in the top panel of Figure 8.1, as a function of the period ratio. We also show the χ^2 map in the second panel of the figure. In addition to the case of $e_2 = 0$, we also generated a set of artificial TTV data for $e_2 = 0.1$, under the same conditions as the previous ones and in an additional condition: the initial position of the periapsis of the second planet was set to zero. In this case, the regions around the MMRs of 1:4, 1:3, 2:5, 3:5, 2:1, 5:2, 3:1, and 4:1 were searched densely. We then searched for the best-fit solutions against the respective period ratios by the same procedures as the previous practice. We show the results for $e_2 = 0.1$ in the lower two panels of Figure 8.1.

As a result of these practices, we found the followings. First, for the case of $e_2 = 0$, the possible period ratios where the best-fit masses of the hypothetical second planet are lower than the upper limits placed from the RV data, are only around the low-order MMRs, such as 1:3, 1:2, 3:5, 5:3, 2:1, and 3:1. Then the possible period-ratio regions extend to around many other MMRs and some non-MMR regions for the case of $e_2 = 0.1$. Therefore, as long as the observed TTVs are induced by a second planet and its eccentricity and mutual inclination are both nearly zero, the second planet would probably exist in low-order MMRs. Such configurations would have been a consequence of the disk-planet interaction process of WASP-5b.

Next, there are surely some explainable TTV models in such low-order MMRs. One can see that the χ^2 maps have a number of local minima over the examined period-ratios, reflecting the fact that the libration period of TTVs expands or contracts sensitively in the vicinities of MMRs, and there are some solutions which have low- χ^2 values in low-order MMRs. Figure 8.2 shows the enlarged versions around the 2:1 MMR of Figure 8.1, for example.

In Figure 8.3, we show four example TTV models (a, b, c, and d), which satisfy that the second planet is located near an MMR and the mass is lower than the limit placed from

the RV data, as well as the χ^2 value is low enough to explain the observed TTVs. The four models are: (a) the least χ^2 model ($\chi^2 = 4.35$ for 8 degrees of freedom) in all models, being located near the 1:2 MMR and having the mass of $0.003 M_{\text{Jup}}$ and $e_2 = 0$; (b) a low- χ^2 model ($\chi^2 = 5.01$), being located near the 2:1 MMR and having the mass of $0.093 M_{\text{Jup}}$ and $e_2 = 0$; (c) another low- χ^2 model ($\chi^2 = 6.65$), being located near the 2:1 MMR and having the mass of $0.011 M_{\text{Jup}}$ and $e_2 = 0.1$; (d) a long libration model, being located near the 4:1 MMR and having the mass of $0.053 M_{\text{Jup}}$ and $e_2 = 0.1$, with a χ^2 value of 20.57. Although the last one has relatively high χ^2 value, it may still be acceptable.

The models of (a), (c) and (d) show large differences in libration period and amplitude, and therefore continuous observations with the current facility could distinguish them. However, the models (a) and (b) show similar libration periods and amplitudes, indicating that much more precise and frequent TTV observations would be necessary to distinguish these models. To achieve this, observations of consecutive transits with multiple larger telescopes (mirror diameter $\gtrsim 2\text{m}$) located around the world would be ideal. Additional high-precision RV observations would also be helpful to constrain the models. Future observations such as these will reveal the true nature of the TTVs in WASP-5b, which will shed light on the migration mechanism of WASP-5b.

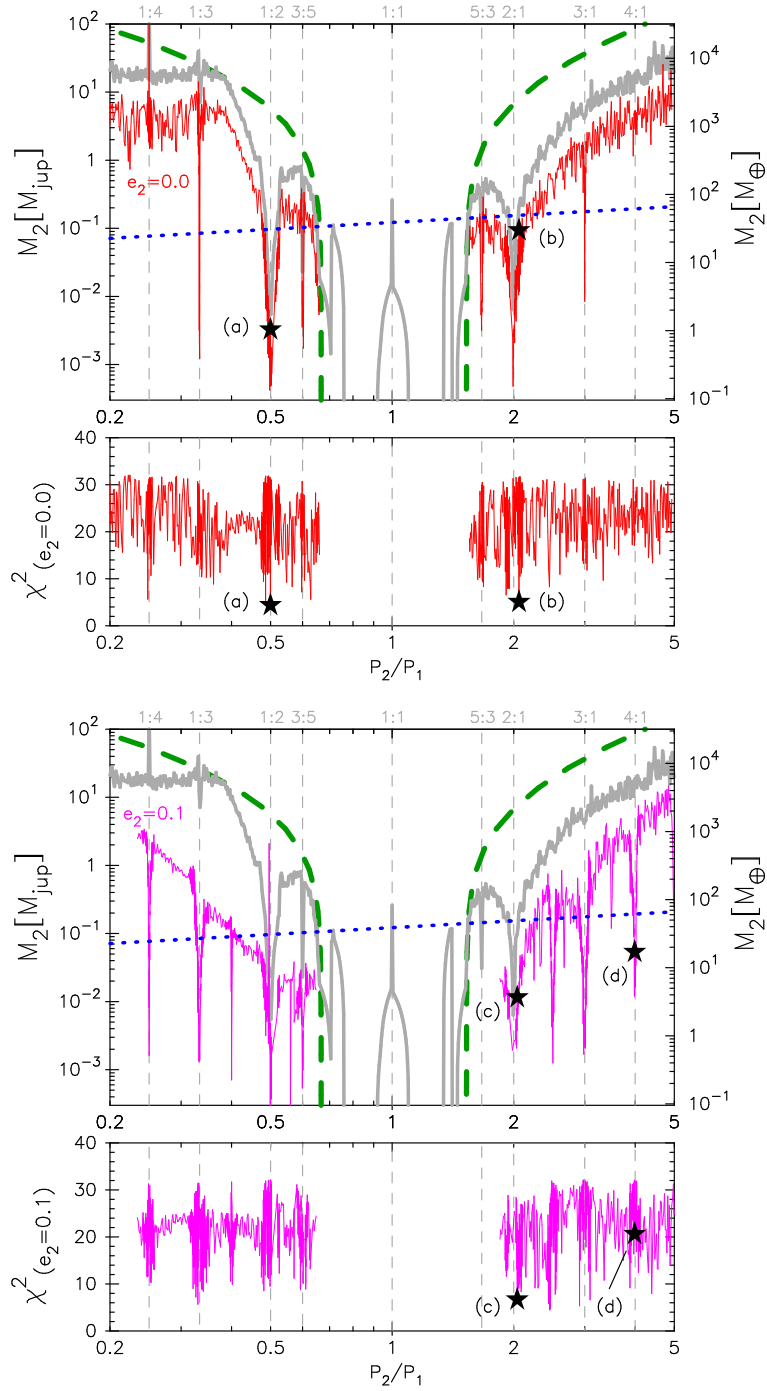


Figure 8.1: Best-fit mass regions of the hypothetical second planet as a function of the orbital period ratio (thin-solid lines in the top and the third panels) and their χ^2 values (the second and the bottom panels), for the case of $e_2 = 0$ (upper two panels) and 0.1 (lower ones). A coplanarity of the two planets was assumed in both cases. The gray thick lines are the same as the black one in Figure 7.1. The locations of example TTV models shown in Figure 8.3 are marked as star symbols with alphabets of (a), (b), (c), and (d).

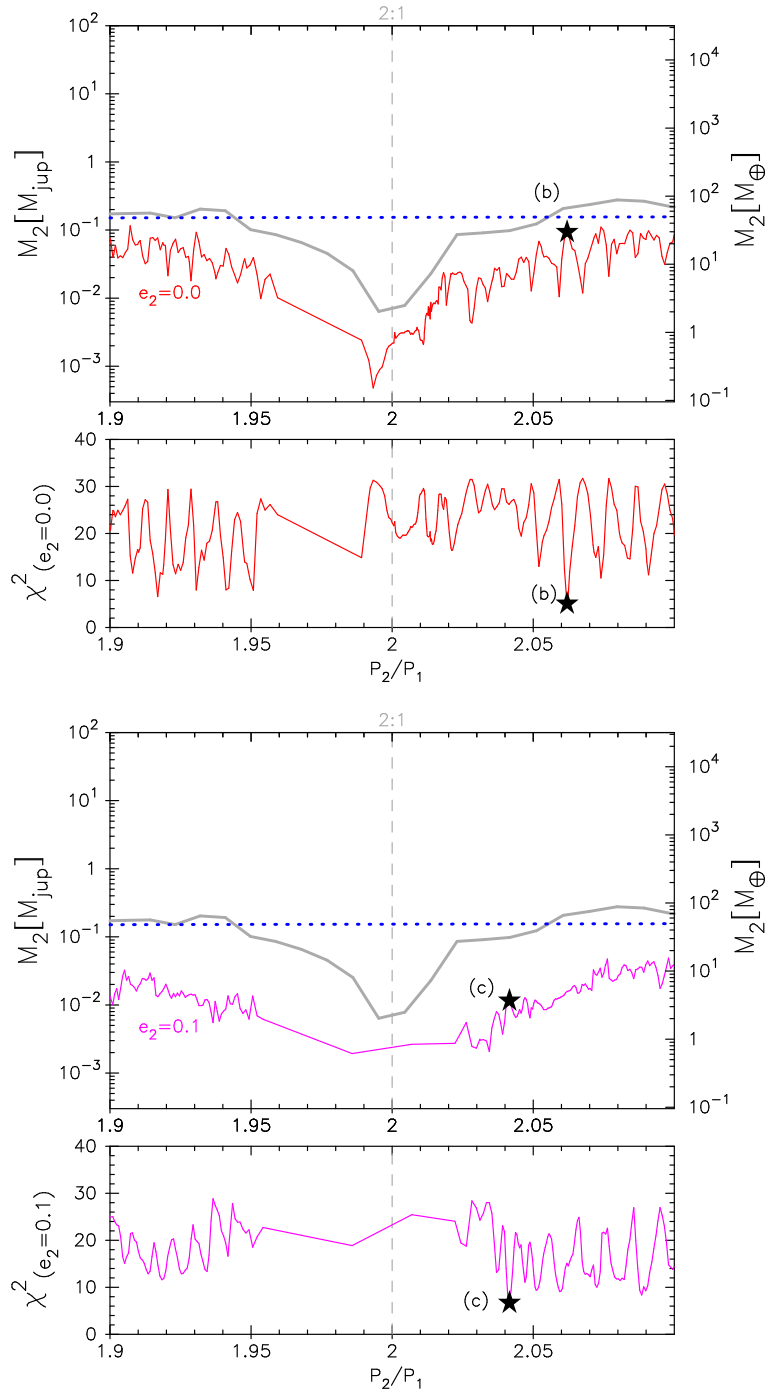


Figure 8.2: Zooms around the 2:1 MMR of Figure 8.1. Discontinuous features are seen in the vicinity of the 2:1 MMR, because the strong resonance near the MMR much excites the eccentricities of the two planets, resulting in the jumps at certain ‘practical’ period ratios.

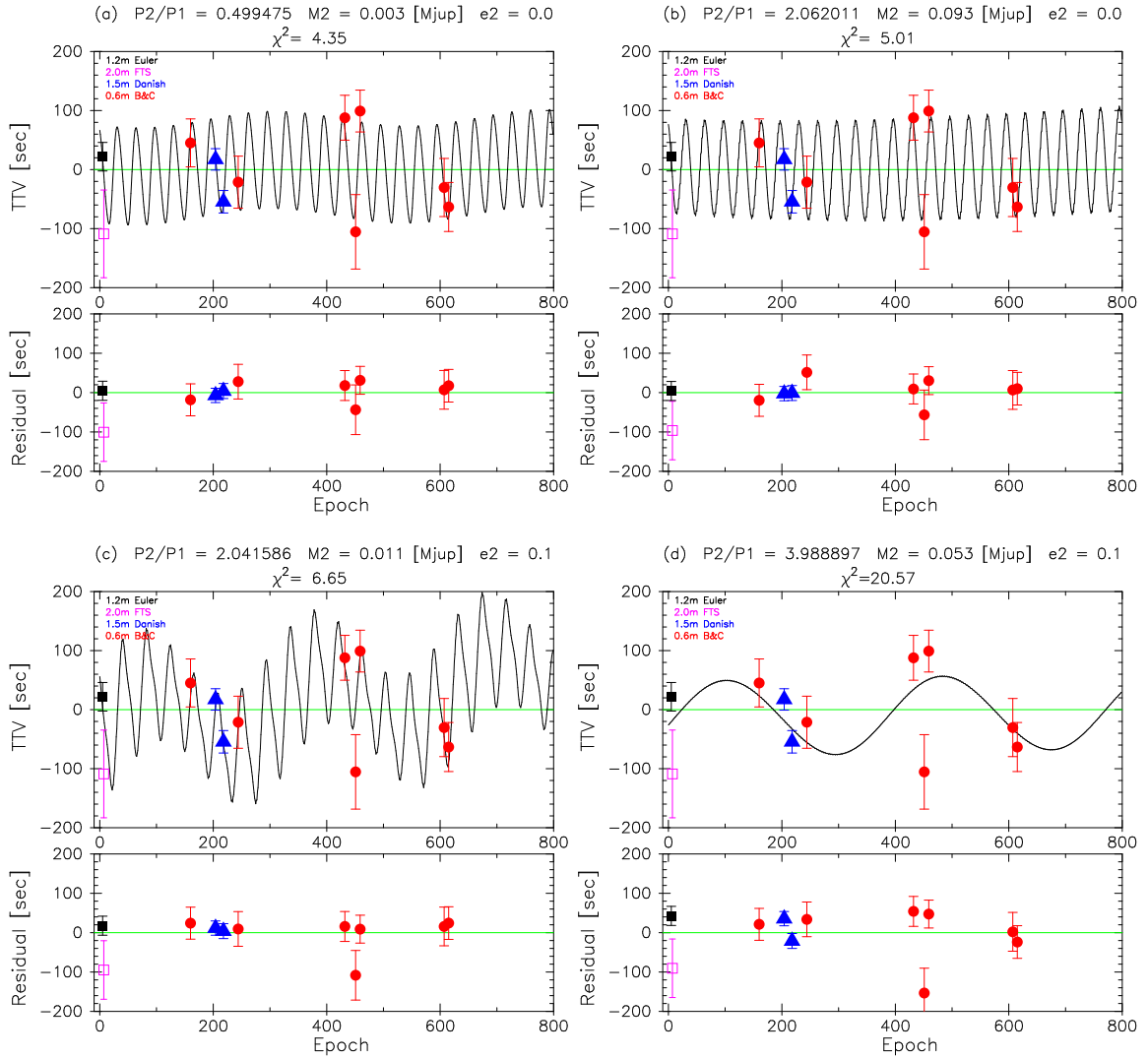


Figure 8.3: Four example TTV models (solid lines) with the observed TTV data (legends are the same as in Figure 6.3) (top panels) and their residuals (bottom panels). The model parameters and χ^2 values are given at the top of the respective examples.

8.2 Correlation with the Correction of Light-Curve Baseline

The observed TTVs in WASP-5b are marginal, and such weak deviations might be explained by some systematics which have not been recognized. One possibility that may account for at least some fraction of the observed TTVs is incompleteness of the baseline corrections for the light curves. In section 5.1, we attributed the systematic trends presented in the light curves to the airmass effects and/or the slow variabilities of the stars, and corrected them by fitting the functions of Equation (5.1) and (5.2) to the light curves; we then forwarded our analyses as the corrections were approximated to be perfect. Such an approximation is often applied in similar works, explicitly or implicitly, however, the imperfect correction of the light-curve baseline could affect the transit timing measurement, and the correlation between the baseline correction and the transit timing, T_c , should be taken into account to the T_c uncertainty. We therefore estimated the impact of the correlation on the T_c uncertainty of our data. Because the baseline trends of the collected light curves of WASP-5b other than those of B&C have already been corrected by each analysts' mean, we have no way to assess the systematics which were produced from their correction procedures; therefore we considered only the B&C light curves.

Generally, it is possible to take into account the error correlation between the baseline correction and T_c in the T_c uncertainty, by including the baseline-correction parameters (k_0 , k_z , k_t , and k_{zt}) as free parameters in the overall fitting procedure as was done in Section 6.2. However, in our fitting procedure, the inclusion of all baseline-correction parameters in free parameters forces the total number of parameter spaces to increase by 4×7 (7 is the number of light curves), and we found that our χ^2 -minimization method could not work robustly with such a large parameter spaces. Instead, we roughly estimated the impact of the error correlation as follows.

To estimate the uncertainty of T_c derived from the baseline correction, we compared two $1\text{-}\sigma$ uncertainties of T_c , (1) $\sigma_{T_c,1}$ and (2) $\sigma_{T_c,2}$: (1) $\sigma_{T_c,1}$ is derived by fitting a baseline-corrected light curve with fixing all parameters except for T_c to the best-fit values determined in Section 6.2 so that T_c is the only free parameter; (2) $\sigma_{T_c,2}$ is derived by fitting the baseline-uncorrected light curve with free parameters of k_i ($i=0, z, t, zt$) and T_c , fixing the other parameters to the same values as in the former practice. The root of the difference of squares of the two, $\sigma_{T_c,\text{diff}} = \sqrt{\sigma_{T_c,2}^2 - \sigma_{T_c,1}^2}$, can be considered as the baseline-correction-derived uncertainty. The resultant values of $\sigma_{T_c,1}$, $\sigma_{T_c,2}$, and $\sigma_{T_c,\text{diff}}$, and the revised uncertainty of T_c , $\sigma_{T_c,\text{rev}}$, which was calculated by adding $\sigma_{T_c,\text{diff}}$ to the original one squarely, are listed in Table 8.1.

As a result, using the revised uncertainties of $\sigma_{T_c,\text{rev}}$, the χ^2 value for a linear fit to the TTVs becomes 24.7 for 9 degrees of freedom, which corresponds to the significance of 2.9σ . A linear fit to the B&C data only yields the χ^2 value of 11.0 for 5 degrees of freedom, which corresponds to the significance of 1.9σ . We can consider these values are the conservative ones, because the four-parameter fit to the light-curve baseline may be redundant for some light curves; while we adopted the four-parameter fit to all the B&C light curves for consistency. Therefore, we believe that the conclusion described in section 6.3 does not change, i.e. the transit timings of WASP-5b are marginally inconsistent with a liner ephemeris. In addition, the results derived in Section 7 and the discussions in the previous section do not largely change even if we consider the additional uncertainties.

Table 8.1: Estimation of baseline-correction-derived uncertainties in T_c .

Epoch	$\sigma_{T_c,1}$ [d] ^a	$\sigma_{T_c,2}$ [d] ^b	$\sigma_{T_c,\text{diff}}$ [d] ^c	$\sigma_{T_c,\text{rev}}$ [d] ^d
160	0.00045	0.00054	0.00030	0.00056
244	0.00050	0.00062	0.00037	0.00063
432	0.00043	0.00060	0.00042	0.00061
451	0.00073	0.00082	0.00035	0.00082
459	0.00040	0.00049	0.00028	0.00050
607	0.00057	0.00079	0.00055	0.00079
615	0.00048	0.00066	0.00045	0.00066

^a T_c uncertainty derived by fitting the baseline-corrected light curve with fixing all parameters to the best-fit values determined in Section 6.2 except for T_c .

^b T_c uncertainty derived by fitting the baseline-uncorrected light curve with free parameters of k_i ($i=0, z, t, zt$) and T_c , fixing the other parameters to the same values as those used for $\sigma_{T_c,1}$.

^c The root of the difference of squares of the two: $\sigma_{T_c,\text{diff}} = \sqrt{\sigma_{T_c,2}^2 - \sigma_{T_c,1}^2}$.

^d The revised uncertainty of T_c , calculated by adding $\sigma_{T_c,\text{diff}}$ to the original one listed in Table 6.4 squarely.

8.3 Statistical Analysis of TTVs in Hot Jupiters

As of June 2011, similar TTV searches to ours have been conducted for about 15 transiting hot Jupiters by a number of groups. Figure 8.4 shows the published transit timing data of 15 transiting hot Jupiters which are listed in Table 2.1 with the addition of WASP-5b.

Among them, two have been claimed to hold possible another planets near MMRs (WASP-3c near 2:1 MMR and WASP-10c near 5:3 MMR, Maciejewski et al. 2010, 2011). Such an MMR planetary pair can form during the disk-planet interaction processes of the two planets, whereas almost never form during the planet-planet interaction process. Therefore at least these two hot Jupiters, if the claims are true, could be considered to have formed via the disk-planet interaction process. During this process, whether a planetary pair will be captured in an MMR or not depends on the relative migration speed, the planetary masses, the eccentricities at the time when the two planets encounter the MMR, and the relative orbital phase. The last quantity is almost random, whereas the relative migration speed and the eccentricities depend on the condition of the protoplanetary disk, such as the amount of the gas and the level of turbulence, at given planetary masses (e.g., Mustill & Wyatt 2011; Ketchum et al. 2011). However, the distributions of disk mass and the level of turbulence are not well known, as well as the theoretical models which predict the migration rate and the eccentricity evolution of a planet in a given disk have large uncertainties. Therefore, observational constraint on the probability that an additional planet appears in an MMR with a hot Jupiter will provide a strong constraint on such theoretical models. Since the TTV method has a strong sensitivity to planets near MMRs with transiting planets, it can be a powerful tool to constrain such probability. In this section, we estimate the probability of second planet occurrence near 2:1 MMR with a hot Jupiter, where one of the most sensitive regions to additional planets by the TTV method (see Figure 7.1).

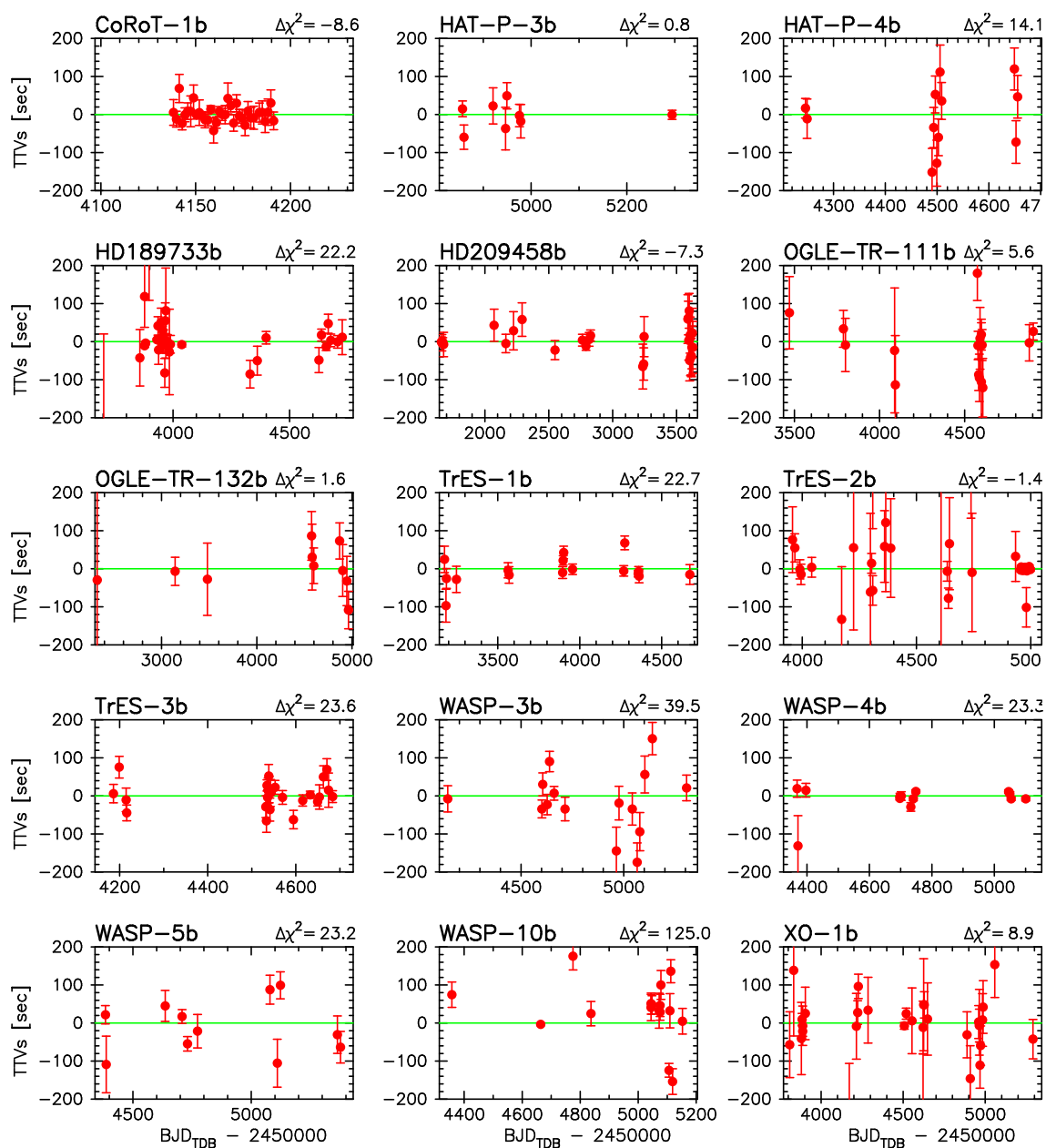


Figure 8.4: The TTV data of 15 transiting hot-Jupiters collected from publications. The references of these data are found in Table 2.1. The $\Delta\chi^2$ value shown at the top right of each panel indicates the χ^2 value for a linear fit to the timing data minus degree of freedom: $\Delta\chi^2 = \chi^2_{\text{linear}} - d.o.f.$

Among the sample of 15 hot Jupiters, only WASP-3b has been argued to show TTVs that can be attributed to the presence of a second planet near the 2:1 MMR with a hot Jupiter. If this argument is true, the second-planet occurrence rate near 2:1 MMR with a hot Jupiter would be simply $1/15 \sim 7\%$. However, this is not the genuine probability because this estimation does not account for the detection efficiency of each observation.

We then calculated the detection efficiency for each of the hot Jupiters by using the published transit timings, whose references are listed in Table 2.1, in addition to the transit timings of WASP-5b listed in Table 6.4. To calculate the detection efficiencies, one needs to define the “detection” of a second planet. Here we placed the detection threshold as $\Delta\chi^2=35$, where $\Delta\chi^2$ is equal to the χ^2 value of a linear fit for a transit timing data minus the degree of freedom, $N - 2$, where N is the number of data points. This threshold level was determined based on the fact that the $\Delta\chi^2$ value for the transit timing data of WASP-5b is 23.2, from which any unique perturber model could not be constrained, while the $\Delta\chi^2$ value for those of WASP-3b is 39.5, from which the authors could find an unique model of WASP-3c. To treat WASP-3c as a “detection”, we choose $\Delta\chi^2=35$ as the threshold.

We first created an efficiency map in the plane of the second-planet mass and the period ratio. Using the same time sampling and the timing errors as the observed transit timing data, we produced artificial TTV datasets by using the same numerical simulation code used in Section 7. For a given M_2 and P_2 , we produced 36 artificial TTV datasets as changing θ_2 by 10 degrees, assuming co-planarity and zero eccentricity of the second planet for simplicity. We then assigned an artificial TTV dataset as a detection when it got the $\Delta\chi^2$ value over the threshold of 35. This exercise was repeated in the grid of the second-planet mass and the period ratio, from the mass of 3×10^{-7} to $10^{-3} M_\odot$ with a scale-up factor of 1.23 and from the period ratio of 1.80 to 2.20 with a step size of 0.01 d. The resultant detection-efficiency map for WASP-5b is shown in Figure 8.5. The red region indicates 100% detection efficiency while the blue region indicates 0% efficiency, and their

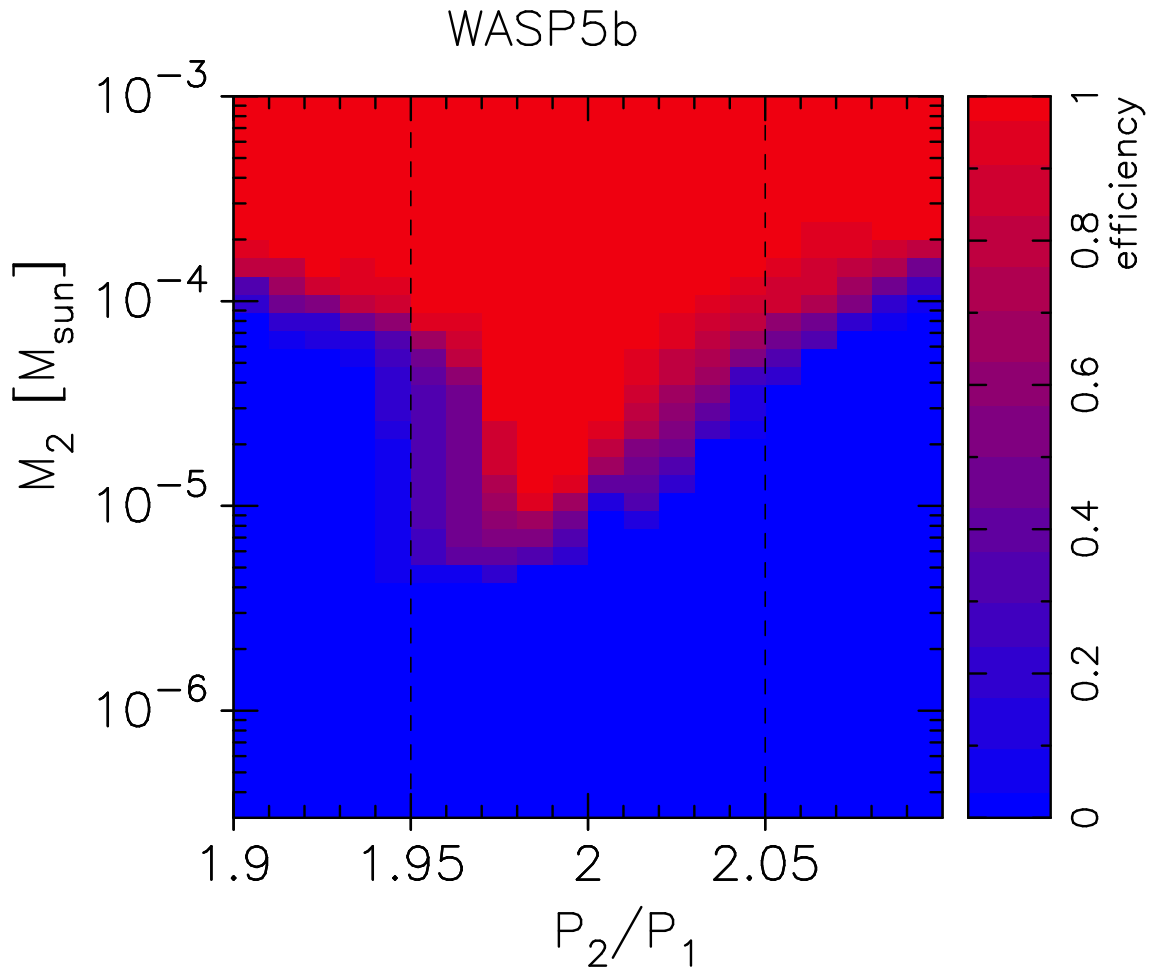


Figure 8.5: The second-planet detection efficiency map for the WASP-5 system, in the plane of second-planet mass and orbital-period ratio around 2:1 MMR with WASP-5b. Co-planarity and zero eccentricity of the second planet are assumed. The red region indicates 100% detection efficiency while the blue region indicates 0% efficiency, and their intermediate colors correspond to the efficiencies indicated at the right-side color legends. Note that the x-axis shows the orbital-period ratio of the ‘initial’ state, instead of the ‘observed’ period ratio.

intermediate colors correspond to the right-side color legends. Note that the x-axis shows the orbital-period ratio of the ‘initial’ state, instead of the ‘practical’ period ratio.

Then, the same calculations were done for the other 14 hot Jupiters. The resultant all efficiency maps including that for WASP-5 are shown in Figure 8.6. A star symbol shown in the map of WASP-3 indicates the location of the claimed second planet, WASP-3c.

The 100% efficiency regions of all samples except for those of CoRoT-1 gradually narrow toward smaller M_2 , reflected that the period-ratio region of 2:1 MMR becomes narrow as M_2 becomes small. For CoRoT-1, the time coverage of the observed transit timings is too short to cover a long-term TTV period which is produced in the case of 2:1 MMR, therefore despite their quite high timing precisions and high sampling rate, the efficiencies for the low-mass region are almost zero.

In order to calculate the frequency of second-planet occurrence near 2:1 MMR with a hot Jupiter as a function of typical second-planet mass, we simply defined the period-ratio range of near 2:1 MMR as from 1.95 to 2.05 regardless of the second-planet mass, and averaged the efficiencies inside this region with respect to each second-planet mass. Figure 8.7 shows the projected efficiencies for all planets, where the averaged-efficiencies of every 0.5 dex in M_2 from 10^{-6} to $10^{-3} M_\odot$ are plotted. The green hatched region in the figure of WASP-3 indicates the region of the claimed WASP-3c.

Using the likelihood analysis, we converted Figure 8.7 to the frequency of the second-planet occurrence near 2:1 MMR with a hot Jupiter as a function of typical second-planet mass, assuming all second planets are co-planer with their primary planets and have zero eccentricities. Using the averaged efficiency $q_i(M_2)$ at M_2 for the i -th hot-Jupiter system, the likelihood function can be expressed by binomial distribution model as

$$L(M_2) = \prod_{i=1}^{N_d} f(M_2)q_i(M_2) \prod_{j=1}^{N_s-N_d} (1 - f(M_2)q_j(M_2)), \quad (8.1)$$

where $f(M_2)$ is the frequency of second-planet occurrence near 2:1 MMR with a hot Jupiter at the second-planet mass of M_2 , assuming all second planets has the same mass, and N_d is the number of second-planet detections among the total number of observed systems N_s . From the likelihood distributions, the median value of $f(M_2)$ and the 90% contained region (for 90% confidence level) were calculated at $M_2 = 3 \times 10^{-5} M_\odot$, where one second-planet was detected, and 90% confidence level upper limits of $f(M_2)$ were calculated for the other

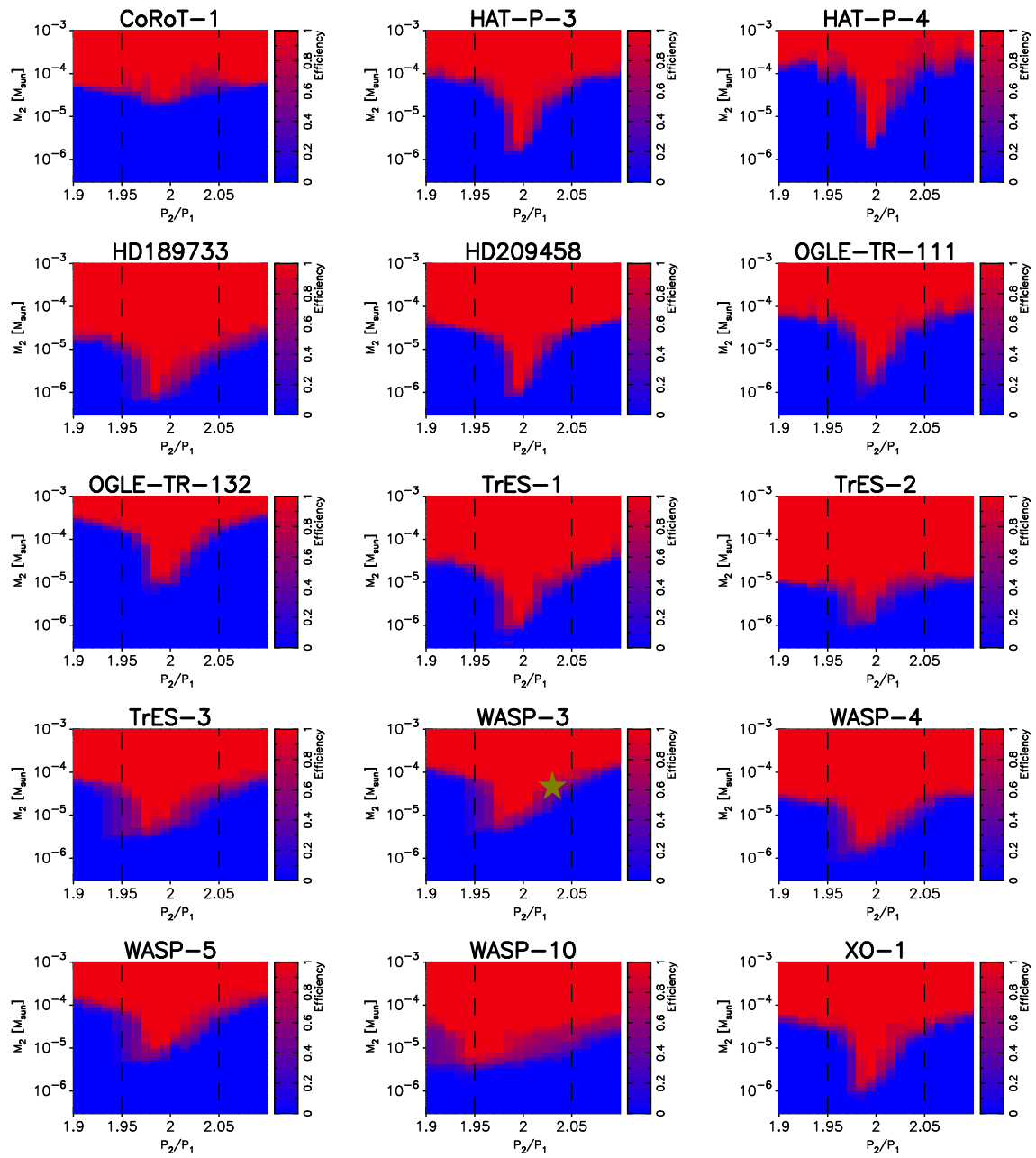


Figure 8.6: The second-planet detection efficiency maps for 15 transiting hot-Jupiters. The axes and the color legends are same as figure 8.5. A star symbol shown in the map of WASP-3 indicates the location of the second planet which has been claimed in the TTVs of WASP-3b.

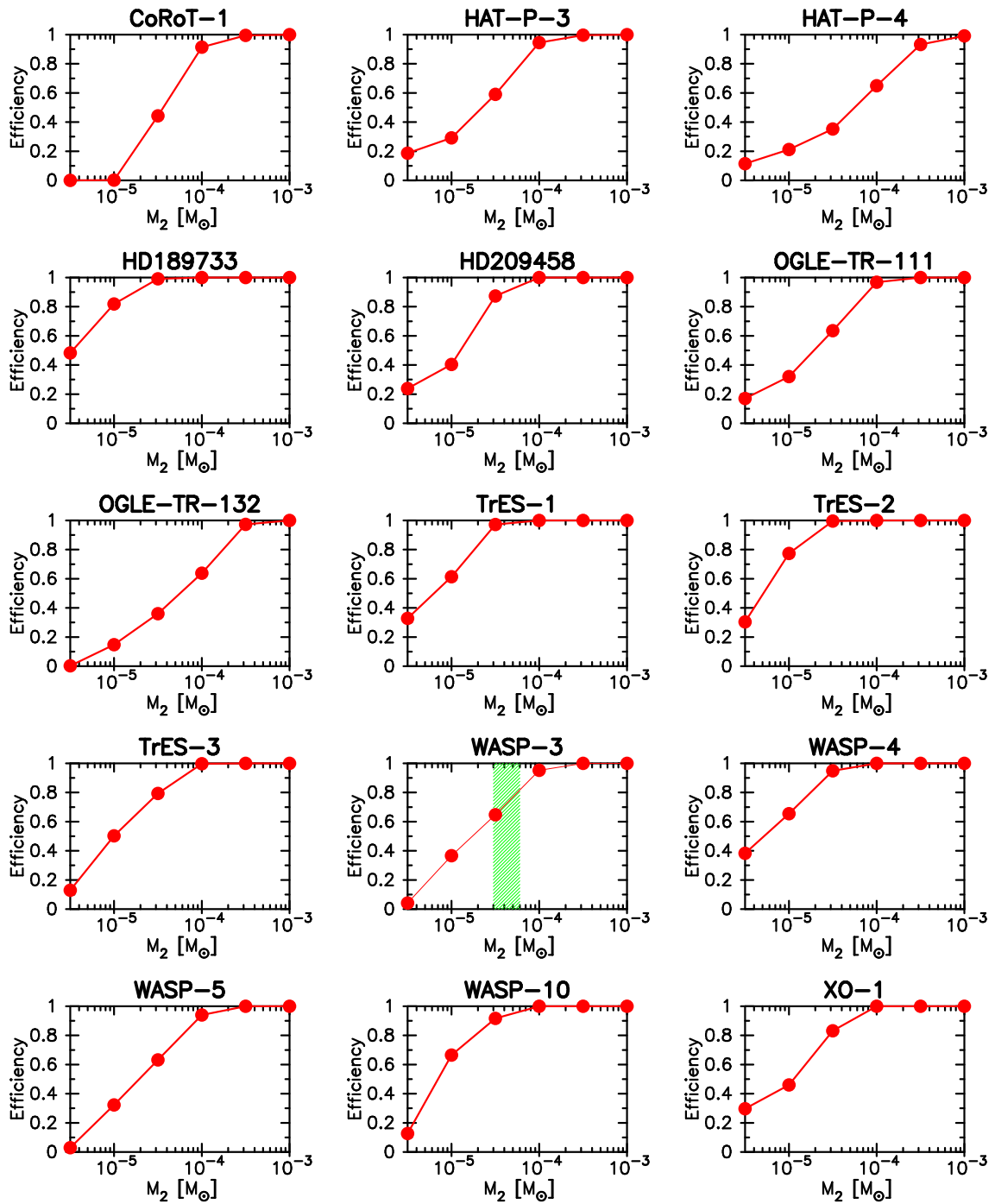


Figure 8.7: Projected detection efficiencies onto the M_2 plane for respective systems (red lines). Each plot represents averaged efficiency over ± 0.25 dex from the representative value of M_2 . The green hatched region in the figure of WASP-3 indicates the region of the claimed WASP-3c.

M_2 values, where no second-planet was detected. The resultant $f(M_2)$, which is the same mean as the number of second planet existing near 2:1 MMR with a hot Jupiter, N_{second} per system, are shown in Figure 8.8. The point with error bars at $M_2 \simeq 10M_{\oplus}$ represents the median value of N_{second} with the 90% confidence region, and the arrows show the 90% confidence upper limits. No meaningful constraint could be placed for $M_2 \sim M_{\oplus}$, however, we found that $N_{\text{second}} = 0.14^{+0.2}_{-0.1}$ at $M_2 \simeq 10 M_{\oplus}$, and N_{second} does not exceed 0.15 for 30 M_{\oplus} or more massive planets at the 90% confidence level. These facts indicate that $\sim 30 M_{\oplus}$ or more massive planets hardly exist near 2:1 MMR with hot Jupiters.

This result does not only confirm the tendency of isolation of hot Jupiters revealed by the RV surveys and the *Kepler*'s transit survey (see Section 1.4.4), but also provide the first-ever quantitative values with respect to the number of second planets per hot-Jupiter system lying near an MMR with hot Jupiters. This result also suggests that a certain type of migration models are excluded as dominant hot-Jupiter migration scenarios: models which produce plenty of somewhat massive ($\gtrsim 10 M_{\oplus}$) planets near MMRs with hot Jupiters.

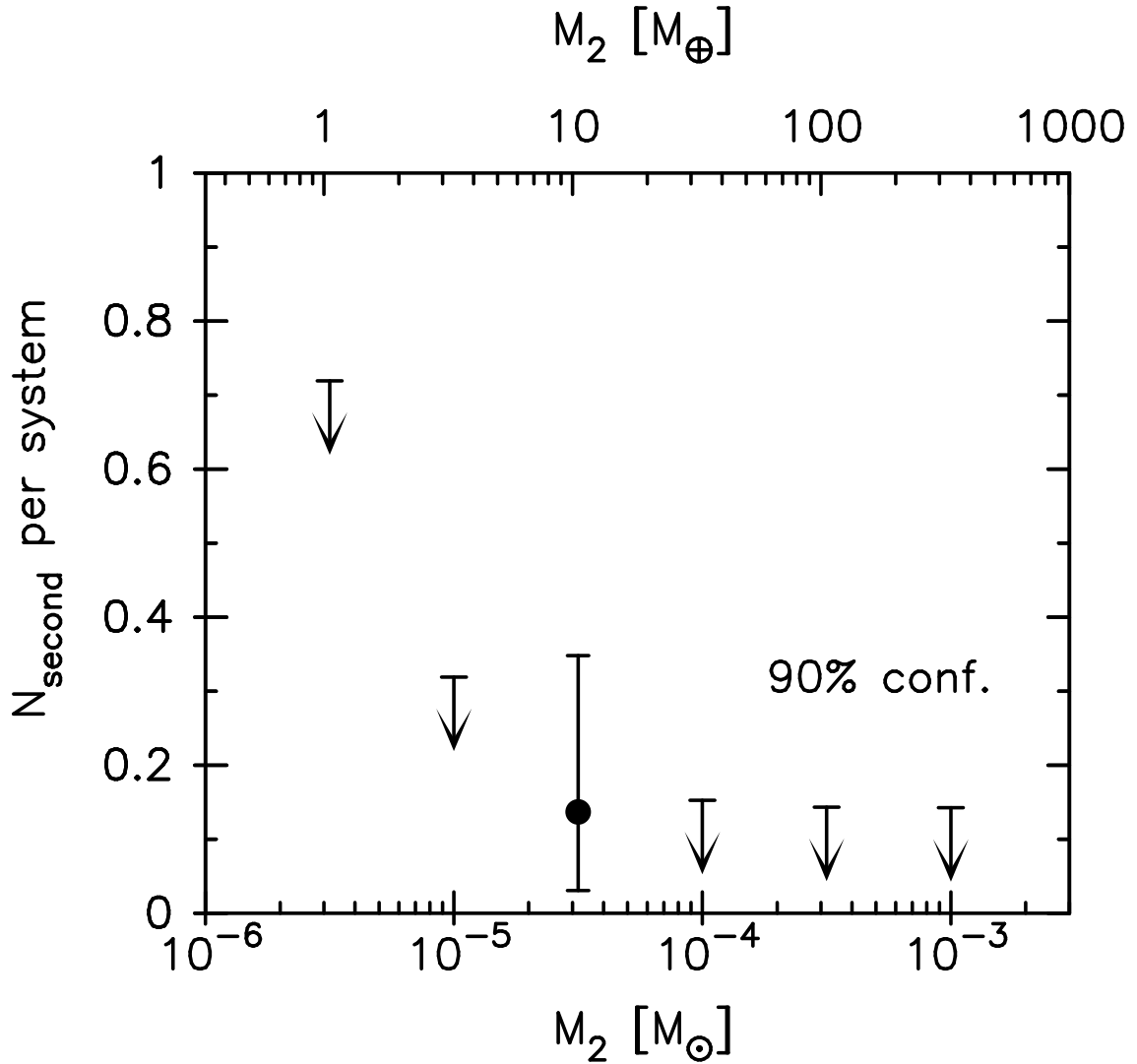


Figure 8.8: The frequency of second planet occurrence near 2:1 MMR (the period ratio from 1.95 to 2.05) with a hot Jupiter as a function of second-planet mass, calculated using the detection-efficiency maps of Figure 8.6. The point with error bars shows the 90% confidence-level region assuming the detection of WASP-3c is real, while the arrows show the 90% confidence upper limits reflecting the non-detections of second planets in their mass range.

8.4 Future Prospects

In this paper, we found a hint of existing TTVs in WASP-5b from multiple transit observations by using a 61 cm telescope. Further transit timing observations of WASP-5b with the current facility will confirm or reject the nature of the TTVs. However, if the observed TTVs are real, more precise and higher cadence photometric observations would be necessary to constrain the mass and the orbital elements of the additional planet, because solving the transit timing inverse problem is generally highly difficult from a limited number of observations (Meschiari & Laughlin 2010). Followup RV observations would also be helpful to constrain them. Note that the RV observations only cannot constrain the orbital inclination, and therefore precise transit-timing observations would be necessary to find out the true nature.

In order to model the observed TTVs with a reliable accuracy, continuous transit observations by using several moderate-size (~ 2 m) telescopes distributed around the world are identical, such as what the LCOGT network is going to do (Shporer et al. 2010). Although much larger (~ 8 m) telescopes can get very precise transit timings, obtaining the telescope time is very competitive, and therefore frequent transit observations with such telescopes are difficult.

In Section 8.3, we have constrained the frequency of second planet occurrence near only 2:1 MMR with a hot Jupiter, assuming only the limiting case that the two planets are coplaner. Increasing the number of hot-Jupiters in the sample as well as the number of timing measurements for each hot Jupiter will allow us to extend this analysis to other MMRs and to another dimension, the orbital inclination of the second planet. Such analyses will provide a more global understanding about the frequency of MMR planets with hot Jupiters, leading to further constraint on the hot-Jupiter migration mechanisms.

Space telescopes for transit survey such as *Kepler* and *CoRoT* will also provide plenty of precise, continuous transit timing data, which will also be very useful for extending our

analysis. Ford et al. (2011) has already found ~ 65 TTV candidates in $\sim 1,200$ transiting planetary candidates detected from the first four months' data of *Kepler*. They will be confirmed or rejected from the *Kepler*'s further observations, and these must provide a valuable information about the planetary migration processes.

Infrared (IR) observations are also capable for measuring transit timings of planets transiting M dwarfs, and these will provide important information about the planetary multiplicity and the frequency of resonance around M dwarfs. From recent RV observations, low-mass planets orbiting G dwarfs tend to exist as multiple in a system but do not tend to be in MMRs (Lovis et al. 2011). Whether the situation for M dwarfs is the same or not is important to understand the planetary formation and migration processes. The TTV method is an ideal tool to test them. Although the number of transiting planets around M dwarfs are quite limited at this time due to the faintness of M dwarfs in the visible wavelength, future high-precision IR Doppler surveys will allow us to find a lot of planets around M dwarfs including transiting ones. The ongoing Japanese IR telescopes such as the 1.4 m IRSF telescope in South Africa, the 1.88 m telescope in Okayama, and the 1 m mini-TAO telescope in Chili, as well as the planning 6.5 m TAO telescope in Chili, are capable of measuring TTVs of planets around M dwarfs precisely, and TTV campaign observations by using a network of these telescopes would be a powerful tool to test for planetary formation and migration mechanisms.

Chapter 9

Conclusion

We observed 7 new transits of the hot Jupiter WASP-5b by using a 61 cm telescope in order to search for an additional body via the TTV method. By combining all available photometric and RV data, we slightly refined the transit-model parameters and confirmed that all parameters were consistent with published values, except for the orbital period; which may be a sign of TTVs. We also confirmed that the sky-projected spin-orbit angle is consistent with zero, which was first reported by Triaud et al. (2010), by including independent photometric data and using an improved RM formula.

The χ^2 value for a linear fit to 11 transit timings is 32.2 for 9 degrees of freedom. This result indicates that the transit timings do not match a linear ephemeris at a confidence level of 99.982 %, or 3.7σ , either due to unknown systematic effects or possibly due to real TTVs. Taking into account the possible imperfect corrections of light curve baselines, the χ^2 value reduces to 24.7, which corresponds to a confidence level of 99.668 % or 2.9σ . We could not find any unique mass and orbital elements of an additional planet from such a low significant TTVs.

From the absence of significant TTV signals, we calculated upper limits of the mass of an hypothetical additional planet by means of numerical simulations, as a function of orbital-period ratio of the two planets. Assuming that the two planets are co-planer, we

placed the limits of $2 M_{\oplus}$ (3σ conf.) for a second planet near 1:2 and 2:1 MMRs with WASP-5b. These limits narrowed the limits placed from the RV data only, where the limits of 22-70 M_{\oplus} over the orbital-period ratio from 0.2 to 5.0 are placed. We also put an upper limit of $43 M_{\oplus}$ (3σ conf.) on excess of Trojan mass using both RV and photometric data.

We also found that, as long as the observed transit timing excess is real and the possible secondary planet has \sim zero eccentricity, it would likely be near low-order MMRs. If this scenario is true, it would support the disk-planet interaction model as the migration mechanism for WASP-5b. Further followup observations for the WASP-5 system by both photometry and spectroscopy will reveal the true nature of the TTV signal.

A brief estimation of the frequency of second-planet occurrence near an MMR with a hot Jupiter was done by analyzing the published transit timing data of 15 hot Jupiters. Assuming that the tentative detection of WASP-3c is real, and the mutual inclination of the two planets and the second-planet eccentricity are zero, we found that the number of second planet near 2:1 MMR with a hot Jupiter, N_{second} , is $0.14^{+0.2}_{-0.1}$ at $M_2 = 10 M_{\oplus}$, and $N_{\text{second}} < 0.15$ for $30 M_{\oplus}$ or more massive planets (90% conf.). This result forbids any models from producing plenty of somewhat massive ($\gtrsim 10 M_{\oplus}$) planets near MMRs with hot Jupiters. Future qualitative and quantitative improvements of transit-timing observations for a larger number of hot Jupiters will shed light on the hot-Jupiter migration mechanisms.

Appendix A

Baseline Correction Function

When we consider primary and secondary atmospheric extinctions, time-averaged standard magnitudes of a target star and a reference star in an arbitrary passband, M_{obj} and M_{ref} , can be expressed as

$$M_{\text{obj}} = m_{\text{obj}} - k'z - k''C_{\text{obj}}z + TC_{\text{obj}} + Z_{\text{p}} + f_{\text{obj}}(t), \quad (\text{A.1})$$

$$M_{\text{ref}} = m_{\text{ref}} - k'z - k''C_{\text{ref}}z + TC_{\text{ref}} + Z_{\text{p}} + f_{\text{ref}}(t), \quad (\text{A.2})$$

where m_{obj} and m_{ref} are observed magnitudes of the target star and the reference star, C_{obj} and C_{ref} are their color indices, z is the airmass, T is the transformation factor, Z_{p} is nightly zero point, k' and k'' are coefficients of primary and secondary extinctions, and $f_{\text{obs}}(t)$ and $f_{\text{ref}}(t)$ are terms of stellar intrinsic variability as a function of time (see e.g., Chapter 6 of Warner 2006). When we approximate that each stellar intrinsic brightness varies with time in linear function, then the differential magnitude between the target star and the reference star, $\Delta M = M_{\text{obs}} - M_{\text{ref}}$, is written as

$$\Delta M = \Delta m - k''\Delta C z + T\Delta C + at + b, \quad (\text{A.3})$$

where $\Delta m = m_{\text{obj}} - m_{\text{ref}}$, $\Delta C = C_{\text{obj}} - C_{\text{ref}}$, and a and b are coefficients. Here, we assume that the k'' varies with time t in linear function, as $k'' = k_0'' + k_1''t$, then

$$\Delta M = \Delta m - (k_0'' + k_1''t)\Delta Cz + T\Delta C + at + b. \quad (\text{A.4})$$

Consequently, if we redefine $k_z \equiv -k_0''\Delta C$, $k_{tz} \equiv -k_1''\Delta C$, $k_t \equiv a$, and $k_0 \equiv T\Delta C + b$, then the correction magnitude $\Delta m_{\text{corr}} = \Delta M - \Delta m$ can be written as

$$\Delta m_{\text{corr}} = k_z z + k_{tz}tz + k_t t + k_0. \quad (\text{A.5})$$

Appendix B

Analytic Transit Light Curve

B.1 The Mandel's Model

To correct the baseline systematics of the transit light curves in Section 5.1, we used analytic formulae derived with a small-planet approximation presented by Mandel & Agol (2002). We here summarize their derivations.

We model a transit as an eclipse of a spherical star by an opaque, dark sphere. In what follows, d is the center-to-center distance between the star and the planet, r_p is the radius of the planet, r_* is the stellar radius, $z = d/r_*$ is the normalized separation of the centers, and $p = r_p/r_*$ is the size ratio (Figure B.1 (b)).

Usually stellar surface brightness is not uniform but peaked at the disk center and darkening toward the limb. This limb darkening effect affects the transit light curve, and so is important to be included in the modeling of the light curve. A non-linear limb darkening law proposed by Claret (2000) is expressed as

$$I(r) = 1 - \sum_{n=1}^4 c_n (1 - \mu^{n/2}), \quad (\text{B.1})$$

where $\mu = \cos \theta = (1 - r^2)^{1/2}$, $0 \leq r \leq 1$ is the normalized radial coordinate on the disk

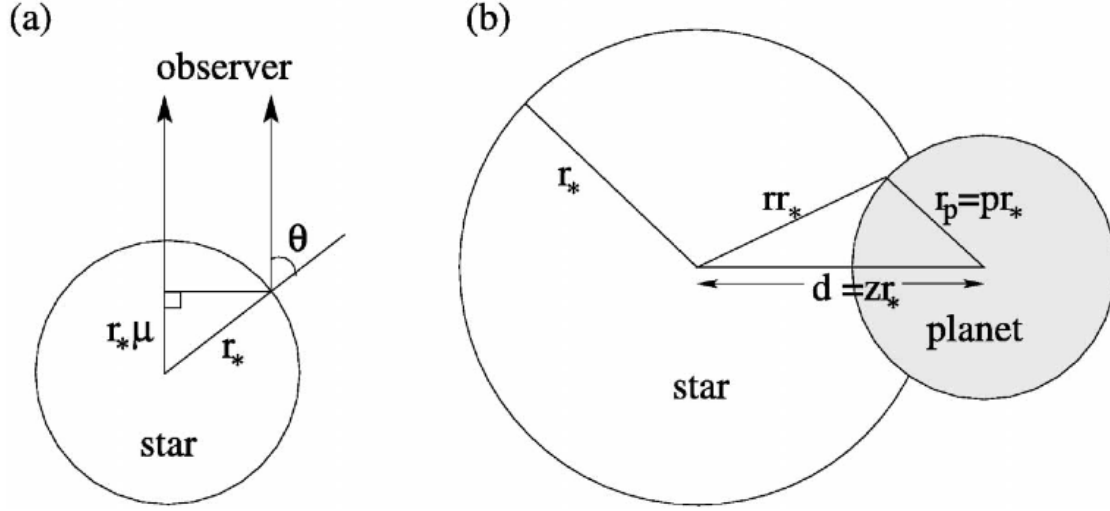


Figure B.1: (a) Geometry of limb darkening. The star is seen edge-on, with the observer off the top of the page. r_* is the stellar radius, and θ is defined as the angle between the observer and the normal to the stellar surface, while $\mu = \cos \theta$. (b) Transit geometry from the perspective of the observer. $p = r_p/r_*$, where r_p is the planetary radius, and $d = z r_*$ is the center-to-center distance.

of the star and $I(r)$ is the specific intensity as a function of r or μ with $I(0) = 1$. Figure B.1 (a) shows the geometry of lensing and the definition of μ . In this paper, we adopted a quadratic limb darkening law in the form of Equation (5.3). In this case, $c_1 = c_3 = 0$, $c_2 = u_1 + 2u_2$, and $c_4 = -u_2$.

For a small planet, $p \lesssim 0.1$, the relative flux of a star partially blocked by the planet can be approximated by assuming the surface brightness of the star is constant under the disk of the planet. When the planet is completely inside the stellar disk, so that $z < 1 - p$, the relative flux to the unobscured flux, F , is written by

$$F = 1 - \frac{p^2 I^*(z)}{4\Omega}, \quad (\text{B.2})$$

$$I^*(z) = \frac{1}{4zp} \int_{z-p}^{z+p} I(r) 2r dr, \quad (\text{B.3})$$

where Ω is defined as

$$\Omega = \sum_{n=0}^4 \frac{c_n}{n+4}, \quad (\text{B.4})$$

which reduces to

$$\Omega = \frac{6 - 2u_1 - u_2}{24} \quad (\text{B.5})$$

for the case of the quadratic limb darkening law.

During ingress or egress of the transit, $1 - p < z < 1 + p$, the relative flux is calculated as

$$F = 1 - \frac{I^*(z)}{4\pi\Omega} \left[p^2 \cos^{-1} \left(\frac{z-1}{p} \right) - (z-1) \sqrt{p^2 - (z-1)^2} \right], \quad (\text{B.6})$$

$$I^*(z) = \frac{1}{1 - (z-p)^2} \int_{z-p}^1 I(r) 2r dr. \quad (\text{B.7})$$

The integral terms of Equation (B.2) and (B.6) are computed numerically.

B.2 The Ohta's Model

In Section 5.3 and 6.2, we used formulae presented by Ohta et al. (2009). In this model, the stellar flux masked by a planet is approximated by analytical formulae instead of calculated numerically. Here we summarize their derivations. Their notations are different from those of the Mandel's model as follows. $\gamma = R_p/R_s$ is the radius ratio and $\rho = \sqrt{X_p^2 + Z_p^2}/R_s$ is the normalized center-to-center distance of the star and the planet when the planet is at (X_p, Z_p) in the x - z plane on the sky-projected stellar surface, where z -axis is aligned with the projected stellar spin axis and the origin is at the center of the star. $I_{\text{star}} = I_0[1 - u_1(1 - \mu) - u_2(1 - \mu)^2]$ is the stellar intensity assuming a quadratic limb

darkening law, where I_0 is the intensity at the center of the star and $\mu = \sqrt{1 - (x^2 + z^2)/R_s^2}$ is the directional cosine between the line of sight and the normal vector to the local stellar surface.

The relative flux of the star to the unmasked flux is calculated by

$$F = \frac{\iint I(x, z) dx dz}{\iint I_s(x, z) dx dz}, \quad (\text{B.8})$$

where $I(x, z)$ and $I_s(x, z)$ represent intensities at a given position (x, z) , so that

$$I(x, z) = \begin{cases} 0 & : x^2 + z^2 > R_s^2 \\ 0 & : (x - X_p)^2 + (z - Z_p)^2 \leq R_p^2 \\ I_{\text{star}}(\mu) & : \text{otherwise,} \end{cases} \quad (\text{B.9})$$

$$I_s(x, z) = \begin{cases} 0 & : x^2 + z^2 > R_s^2 \\ I_{\text{star}}(\mu) & : x^2 + z^2 < R_s^2. \end{cases} \quad (\text{B.10})$$

The denominator of Equation (B.8) can be integrated analytically:

$$\iint I_s(x, z) dx dz = \pi I_0 R_s^2 \left(1 - \frac{u_1}{3} - \frac{u_2}{6}\right). \quad (\text{B.11})$$

On the other hand, the numerator reduces to

$$\iint I(x, z) dx dz = \pi I_0 R_s^2 \left[\left(1 - \frac{u_1}{3} - \frac{u_2}{6}\right) - \frac{1}{\pi} A(\rho, \gamma) \right], \quad (\text{B.12})$$

where

$$A(\rho, \gamma) = \begin{cases} \pi\gamma^2[1 - u_1 - u_2(2 - \rho^2 - \gamma^2/2) + (u_1 + 2u_2)W_1] & : \rho < 1 - \gamma \\ (1 - u_1 - 3u_2/2)[\gamma^2 \cos^{-1}(\zeta/\gamma) + \sin^{-1} z_0 - \rho z_0] \\ \quad + (u_2/2)\rho[(\rho + 2\zeta)\gamma^2 \cos^{-1}(\zeta/\gamma) - z_0(\rho\zeta + 2\gamma^2)] \\ \quad + (u_1 + 2u_2)W_3 & : 1 - \gamma \leq \rho \leq 1 + \gamma \\ 0 & : 1 + \gamma < \rho. \end{cases} \quad (\text{B.13})$$

The variables z_0 and ζ are written in terms of γ and $\eta_p = \rho - 1$ as

$$z_0(\gamma) = \frac{\sqrt{(\gamma^2 - \eta_p^2) [(\eta_p + 2)^2 - \gamma^2]}}{2(1 + \eta_p)}, \quad (\text{B.14})$$

$$\zeta(\gamma) = \frac{\eta_p^2 + 2\eta_p + \gamma^2}{2(1 + \eta_p)}. \quad (\text{B.15})$$

Here, the functions W_i ($i = 1, 3$) are expressed as

$$W_1 = \frac{1}{\pi R_p^2} \iint_S dx dz \sqrt{1 - (x^2 + z^2)/R_s^2} \quad (\text{B.16})$$

$$\simeq (1 - \rho^2)^{1/2} - \gamma^2 \frac{2 - \rho^2}{8(1 - \rho^2)^{3/2}} + \mathcal{O}(\gamma^4), \quad (\text{B.17})$$

$$W_3 = \iint_S d\tilde{x} d\tilde{z} \sqrt{1 - \tilde{x}^2 - \tilde{z}^2} \quad (\text{B.18})$$

$$\simeq \frac{\pi}{6}(1 - x_0)^2(2 + x_0) + \frac{\pi}{2}\gamma(\gamma - \zeta) \quad (\text{B.19})$$

$$\times \frac{g(x_c; \eta_p, \gamma)}{g(1 - 2s\gamma; -\gamma, \gamma)} W_1(1 - \gamma), \quad (\text{B.20})$$

where the function g is given by

$$g(\tilde{x}; \eta_p, \gamma) \equiv (1 - \tilde{x}^2) \sin^{-1} \left\{ \frac{\gamma^2 - (\tilde{x} - 1 - \eta_p)^2}{1 - \tilde{x}^2} \right\}^{1/2} \quad (\text{B.21})$$

$$+ \sqrt{2(1 + \eta_p)(x_0 - \tilde{x})\{\gamma^2 - (\tilde{x} - 1 - \eta_p)^2\}}, \quad (\text{B.22})$$

where the new variables (\tilde{x}, \tilde{z}) are related to the coordinate (x, y) through

$$\begin{pmatrix} \tilde{x} \\ \tilde{z} \end{pmatrix} = \frac{1}{R_s \sqrt{X_p^2 + Z_p^2}} \begin{pmatrix} X_p & Z_p \\ -Z_p & X_p \end{pmatrix} \begin{pmatrix} x \\ z \end{pmatrix}, \quad (\text{B.23})$$

and

$$x_0 = 1 - \frac{\gamma^2 - \eta_p^2}{2(1 + \eta_p)}, \quad (\text{B.24})$$

$$\zeta = \frac{2\eta_p + \gamma^2 + \eta_p^2}{2(1 + \eta_p)}, \quad (\text{B.25})$$

$$x_c = x_0 + s(\zeta - \gamma). \quad (\text{B.26})$$

Here, the value of s is obtained empirically to yield the best fit to the numerical results, and Ohta et al. (2009) derived $s = 0.4$ as a better value.

Figure B.2 shows a comparison of transit light curves between the Mandel's model with a small-planet approximation and the Ohta's one for the case of WASP-5b. The limb darkening coefficients are chosen for those for B&C, i.e., $u_1 = 0.27$ and $u_2 = 0.34$. The maximum difference is $\sim 2 \times 10^{-4}$, which is an order of magnitude less than the typical photometric precision of the B&C observations with 60 s exposure time. Therefore we can safely use this model for fitting each of the B&C light curves. However, this difference becomes to be considerable if we treat more precise light curves or the ensemble of all light curves. Because the Ohta's model is more reliable at a higher order level, we used this model for the fit to the ensemble data.

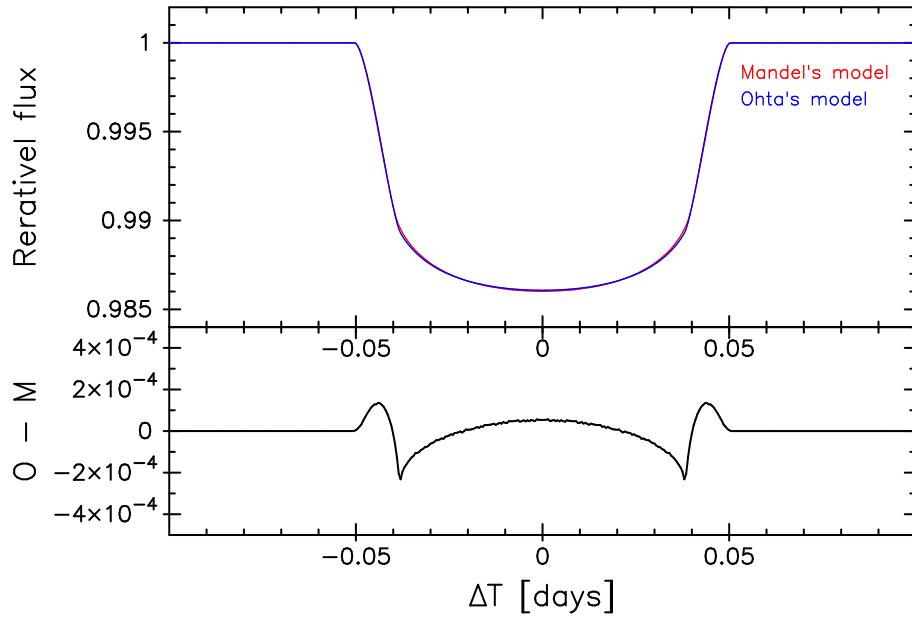


Figure B.2: A comparison of transit light curves between the Mandel’s model with a small-planet approximation and the Ohta’s model. Top panel: Light curves for WASP-5b drawn with the Mandel’s model (red) and the Ohta’s one (blue) are shown. All transit parameters are same for both models. The limb darkening coefficients are chosen for those for B&C, i.e., $u_1 = 0.27$ and $u_2 = 0.34$. Bottom panel: The differential light curve derived by subtracting the Mandel’s light curve from the Ohta’s one is shown. The maximum difference is $\sim 2 \times 10^{-4}$.

Appendix C

Analytic Formula for Rossiter-McLaughlin Effect

C.1 General Description

For a planetary system, the radial velocity of the star is written as

$$v = -\frac{m_p}{m_s + m_p} \frac{na \sin i}{\sqrt{1 - e^2}} [\sin(f + \omega) + e \sin \omega], \quad (\text{C.1})$$

where m_p , m_s , n , a , i , e , f , and ω are the planetary mass, the stellar mass, the mean motion, the semi-major axis, the orbital inclination, the eccentricity, the true anomaly, and the longitude of pericenter with respect to the line of sight, respectively (see e.g., Murray & Dermott 1999). When we use the same coordinate system as in Section B.2, the position of the planet is related to the angle λ between the z-axis (stellar-spin axis)

and the planetary orbital axis as

$$\mathbf{X} = r_p \begin{pmatrix} -\cos \lambda \sin(f + \omega) - \sin \lambda \cos i \cos(f + \omega) \\ \sin i \cos(f + \omega) \\ \sin \lambda \sin(f + \omega) - \cos \lambda \cos i \cos(f + \omega) \end{pmatrix}, \quad (\text{C.2})$$

where $r_p = a(1 - e^2)/(1 + e \cos f)$ is the star-planet distance.

During a transit, the planet masks a portion of the rotating stellar surface, leading to the observed radial velocity anomaly known as the Rossiter-McLaughlin (RM) effect. The radial velocity anomaly due to the RM effect is expressed as

$$\Delta v = -V \sin I_s \frac{\iint x I(x, z) dx dz}{\iint I(x, z) dx dz}, \quad (\text{C.3})$$

where V is the stellar rotational velocity and $I(x, z)$ is the stellar intensity at (x, z) . Therefore, if the relation between Δv and \mathbf{X} can be modeled, one can fit the model to the observed Δv to derive the values of $V \sin I_s$ and λ .

C.2 The Hirano's Model

For modeling velocity anomalies due to the RM effect, several theoretical developments have been done so far (e.g. Kopal 1942; Ohta et al. 2005; Giménez 2006). These authors developed their analytical formulae based on the first moment (intensity-weighted mean wavelength) of distorted absorption lines for calculating the velocity anomalies. However, namely, the moment method is not identical to the actual observations because, for instance, HARPS and SOPHIE teams involve the cross-correlation of the observed spectrum with a template spectrum, and the velocity anomaly is estimated from the peak of the cross-correlation function. This discrepancy leads systematics in the RM model, and tends to overestimate the value of $V \sin I_s$ (Triaud et al. 2009). Hirano et al. (2010) developed more

appropriate formulae based on the cross-correlation method, and we used the ‘‘Hirano’s model’’ for modeling the RM effect in this paper. Here we summarize their derivations.

A symmetric, stellar absorption line profile over the entire stellar disk outside the transit, $\mathcal{F}_{\text{star}}(\lambda)$, where λ is the wavelength, can be distorted due to the RM effect. During a transit, a portion on the stellar disk is occulted by a planet, and the flux contribution from the portion, $\mathcal{F}_{\text{planet}}(\lambda - \Delta\lambda)$, is subtracted from $\mathcal{F}_{\text{star}}(\lambda)$, yielding the distorted line profile of $\mathcal{F}_{\text{transit}}(\lambda)$ (see Figure C.1). The center of $\mathcal{F}_{\text{planet}}$ is Doppler-shifted by $\Delta\lambda$ relative to the central wavelength λ_0 of $\mathcal{F}_{\text{star}}$ since the portion occulted by the planet has a stellar rotation velocity,

$$v_p = c \frac{\Delta\lambda}{\lambda_0}, \quad (\text{C.4})$$

along the line of sight of an observer. Due to the distortion, the absorption line profile becomes asymmetric, leading to the observed radial velocity anomaly.

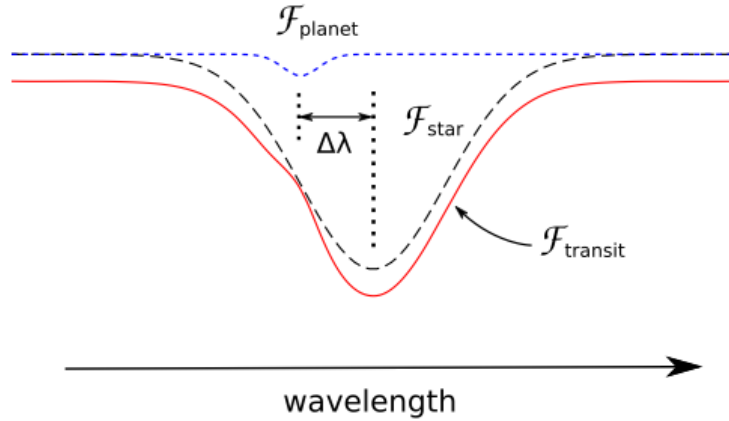


Figure C.1: Schematic absorption line profiles of a transiting planetary system (from Hirano et al. 2010). The black dashed line is a symmetric line profile with respect to the central wavelength of each line λ_0 over the entire stellar disk outside the transit, $\mathcal{F}_{\text{star}}(\lambda)$. The blue dotted line is a symmetric line profile for the portion occulted by a planet that is shifted by a wavelength of $\Delta\lambda$ with respect to λ_0 , $\mathcal{F}_{\text{planet}}(\lambda - \Delta\lambda)$. The resulting distorted stellar line profile in transit, $\mathcal{F}_{\text{transit}}(\lambda) = \mathcal{F}_{\text{star}}(\lambda) - \mathcal{F}_{\text{planet}}(\lambda - \Delta\lambda)$, is indicated by the red solid line.

A stellar absorption line profile is written as a convolution of an intrinsic line profile $S(\lambda)$ and a stellar rotation kernel $R(\lambda; \lambda_L)$ as

$$\mathcal{F}_{\text{star}}(\lambda) = 1 - S(\lambda) * R(\lambda; \lambda_L), \quad (\text{C.5})$$

where $R(\lambda; \lambda_L)$ broadens the intrinsic stellar line at λ_0 over the range from $\lambda_0 - \lambda_L$ to $\lambda_0 + \lambda_L$, where $\lambda_L/\lambda_0 = V \sin I_s/c$. Using Equation (C.5), the distorted line profile due to the RM effect is calculated as

$$\mathcal{F}_{\text{transit}}(\lambda) = -S(\lambda) * R(\lambda; \lambda_L) + fS(\lambda; \Delta\lambda), \quad (\text{C.6})$$

where f is the ratio of the flux from the occulted part of the stellar disk to the total flux.

Based on the cross-correlation method, the wavelength shift of central line δ_{RM} is obtained by maximizing the cross-correlation function:

$$\left. \frac{dC(x)}{dx} \right|_{x=\delta_{\text{RM}}} = 0, \quad (\text{C.7})$$

$$C(x) = \int_{-\infty}^{\infty} \mathcal{F}_{\text{star}}(\lambda - x) \mathcal{F}_{\text{transit}}(\lambda) d\lambda. \quad (\text{C.8})$$

A Voigt profile (convolution of a Gaussian and a Lorentzian) is often used to approximate $S(\lambda)$, but a Gaussian profile also provides a reasonable approximation. Here the Gaussian profile is adopted for the stellar line so that

$$S(\lambda) = G_S(\lambda; \beta) = \frac{1}{\beta\sqrt{\pi}} e^{-\lambda^2/\beta^2}, \quad (\text{C.9})$$

where β characterizes the thermal and microturbulent broadening. Meanwhile, $R(\lambda; \lambda_L)$ is

also approximated by a Gaussian:

$$R(\lambda; \lambda_L) \approx G_R(\lambda; \sigma) \equiv \frac{1}{\sigma\sqrt{\pi}} e^{-\lambda^2/\sigma^2}, \quad (\text{C.10})$$

where the relation between σ and λ_L is obtained by least-squares fitting of the Gaussian to a more accurate analytical formula (see Hirano et al. 2010, for the details). Substituting Equation (C.9) and (C.10) in Equation (C.5) and (C.6), and calculating Equation (C.7) and (C.8), one can derive

$$f = \left(\frac{\beta_*^2 + \beta_p^2}{2\beta_*^2} \right)^{3/2} \frac{\delta_{\text{RM}}}{\delta_{\text{RM}} - \Delta\lambda} \exp \left\{ -\frac{\delta_{\text{RM}}^2}{2\beta_*^2} + \frac{(\delta_{\text{RM}} - \Delta\lambda)^2}{\beta_*^2 + \beta_p^2} \right\}, \quad (\text{C.11})$$

where $\beta_*^2 = \beta^2 + \sigma^2$ and β_p indicates the narrow line originated from the portion of the planet. Here, $|\delta_{\text{RM}}/\Delta\lambda|$ can be approximated so that $|\delta_{\text{RM}}/\Delta\lambda| \ll 1$, and therefore the exponent in Equation (C.11) can be expanded up to the linear order of δ_{RM} :

$$-\frac{\delta_{\text{RM}}^2}{2\beta_*^2} + \frac{(\delta_{\text{RM}} - \Delta\lambda)^2}{\beta_*^2 + \beta_p^2} \approx \frac{\Delta\lambda^2}{\beta_*^2 + \beta_p^2} \left(1 - 2\frac{\delta_{\text{RM}}}{\Delta\lambda} \right) \quad (\text{C.12})$$

$$\equiv \kappa \left(1 - 2\frac{\delta_{\text{RM}}}{\Delta\lambda} \right). \quad (\text{C.13})$$

In general, we consider the case where $\Delta\lambda$ is well within the width of the stellar broadening, and therefore $\kappa \ll 1$. Thus, Equation (C.11) can be expanded up to the linear order in $\delta_{\text{RM}}/\Delta\lambda$ as

$$f \approx - \left(\frac{\beta_*^2 + \beta_p^2}{2\beta_*^2} \right)^{3/2} \frac{\delta_{\text{RM}}}{\Delta\lambda} (1 + \kappa). \quad (\text{C.14})$$

Finally, δ_{RM} is obtained as

$$\delta_{\text{RM}} \approx - \left(\frac{2\beta_*^2}{\beta_*^2 + \beta_p^2} \right)^{3/2} f \Delta\lambda \left(1 - \frac{\Delta\lambda^2}{\beta_*^2 + \beta_p^2} \right). \quad (\text{C.15})$$

The above equation can be rewritten as

$$\Delta v \approx - \left(\frac{2\beta_*^2}{\beta_*^2 + \beta_p^2} \right)^{3/2} f v_p \left\{ 1 - \frac{\lambda_0^2}{c^2(\beta_*^2 + \beta_p^2)} v_p^2 \right\} \quad (\text{C.16})$$

or

$$\Delta v \approx - \left(\frac{2(\beta^2 + \sigma^2)}{2\beta^2 + \sigma^2} \right)^{3/2} f v_p \left\{ 1 - \frac{\lambda_0^2}{c^2(2\beta^2 + \sigma^2)} v_p^2 \right\}, \quad (\text{C.17})$$

where β_p^2 is replaced with β^2 (line width without rotational broadening), and β_*^2 with $\beta^2 + \sigma^2$, in which σ indicates the stellar rotation width. The values of β and σ are determined empirically. Since f and v_p can be modeled as a function of the planetary position, one can fit this formula to the observed radial velocity anomalies to derive the values of $V \sin I_s$ and λ (here it is the angle between the stellar spin axis and the orbital axis).

Bibliography

- Adams, E. R., López-Morales, M., Elliot, J. L., Seager, S., & Osip, D. J. 2011, *ApJ*, 728, 125
- Agol, E., Steffen, J., Sari, R., & Clarkson, W. 2005, *MNRAS*, 359, 567
- Anderson, D. R., et al. 2008, *MNRAS*, 387, L4
- Backer, D. C., Foster, R. S., & Sallmen, S. 1993, *Nature*, 365, 817
- Bakos, G. Á., et al. 2006, *ApJ*, 650, 1160
- Barnes, R., & Greenberg, R. 2006, *ApJ*, 647, L163
- Bond, I. A., et al. 2004, *ApJ*, 606, L155
- Borucki, W. J., et al. 2011, *ArXiv e-prints*
- Boss, A. P. 1997, *Science*, 276, 1836
- . 2010, *ApJ*, 725, L145
- Burke, C. J., et al. 2010, *ApJ*, 719, 1796
- Cameron, A. G. W. 1978, *Moon and Planets*, 18, 5
- Charbonneau, D., Brown, T. M., Latham, D. W., & Mayor, M. 2000, *ApJ*, 529, L45
- Christiansen, J. L., et al. 2011, *ApJ*, 726, 94

- Claret, A. 2000, *A&A*, 363, 1081
- . 2004, *A&A*, 428, 1001
- Csizmadia, S., et al. 2010, *A&A*, 510, A94+
- Dobrovolskis, A. R., & Borucki, W. J. 1996, in *Bulletin of the American Astronomical Society*, Vol. 28, *Bulletin of the American Astronomical Society*, 1112–+
- Dravins, D., Lindegren, L., Mezey, E., & Young, A. T. 1998, *PASP*, 110, 610
- Eastman, J., Siverd, R., & Gaudi, B. S. 2010, *PASP*, 122, 935
- Ford, E. B., & Gaudi, B. S. 2006, *ApJ*, 652, L137
- Ford, E. B., et al. 2011, *ArXiv e-prints*
- Frieboes-Conde, H., Herczeg, T., & Høg, E. 1970, *A&A*, 4, 78
- Fukui, A., et al. 2011, *PASJ*, 63, 287
- Gatewood, G., & Eichhorn, H. 1973, *AJ*, 78, 769
- Gaudi, B. S., & Winn, J. N. 2007, *ApJ*, 655, 550
- Gibson, N. P., et al. 2009, *ApJ*, 700, 1078
- . 2010, *MNRAS*, 401, 1917
- Gillon, M., et al. 2009, *A&A*, 496, 259
- Giménez, A. 2006, *ApJ*, 650, 408
- Goldreich, P. 1965, *MNRAS*, 130, 159
- Goodricke, J. 1783, *Royal Society of London Philosophical Transactions Series I*, 73, 474

- Gould, A., & Loeb, A. 1992, *ApJ*, 396, 104
- Hayashi, C., Nakazawa, K., & Nakagawa, Y. 1985, in *Protostars and Planets II*, ed. D. C. Black & M. S. Matthews, 1100–1153
- Hellier, C., et al. 2009, *Nature*, 460, 1098
- Heyl, J. S., & Gladman, B. J. 2007, *MNRAS*, 377, 1511
- Hirano, T., Suto, Y., Taruya, A., Narita, N., Sato, B., Johnson, J. A., & Winn, J. N. 2010, *ApJ*, 709, 458
- Holman, M. J., & Murray, N. W. 2005, *Science*, 307, 1288
- Holman, M. J., et al. 2010, *Science*, 330, 51
- Howell, S. B. 2006, *Handbook of CCD astronomy*, ed. Howell, S. B.
- Hoyer, S., Rojo, P., López-Morales, M., Díaz, R. F., Chambers, J., & Minniti, D. 2011, *ApJ*, 733, 53
- Hrudková, M., et al. 2010, *MNRAS*, 403, 2111
- Ida, S., & Lin, D. N. C. 2008, *ApJ*, 673, 487
- Irwin, J. B. 1959, *AJ*, 64, 149
- Jacob, W. S. 1855, *MNRAS*, 15, 228
- Jewitt, D. C., Trujillo, C. A., & Luu, J. X. 2000, *AJ*, 120, 1140
- Jordán, A., & Bakos, G. Á. 2008, *ApJ*, 685, 543
- Kalas, P., et al. 2008, *Science*, 322, 1345
- Ketchum, J. A., Adams, F. C., & Bloch, A. M. 2011, *ApJ*, 726, 53

- Kipping, D., & Bakos, G. 2011, *ApJ*, 733, 36
- Kipping, D. M. 2009a, *MNRAS*, 392, 181
- . 2009b, *MNRAS*, 396, 1797
- Kopal, Z. 1942, *Proceedings of the National Academy of Science*, 28, 133
- Kozai, Y. 1962, *AJ*, 67, 591
- Lafrenière, D., Jayawardhana, R., & van Kerkwijk, M. H. 2008, *ApJ*, 689, L153
- Lagrange, A., et al. 2009, *A&A*, 493, L21
- Latham, D. W., et al. 2011, *ApJ*, 732, L24+
- Laughlin, G., & Chambers, J. E. 2001, *ApJ*, 551, L109
- Lee, M. H., & Peale, S. J. 2002, *ApJ*, 567, 596
- Léger, A., et al. 2009, *A&A*, 506, 287
- Lin, D. N. C., Bodenheimer, P., & Richardson, D. C. 1996, *Nature*, 380, 606
- Lin, D. N. C., & Papaloizou, J. 1985, in *Protostars and Planets II*, ed. D. C. Black & M. S. Matthews, 981–1072
- Lin, D. N. C., & Papaloizou, J. 1986, *ApJ*, 309, 846
- Lissauer, J. J., et al. 2011, *Nature*, 470, 53
- Lovis, C., et al. 2011, *A&A*, 528, A112+
- Maciejewski, G., et al. 2010, *MNRAS*, 407, 2625
- . 2011, *MNRAS*, 411, 1204

- Madhusudhan, N., & Winn, J. N. 2009, *ApJ*, 693, 784
- Mandel, K., & Agol, E. 2002, *ApJ*, 580, L171
- Mao, S., & Paczynski, B. 1991, *ApJ*, 374, L37
- Marois, C., Macintosh, B., Barman, T., Zuckerman, B., Song, I., Patience, J., Lafrenière, D., & Doyon, R. 2008, *Science*, 322, 1348
- Masset, F. S., D'Angelo, G., & Kley, W. 2006, *ApJ*, 652, 730
- Mayor, M., & Queloz, D. 1995, *Nature*, 378, 355
- McLaughlin, D. B. 1924, *ApJ*, 60, 22
- Meschiari, S., & Laughlin, G. P. 2010, *ApJ*, 718, 543
- Miller-Ricci, E., et al. 2008, *ApJ*, 682, 586
- Miralda-Escudé, J. 2002, *ApJ*, 564, 1019
- Murray, C. D., & Dermott, S. F. 1999, *Solar system dynamics*, ed. Murray, C. D. & Dermott, S. F.
- Mustill, A. J., & Wyatt, M. C. 2011, *MNRAS*, 413, 554
- Nagasawa, M., Ida, S., & Bessho, T. 2008, *ApJ*, 678, 498
- Narita, N., Sato, B., Hirano, T., & Tamura, M. 2009, *PASJ*, 61, L35
- Narita, N., et al. 2007, *PASJ*, 59, 763
- Nascimbeni, V., Piotto, G., Bedin, L. R., & Damasso, M. 2011, *A&A*, 527, A85+
- Ohta, Y., Taruya, A., & Suto, Y. 2005, *ApJ*, 622, 1118
- . 2009, *ApJ*, 690, 1

- Paczynski, B. 1986, *ApJ*, 304, 1
- Pál, A. 2008, *MNRAS*, 390, 281
- Pinsonneault, M. H., DePoy, D. L., & Coffee, M. 2001, *ApJ*, 556, L59
- Podlewska, E., & Szuszkiewicz, E. 2008, *MNRAS*, 386, 1347
- Press, W. H., Teukolsky, S. A., Vetterling, W. T., & Flannery, B. P. 1992, *Numerical recipes in C. The art of scientific computing*, ed. Press, W. H., Teukolsky, S. A., Vetterling, W. T., & Flannery, B. P.
- Rabus, M., Deeg, H. J., Alonso, R., Belmonte, J. A., & Almenara, J. M. 2009, *A&A*, 508, 1011
- Reuyl, D., & Holmberg, E. 1943, *ApJ*, 97, 41
- Rossiter, R. A. 1924, *ApJ*, 60, 15
- Sako, T., et al. 2008, *Experimental Astronomy*, 22, 51
- Sanchis-Ojeda, R., Winn, J. N., Holman, M. J., Carter, J. A., Osip, D. J., & Fuentes, C. I. 2011, *ApJ*, 733, 127
- Shporer, A., Brown, T., Lister, T., Street, R., Tsapras, Y., Bianco, F., Fulton, B., & Howell, A. 2010, *ArXiv e-prints*
- Southworth, J., et al. 2009, *MNRAS*, 396, 1023
- Steffen, J. H., & Agol, E. 2005, *MNRAS*, 364, L96
- Strand, K. A. 1943, *PASP*, 55, 29
- Sumi, T., et al. 2010, *ApJ*, 710, 1641
- Tanaka, H., Takeuchi, T., & Ward, W. R. 2002, *ApJ*, 565, 1257

- Triaud, A. H. M. J., et al. 2009, *A&A*, 506, 377
- . 2010, *A&A*, 524, A25+
- van de Kamp, P. 1963, *AJ*, 68, 515
- Vogt, S. S., Butler, R. P., Rivera, E. J., Haghighipour, N., Henry, G. W., & Williamson, M. H. 2010, *ApJ*, 723, 954
- Walker, G. A. H., Walker, A. R., Irwin, A. W., Larson, A. M., Yang, S. L. S., & Richardson, D. C. 1995, *Icarus*, 116, 359
- Ward, W. R. 1986, *Icarus*, 67, 164
- Warner, B. D. 2006, *A Practical Guide to Lightcurve Photometry and Analysis*, ed. Warner, B. D.
- Watson, C. A., & Marsh, T. R. 2010, *MNRAS*, 405, 2037
- Weidner, C., & Horne, K. 2010, *ArXiv e-prints*
- Winn, J. N. 2010, *Exoplanet Transits and Occultations*, ed. Seager, S., 55–77
- Winn, J. N., Fabrycky, D., Albrecht, S., & Johnson, J. A. 2010, *ApJ*, 718, L145
- Winn, J. N., Holman, M. J., Carter, J. A., Torres, G., Osip, D. J., & Beatty, T. 2009, *AJ*, 137, 3826
- Winn, J. N., et al. 2008, *ApJ*, 683, 1076
- Wolszczan, A. 1994, *Science*, 264, 538
- Wolszczan, A., & Frail, D. A. 1992, *Nature*, 355, 145
- Wright, J. T. 2005, *PASP*, 117, 657

Wright, J. T., Upadhyay, S., Marcy, G. W., Fischer, D. A., Ford, E. B., & Johnson, J. A.
2009, *ApJ*, 693, 1084

Wright, J. T., et al. 2011, *ApJ*, 730, 93

Yanagisawa, T., et al. 2000, *Experimental Astronomy*, 10, 519

Yee, J. C., et al. 2009, *ApJ*, 703, 2082

Young, A. T. 1967, *AJ*, 72, 747